CAD IN MACHINERY DESIGN

IMPLEMENTATION AND EDUCATIONAL ISSUES

XXIX INTERNATIONAL POLISH-UKRAINIAN CONFERENCE

COLLECTIVE MONOGRAPH

Edited by: Marian Banaś, Krzysztof Pytel
Mykhaylo Lobur, Andriy Zdobytskyi

WYDAWNICTWA AGH

KRAKOW 2023

CAD IN MACHINERY DESIGN

IMPLEMENTATION AND EDUCATIONAL ISSUES

XXIX INTERNATIONAL POLISH-UKRAINIAN CONFERENCE

COLLECTIVE MONOGRAPH

Edited by: Marian Banaś, Krzysztof Pytel
Mykhaylo Lobur, Andriy Zdobytskyi

WYDAWNICTWA AGH

KRAKOW 2023

Published by AGH University Press

ISBN 978-83-67427-24-1
e-ISBN 978-83-67427-25-8

Head of Publishing of AGH University Press: *Jan Sas*

Editors' affiliation
Marian Banaś, Krzysztof Pytel
AGH University of Science and Technology
Faculty of Mechanical Engineering and Robotics

Andriy Zdobytskyi, Mykhaylo Lobur
Lviv Polytechnic national University
Department of Computer-Aided Design Systems

Technical editor: *Agnieszka Rusinek*

Desktop publishing: *ANDRE*

Cover design: *Paweł Sepielak*

AGH University Press (Wydawnictwa AGH)
al. A. Mickiewicza 30, 30-059 Kraków
tel. 12 617 32 28, 12 636 40 38
e-mail: redakcja@wydawnictwoagh.pl
www.wydawnictwo.agh.edu.pl

Contents

Preface

The CADMD conference series started in Warsaw in 1994 and has been organized annually since then in Poland and Ukraine.

In 2021 the XXIX CADMD conference took place in Krakow. A short history of the conference can be found on its website (http://cadmd.lpnu.ua/).

The organizers are as follows:

- Faculty of Mechanical Engineering and Robotics, AGH University of Science and Technology, Krakow, Poland;
- Department of Automated Design Systems, Lviv Polytechnic National University, Lviv, Ukraine;
- Faculty of Electrical Engineering, Białystok University of Technology, Białystok, Poland;
- Institute of Fundamentals of Mechanical Engineering, Warsaw University of Technology, Warsaw, Poland.

The aim of the conference is to exchange experiences between scientists of Ukraine and Poland and their young and promising colleagues in modern information technology, the development of CAD in mechanics, teaching methods and the implementation of automated systems in the educational process, and establishing closer ties between researchers.

The main topics of discussion are as follows:

- automated design systems;
- robotics, mechatronics, and automation;
- process management, identification, modeling, and modeling of processes and systems;
- energy systems and environmental protection facilities –microelectromechanical systems;
- 3D scanning, printing, and augmented and virtual reality;
- engineering education.

The XXIX International Polish-Ukrainian Conference CAD in Machinery Design Implementation and Educational Issues occurred under the patronage of Professor Jerzy Lis (AGH UST Rector). The conference took place in Krakow, Poland, on December 9–10, 2021.

Analysis of applicability of flow-acoustic coupling used for pressure measurement

Paweł Łojek ORCID ID: 0000-0002-4291-7816

AGH University of Science and Technology
Faculty of Mechanical Engineering and Robotics
Department of Power Systems and Environmental Protection Facilities, Krakow
email: lojek@agh.edu.pl

Ireneusz Czajka ORCID ID: 0000-0003-0013-8467

AGH University of Science and Technology
Faculty of Mechanical Engineering and Robotics
Department of Power Systems and Environmental Protection Facilities, Krakow
email: iczajka@agh.edu.pl

ABSTRACT

This paper presents the concept and results of initial simulations of an acoustic system for absolute pressure measurement. Its working principle is based on a coupling between the flow and acoustic fields. The measurement is performed indirectly. The measurement of absolute pressure is based on measuring the velocity and time of arrival of an acoustic wave and the relationship between the pressure and speed of sound in a given medium. The concept was verified numerically using the finite volume method and the OpenFOAM environment. One possible application of the system is to measure the mean pressure on the walls of buildings.

Keywords: measurement system, numerical simulations, pressure measurement, CFD

1. Introduction

Knowledge about the pressure that is exerted on the walls of buildings is very useful for designing new constructions and in the diagnostics of existing ones. The characteristics of pressure may be used for estimating the serviceability and durability of a structure (Kim et al. 2018). Currently used methods allow for wind-pressure measurement by using piezoelectric or piezoresistive sensors that are connected by plastic tubes and located on various positions on the exterior sides of a building. The methodology of measurements has not changed over the years (Levitan, Mehta 1992; Zhang, Li 2018); unfortunately, these methods are often highly inefficient and expensive.

The lack of an efficient method for measuring the pressure that is exerted on buildings was the main reason for developing a new method that allowed for measuring the mean pressure at a given distance. Another method that is based on a similar phenomenon is laser measurement, which uses the relationship between air pressure and electromagnetic wave properties.

Currently, the research on new pressure-measurement methods is ongoing; however, the working principle of the majority of these can be reduced to an array of piezoelectric sensors. Thus far, none of them have allowed for measurements of mean values at great distances (An et al. 2018).

The problem of measuring nonelectrical values such as pressure is connected with developing a sensor that is capable of registering quantity (which is easy to measure) and choosing a transducer that allows us to convert a measured signal to an electric one. The authors decided to use couplings between thermodynamic state variables and acoustic field parameters. In the researched case, couplings between flow and acoustic fields were used.

2. Materials and methods

2.1. Idea of measurement system

The working principle of pressure sensors is based on many physical phenomena; so far, however, none of these sensors have used the relationship between the speed of sound in air and its pressure. This is described by the following formula:

$$c = \sqrt{\frac{\kappa p}{\rho}} \tag{1}$$

where:

κ – adiabatic index [–],
p – pressure [Pa],
ρ – density [kg/m^3],
c – speed of sound in air [m/s^2].

Equation (1) is based on a linearized Euler equation and assumes an adiabatic process during wave propagation and very small air pressure and density changes as compared to reference values (Suder-Dębska et al. 2014; 2018).

Measurement of the time of the arrival of a wave, the known distance between transducers, and Equation (1) allow for the following calculation of pressure:

$$t = \frac{L}{c} = \frac{L}{\sqrt{\frac{\kappa p}{\rho}}} \Rightarrow p = \frac{L^2 \rho}{\kappa t^2} \tag{2}$$

where:

t – time of arrival of acoustic wave [s],
L – distance between transducers [m] (Fig. 1a).

The main issue that could prevent the proper working of the system are disturbances that are caused by an air flow that is parallel to the axes that connect the transducers. The influence of the movement of the medium can change the wave velocity. One of the assumptions of the concept was the symmetrical distribution of the v_y speed component (shown in Figure 1b); this assumption was verified by conducting numerical simulations.

The velocity and pressure fields that were the results of simulations have allowed us to verify whether the influence of a moving medium interferes with the wave velocity and disrupts the measurements.

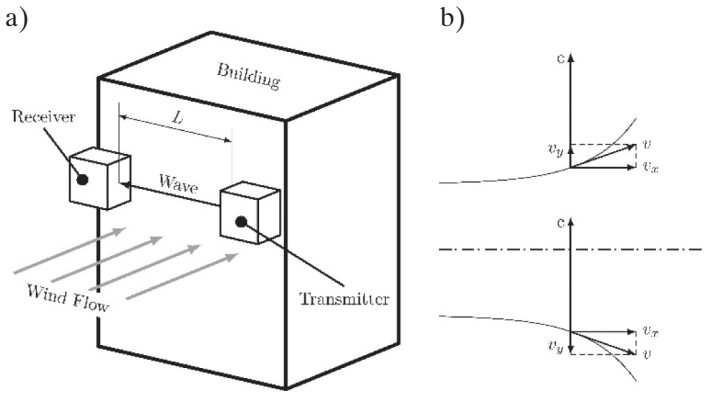

Fig. 1. Measurement system diagram: a) possible application of system for pressure measurement on elevation of buildings; b) distribution of flow and acoustic wave velocities

2.2. Modeling flow

The partial differential equations of continuity (3) and Navier–Stokes (4) can represent a mathematical model of the flow (Moukalled et al. 2015):

$$\frac{\partial \rho}{\partial t} + \nabla \cdot \rho v = 0 \tag{3}$$

$$\rho \frac{Dv}{Dt} = -\nabla p + \eta \left(\nabla^2 + \frac{1}{3} \nabla (v) \right) + F \tag{4}$$

where:

v – velocity [m/s^2],
t – time [s],
F – external forces [N],
η – viscosity [Pa·s].

This was solved by using the finite volume method that was implemented in the OpenFOAM environment and PISO algorithm (Holzmann 2016).

The air flow around two transducers that were presented as cuboids and cylindrical obstacles and placed inside a wind tunnel was modeled (instead of a wall with transducers).

The model was shown in the Figure 2. This allowed us to speed up the simulations and verify the assumptions of the concept. The velocities of constant values (to 5, 10, and 20 m/s) and angles of attack of 0°, 5°, 10°, 20° , and 30° were applied at the inlet to check how the flow behaved and whether the assumption of a symmetrical velocity distribution was met.

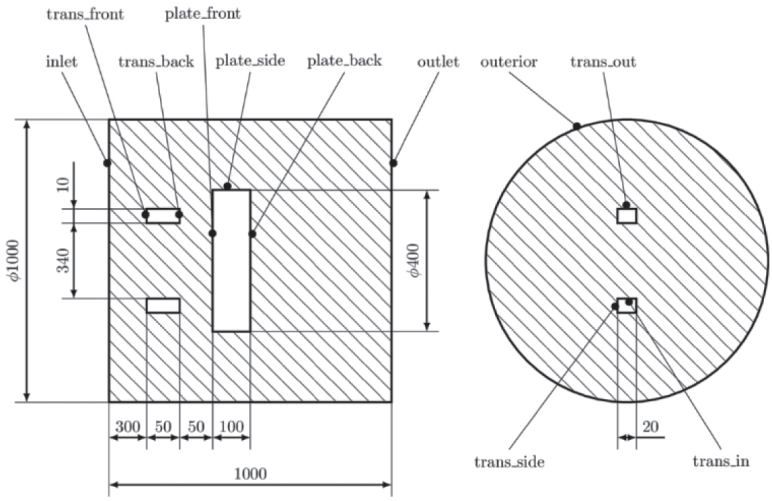

Fig. 2. Computational model with marked boundaries

The air flow was modeled under standard conditions for temperature and pressure; it was also assumed that the flow was incompressible. At the wall boundaries (which were shown in the Figure 2), the velocity was equal to 0, and at the outlet boundary, the velocity gradient was zero. For each boundary, a zero-pressure gradient was specified except for the outlet (for which the pressure was equal to zero).

For such flow velocities, it can be assumed that the flow is turbulent, so turbulence modeling was necessary. A k – ω SST (shear stress transport) model that combined the k – ω and k – ε models was used due to its versatility (Menter 1994). This model expands the mathematical model of the flow by the following turbulent kinetic energy k (Eq. (5)) and specific turbulent dissipation rate ω (Eq. (6)):

$$\frac{D\rho k}{Dt} = \tau_{ij}\frac{\partial u_i}{\partial x_j} - \beta\rho\omega k + \frac{\partial}{\partial x_j}\left[(\mu + \delta_k\mu_t)\frac{\partial k}{\partial x_j}\right] \tag{5}$$

$$\frac{D\rho\omega}{Dt} = \frac{\gamma}{\nu_t}\tau_{ij}\frac{\partial u_i}{\partial x_j} - \beta\rho\omega^2 + \frac{\partial}{\partial x_j}\left[(\mu + \sigma_k\mu_t)\frac{\partial\omega}{\partial x_j}\right] + 2(1-F_1)\rho\sigma_{\omega 2}\frac{1}{\omega}\frac{\partial k}{\partial x_j}\frac{\partial\omega}{\partial x_j} \tag{6}$$

where:

k – turbulent kinetic energy [m^2/s^2],
ω – specific turbulent dissipation rate [1/s],
τ_{ij} – turbulent shear stress [Pa],
F_1 – blending function [–],
β, γ, σ – model constants [–],
μ_t – turbulent viscosity [m^2/s].

2.3. Design of measurement system

The designed measuring system consisted of two ultrasound sensors with a center frequency that was equal to 40 kHz; one of these acted as a transmitter, and the other as a receiver. They were connected to two devices that acted as a signal generator and a processing unit. Also, an environmental sensor that was connected to an Arduino microcontroller needed to be used to measure the air humidity and atmospheric pressure. A diagram of the measurement system is shown in Figure 3.

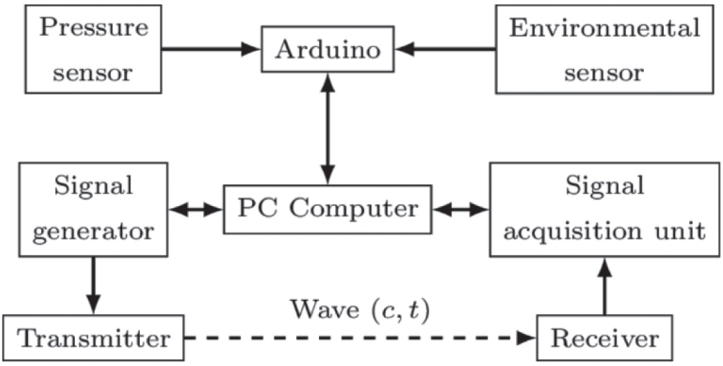

Fig. 3. Block diagram of measurement system

Attempts were made to build and program a measuring system; the signal generator and processing unit were composed of two Arduino microcontrollers. The Arduino unit itself was not capable of recording and registering a signal because of the lack of an analog I/O and low resolution; therefore, an Analog Shield add-on board for the unit was used in the proposed system. As mentioned earlier, two ultrasound sensors were used. The emitted signal was a superposition of a 40 kHz sine wave and 25 Hz square wave (Majerczak 2018).

3. Results and discussion

3.1. Simulation results

The computed values of the velocity and pressure between the transducers were extracted from the entire domain and analyzed. Based on Equations (1) and (2), the time of the arrival of a wave in each cell of the mesh on the path of the wave was estimated:

$$t = \sum_{n} t_i = \sum_{i=0}^{n} \frac{y_i}{\sqrt{\frac{\kappa p_i}{\rho}} \pm v_i} \tag{7}$$

Equation (7) allowed us to determine the total time of the arrival and check whether it depended on the drift velocity.

The distributions of the pressure that are shown in Figure 4 are symmetrical about the x-axis, along with the distribution of the speed of sound that is shown in Figure 5. These distributions and the flow velocity streamlines that are presented in Figure 6 confirm the assumption of the symmetrical distribution of velocity. The streamlines that are shown in Figure 6, were computed for $v_\infty = 10$ m/s.

For the adopted geometrical model, the value of the dynamic pressure between the transducers for different velocities at the inlet varied from 17 to 285 Pa. This corresponded to the times of arrival of the acoustic wave (from 988.99 to 987.59 μs).

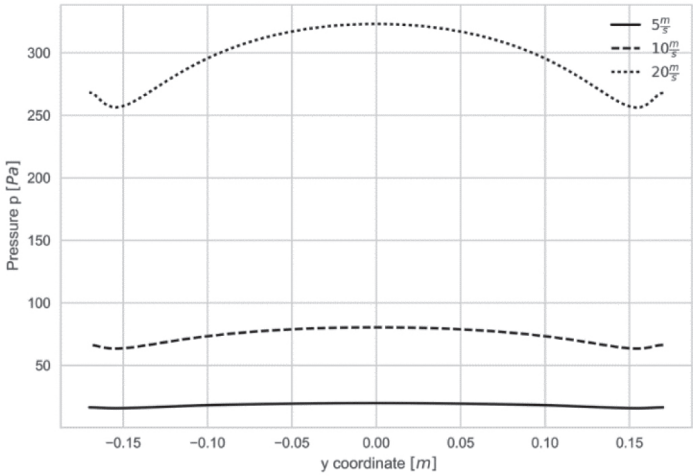

Fig. 4. Distribution of pressure between transducers (along x-axis)

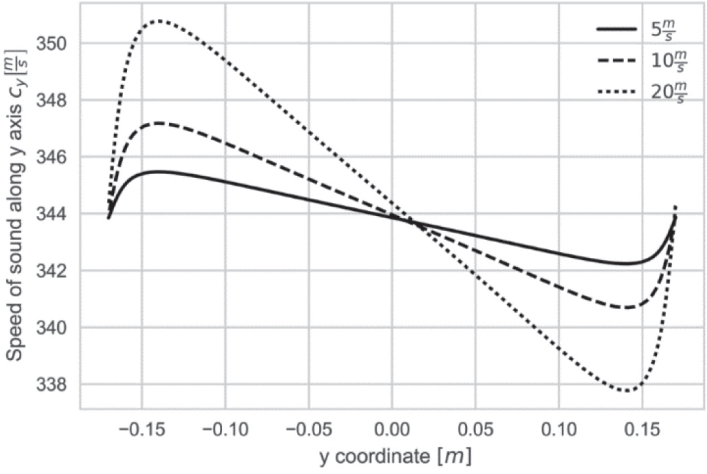

Fig. 5. Distribution of speed of sound between transducers (along x-axis)

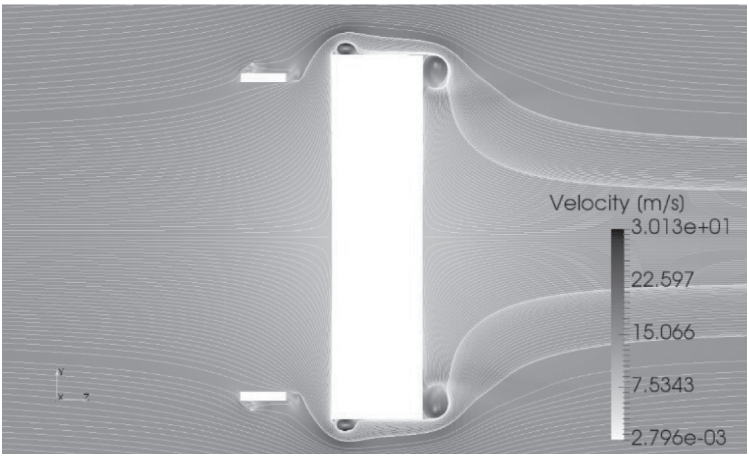

Fig. 6. Streamlines of flow around obstacle

It was estimated that a decrease of 5 ns in the time of arrival corresponded to a mean pressure increase of 1 Pa. An analysis of the results also showed that the difference in the times of arrival that were calculated with and without including the drift speed was 20 ns on average. For the chosen model, this corresponded to a pressure increase of 5 Pa. Other results were described in Łojek (2017).

3.2. Measurement results

The measurements that were carried out using the system that was described in Majerczak (2018) showed that the proposed working principle was partially correct – a system that is composed of two ultrasound sensors can effectively measure pressure. The measurements were carried out without the presence of a flow; the main purpose of the experiment was to check whether the system could effectively measure pressure. The results are shown in Table 1.

Table 1
Results of measurements

Parameter	Value
Number of measurements	77
Mean pressure p_m [Pa]	104,250
Max. pressure $p_{\max}$ [Pa]	110,827
Min. pressure $p_{\min}$ [Pa]	96,884
Standard deviation σ [Pa]	2,689

4. Conclusions

The main purpose of the research and simulations was to verify whether the proposed concept could be implemented. The results of the preliminary simulations allow to state that the concept and assumptions are correct. The simulations showed that the distribution of the pressure and velocity component that was parallel to the front side of the obstacle that were measured between the transducers was symmetrical around the axis along the wind tunnel. The change in the overall time of arrival of the acoustic wave that was caused by this component was very small and can be omitted.

A prototype of the measurement system was designed and assembled. The measurements that were carried out using it showed that pressure can be measured using flow-acoustic coupling.

The next stage of building the measurement system will be to develop a new model that takes the coupling of acoustic and flow fields into account and then conduct new simulations and analyses. Experimental verifications of simulations of the flow around obstacles in wind tunnels are necessary. A prototype of the system must be rebuilt using components that are more accurate.

REFERENCES

An L., Lu T., Xu J., Wang Z., Xu M., Wang T.J., 2018, *Soft sensor for measuring wind pressure*, International Journal of Mechanical Sciences, 141, 386–392.

Holzmann T., 2016, *Mathematics, Numerics, Derivations and OpenFOAM*, Holzmann CFD, Bad Wörishofen.

Kim Y.C., Lo Y.L., Chang C.H., 2018, *Characteristics of unsteady pressures on slender tall building*, Journal of Wind Engineering and Industrial Aerodynamics, 174, 344–357.

Levitan M.L., Mehta K.C., 1992, *Texas Tech field experiments for wind loads part 1: Building and pressure measuring system*, Journal of Wind Engineering and Industrial Aerodynamics, 43, 1–3, 1565–1576.

Łojek P., 2017, *Koncepcja akustycznego systemu pomiaru ciśnienia z weryfikacją numeryczną* [Master's thesis], AGH University of Science and Technology, Krakow.

Majerczak M., 2018, *Prototyp akustycznego systemu pomiaru ciśnienia z wykorzystaniem platformy Arduino* [Master's thesis], AGH University of Science and Technology, Krakow.

Menter F.R., 1994, *Two-equation eddy-viscosity turbulence models for engineering applications*, AIAA Journal, 32(8), 1598–1605.

Moukalled F., Mangani L., Darwish M., 2015, *The Finite Volume Method in Computational Fluid Dynamics*, Springer International Publishing.

Suder-Dębska K., Czajka I., Czechowski M., 2014, *Sensitivity analysis of acoustic field parameters on a change of boundary conditions in a room*, Archives of Acoustics, 39(3), 343–350.

Suder-Dębska K., Gołaś A., Filipek R., 2018, *Wprowadzenie do akustyki użytkowej*, Wydawnictwa AGH, Kraków.

Zhang J., Li Q., 2018, *Field measurements of wind pressures on a 600 m high skyscraper during a landfall typhoon and comparison with wind tunnel test*, Journal of Wind Engineering and Industrial Aerodynamics, 175, 391–407.

Analysis of external factors that affect availability of gas engines

Adam Kalwar ORCID ID: 0000-0572-1019-4354

PGNiG Termika Energetyka Przemysłowa S.A., Jastrzębie-Zdrój
email: adam.kalwar@termika.pgnig.pl

Krzysztof Pytel ORCID ID: 0000-0002-1924-8351

AGH University of Science and Technology
Faculty of Mechanical Engineering and Robotics
Department of Power Systems and Environmental Protection Facilities, Krakow
email: krzysztof.pytel@agh.edu.pl

Franciszek Kurdziel ORCID ID: 0000-0572-1019-6083

PGNiG Termika Energetyka Przemysłowa S.A., Jastrzębie-Zdrój
email: franciszek.kurdziel@termika.pgnig.pl

Grzegorz Grzywnowicz ORCID ID: 0000-0007-2336-5439

PGNiG Termika Energetyka Przemysłowa S.A., Jastrzębie-Zdrój
email: grzegorz.grzywnowicz@termika.pgnig.pl

Uliana Marikutsa ORCID ID: 0000-0002-9514-7413

Lviv Polytechnic National University
Institute of Computer Science and Information Technologies
Department of Computer-Aided Design Systems, Lviv
email: uliana.b.marikutsa@lpnu.ua

ABSTRACT

The factors that directly affect the operation of the gas-fired internal combustion engines that are used in grid-connected generators are presented. Those factors that hinder their operation are also presented, along with ways to solve problems at the operating stage. Our conclusions are also presented for the future that can be used in further projects of cogeneration installations.

Keywords: gaseous fuel, mine gas, gas engines, cogeneration, gas-fired power generation

1. Introduction

Gas engines require certain conditions for fault-free operation – the fulfilment of which makes it possible to achieve the desired efficiency parameters and planned power output (both electrical and thermal). The operating conditions for gas engines that are fueled by mine gas and installed in a former mine site have been analyzed. The chosen location has a definite influence on their efficiency of operation and the specific operations that need to be carried out in order to ensure the smooth running of the engines.

2. Impact of location on operation

The installations of the analyzed gas engines were built in free-standing buildings on the site of a combined heat and power plant that used to be part of a mine. The engine-building area is located at a distance of approximately 200 m from a coal stockpile and 30 m from a fly ash-loading station (from the combustion of coal in pulverized fuel boilers). The ash-loading facility was in use until the winter season of 2017/18 and was decommissioned on March 1, 2018. The air intake to the air-handling units was directed specifically toward the ash-loading station and coal stockpile. This was the solution that was used for Gas Engine No. 1 (built in 2011). Analyzing the materials that concern the repair and maintenance of this engine, it can be seen that the entire set of filters is required to be replaced every 1000 operating hours on average (the minimum filter-operating period was 609 operating hours, and the longest was 3296 operating hours). Once the ash-loading station was shut down, the average time between replacing the filters increased to approximately 3000 operating hours. In 2014, the construction of Gas Engine No. 2 was started in the identical location to that of Gas Engine No. 1. Bearing in mind that the problems that are associated with the need to frequently change the filters of the air-handling units, it was decided to change the direction of the air intake so that the air supply ducts for ventilation systems drew in air from a different direction. The solution that was based on changing the direction of the ventilation

air intake worked well on Gas Engine No. 2; therefore, it was decided to rebuild the air intake of the air-handling units so that the air-intake direction was the same as with Gas Engine No. 2. During an analysis of the work on the ventilation air installation, another problem was discovered. The solution turned out to be correct, and the filters were changed much less frequently (every 6100 operating hours on average – the shortest period for a set of filters was 3254 operating hours, and the longest period was 8997 operating hours).

The location in this area showed the influence of the wind direction on the amount of contamination, as the winds in the study area often blow from the direction of the coal dump toward the gas engine buildings. The problem of the fouling of the air-handling-unit filters is exacerbated during periods of drought, the periods of coal delivery to the stockpile, and the periods of the operation of the coal stockpile; i.e., during furnace carburizing in the boilers (in recent years, the period of the operation of the coal stockpile was reduced to three months).

The blowing in of dust, fine sand, and other impurities also contribute to the clogging of the table coolers that are responsible for emergency cooling of the engine as well as for maintaining the correct temperature during its operation with limited or no heat extraction at all. The fans that were installed in the upper part of the radiator draw in air from the bottom of the radiator; this air flows through the radiator to cool the coolant. Fine impurities that are entrained with the air gradually contaminate the lower part of the radiator, thus restricting the cooling. The simplest way to reduce the negative impact of this on the operations of the gas engines is to wash the radiators (Moran et al. 2014). This process is performed with the engine switched off by spraying the top of the radiator with a cleaning agent; after a short period of time, the radiator is rinsed with a jet of water in a direction that is opposite of the airflow. This radiator washing is usually performed twice a year (before the end of the heating season); i.e., before the period of operation of the installation with limited heat extraction and before the start of the heating season when the dirt that accumulated in the radiator during the period of less precipitation is removed. Washing the radiators twice is sufficient for ensuring their adequate cleanliness. Radiators should not be washed before a period of prolonged installation downtime, as engines that become damp during the washing are more prone to bearing seizure and motor winding damage in the fans. After washing, it is a good idea to run the fans in manual mode for a few hours at a low load; this practice reduces the occurrence of damage to the electric motors.

3. Influence of combustion air duct design

During the operation of Gas Engine No. 1, it was also found that the combustion air filters became dirty very quickly. The fouling of the combustion air filters sometimes

occurred very quickly, requiring their replacement even every 250 operating hours. This phenomenon seemed puzzling because the engine building is enclosed and sealed and the previously described air-handling units are responsible for supplying combustion air. During subsequent cases of the premature fouling of the combustion air filters, the degree of the fouling of the air-handling-unit filters was also checked. During these checks, it turned out that, despite the soiling of the combustion air filters, the filters of the air-handling units remained quite clean (in a state that did not require replacement). The problem was referred to the system designer; this designer recommended changing the filtration class from G4 to G5. However, after the change of the filter class for the air-handling units, the problem of the fouling of the combustion air filters remained (although to a lesser extent). When work began on designing the new air intake system for the air-handling units of Gas Engine No. 1, the problem with the accelerated fouling of the combustion air filters was resolved; the reason for this situation was the poor design of the air-handling-unit's intake ducts, resulting in the point increases intake velocity. This in turn caused dirt to be dragged through the filter material.

4. Influence of operating conditions

Gas engines operate during the heating season with a maximum load on the heat-recovery system, and the heat is transferred via a plate heat exchanger to the district heating system (thus relieving the load on the engine cooling system). This condition usually lasts from September through May. After this period, heat is transferred to the district heating network to a limited extent. Additionally, rising ambient temperatures place an increasing load on the engine's cooling system. An engine-cooling system without heat recovery is designed to maintain maximum engine performance at an ambient temperature of 30°C.

An example graph of the change in the load of an engine heat-recovery system is shown in Figure 1. The orange graph illustrates the heat-energy production in hot water, while the turquoise graph is the heat-energy production for central heating. In January 2020, the engine had an average load of 4.2 MWe and 4.13 MWt (an average of 2.72 MWt for DHW and 1.41 MWt for central heating), whereas in July of the same year, the engine operated with a load of 4.2 MWe and 0.58 MWt (DHW only). As the ambient temperature rises and the temperature in the engine-cooling system increases, it reduces the power to prevent overheating the engine. According to the engine manufacturer's guidelines, the minimum permanent load that the engine can operate at is 65%; in the short-term (up to four hours), it can operate at a 50% load. The problem of increasing the ambient temperature is also linked to the increasing temperature of the gas supply to the engine. There is no possibility of improving the efficiency of the

cooling system, as the installation of larger coolers is a costly and economically unjustified solution, and there is no possibility of artificially increasing the heat removal from the engine block. With these arguments in mind, cooling the air that entered the table coolers began to be used. This solution used garden sprinklers (which produced a water mist) that were installed under the table coolers. The sprinklers were actuated in sections according to the temperature rise in the motor-cooling system. Figure 2 shows the behavior of the engine as the ambient temperature rose – the throttle opening automatically increased, and the electrical power of the engine decreased.

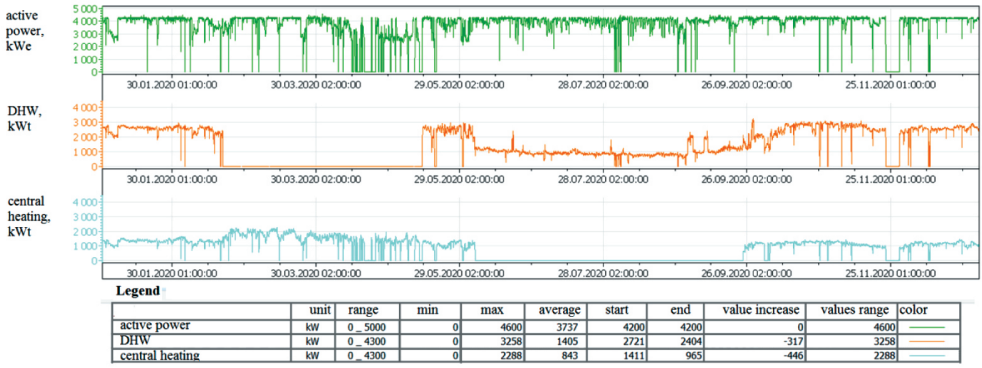

Legend

	unit	range	min	max	average	start	end	value increase	values range	color
active power	kW	0 _ 5000	0	4600	3737	4200	4200	0	4600	
DHW	kW	0 _ 4300	0	3258	1405	2721	2404	-317	3258	
central heating	kW	0 _ 4300	0	2288	843	1411	965	-446	2288	

Fig. 1. Graph of changes in thermal power that what discharged to district heating network in 2020

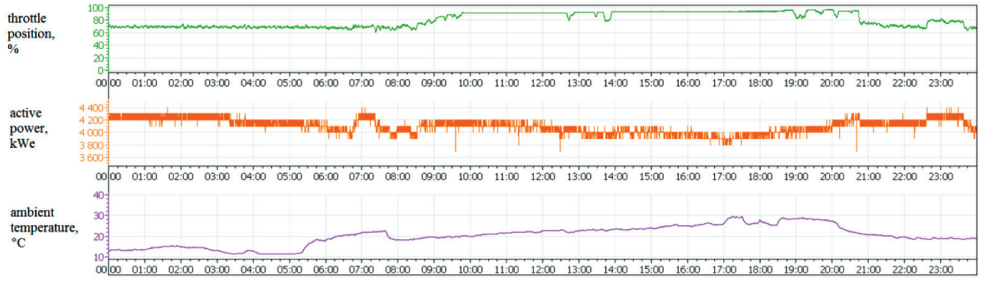

Legend

	unit	range	min	max	average	start	end	value increase	values range	color
throttle position	%	0 _ 100	60,7	96,9	80,9	68,6	70,3	1,7	36,2	
active power	kW	3500 _ 4500	3700	4400	4103	4300	4100	-200	700	
ambient temperature	°C	10 _ 40	11.3	29.5	20.3	12.8	19.3	6.5	18.2	

Fig. 2. Gas engine operation without running sprinkler system

Figure 3 shows the behavior of the engine with the sprinkler system running. It is characteristic that the throttle opening also increased as the ambient temperature rose; in this case, however, no such sharp drop in the engine load could be seen. Another parameter that affected the operation of the gas engine was the variable feed gas temperature, which ranged from –4.4°C (in 2017) to 38.5°C (in 2018).

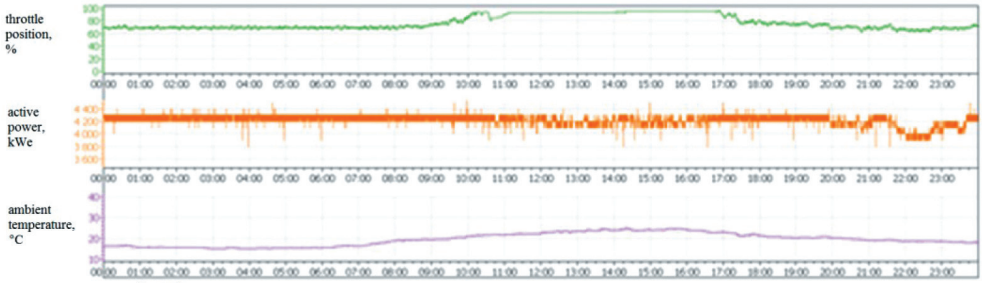

Legend

	unit	range	min	max	average	start	end	value increase	values range	color
throttle position	%	0 _ 100	61.6	96.0	77.7	70.6	71.4	2.8	34.4	
active power	kW	3500 _ 4500	3800	4600	4221	4200	4200	0	800	
ambient temperature	°C	10 _ 40	15.0	25.1	19.5	16.3	18.1	1.8	10.1	

Fig. 3. Gas engine operation with running sprinkler system

5. Summary

The operational availability of a gas engine is influenced by factors such as the amount of gas that is available, breakdowns, and service inspections, among others. The power availability of an engine depends on a great number of conditions, such as the amount of available gas, the gas parameters (concentration, gas temperature), the technical condition of the engine (the cleanliness of the cooling system and the gas and air filters), and the amount of the heat removal depending on the external temperature (Laskowski, Smyk 2020)

Some of the above-mentioned factors can be modified, while there is no influence on others; therefore, it must be assumed that this is the nature of the installation.

The optimum operating system for a gas engine would be year-round heat extraction (used for heating in winter and cooling in summer).

REFERENCES

Laskowski R., Smyk A., 2020, *Współczesne zagadnienia termodynamiki*, Oficyna Wydawnicza Politechniki Warszawskiej, Warszawa.

Moran M.J., Shapiro H.N., Boettner D.D., Bailey M.B., 2014, *Fundamentals of Engineering Thermodynamics*, 8th Edition, Wiley.

Analysis of methane as energy fuel – operational issues

Adam Kalwar ORCID ID: 0000-0572-1019-4354

PGNiG Termika Energetyka Przemysłowa S.A., Jastrzębie-Zdrój
email: adam.kalwar@termika.pgnig.pl

Krzysztof Pytel ORCID ID: 0000-0002-1924-8351

AGH University of Science and Technology
Faculty of Mechanical Engineering and Robotics
Department of Power Systems and Environmental Protection Facilities, Krakow
email: krzysztof.pytel@agh.edu.pl

Franciszek Kurdziel ORCID ID: 0000-0572-1019-6083

PGNiG Termika Energetyka Przemysłowa S.A., Jastrzębie-Zdrój
email: franciszek.kurdziel@termika.pgnig.pl

Grzegorz Grzywnowicz ORCID ID: 0000-0007-2336-5439

PGNiG Termika Energetyka Przemysłowa S.A., Jastrzębie-Zdrój
email: grzegorz.grzywnowicz@termika.pgnig.pl

Mykhaylo Melnyk ORCID ID: 0000-0002-8593-8799

Lviv Polytechnic National University
Institute of Computer Science and Information Technologies
Department of Computer-Aided Design Systems, Lviv
email: mykhaylo.r.melnyk@lpnu.ua

ABSTRACT

Issues that are related to the operation of cogeneration generators that are powered by gas engines that use mine gas as a fuel are presented. Gas engines are increasingly being used to drive electric generators; in such an application, gas is used as a fuel, whether it is mine gas, coke oven gas, septic tank gas, or mains natural gas. In an area where coal is mined, mine gas is commonly used as a fuel to power combined heat and power (CHP) generators. The use of mine gas as a fuel is highly desirable – both for environmental and economic reasons. The benefits and difficulties of using this gas as a fuel are presented.

Keywords: power systems, environmental protection facilities, process control, computer applications in engineering

1. Introduction

Over the years, gas engine-driven cogeneration units that use mine gas as a fuel have been installed in district heating and CHP plants. The first such installations produced electricity and heat in cogeneration, thus reducing the combustion of gas in gas-fired boilers or adapted water boilers. The engines that were built in a heat plant could be trigeneration units, producing cooling energy for the air-conditioning system of the mine workings in addition to electricity and heat. The gas installations of these engines require a gas that is better purified than those of the boilers; however, gas purification is carried out by filters that are built into the gas engine installations. The gas that is fed into a gas engine flows first through a paper gas filter, which removes dust, sand, and rust; at the next stage, it passes through a non-woven filter that was designed to remove impurities that are not caught in the general filter. To a lesser extent, contamination of the fabric and paper filters also causes reduced engine performance and problems with starting. In the long term, oil contamination through the gas-treatment system into the fuel supply path causes contamination of the flame arresters, which are built inside the cylinder heads. Contamination of the paper and fabric filters necessitates shutting down the engine, but the filter-replacement procedure itself ranges from 30 minutes (for fabric filters of gas paths) to 120 minutes (when replacing paper filters). On the other hand, the fouling of the flame arrestors involves a longer engine shutdown; the procedure for removing contaminated flame arresters itself requires the disassembly of the entire fuel supply system to the cylinders. Cleaning the flame arresters is also a lengthy process; if a set of clean interrupters is available, the repair time is shorter. As an example, the cleaning time for an engine intake system can be as high as about 200 man-hours, using a set of remanufactured (i.e., chemically cleaned) interrupters (Moran et al. 2014).

2. Gas composition analysis

From the beginning of the gas network operation, the composition of the mixture was monitored only in terms of the concentration of pure CH_4 in the mixture. The methane content in the mixture was measured with stationary methane meters at the mine demethanation facilities and at the individual plants that consumed mine gas. In addition, the CH_4 content of the mixture was measured three times a day (and even more frequently if necessary) with hand-held methane meters. Since 2014, the gas composition has been monitored at individual intakes and offtakes nonstop using chromatographs. This solution makes it possible to determine the gas quality and the variability of its composition very accurately over any time horizon. As part of the analysis of mine gas quality (in terms of the content of pure methane in the mixture), the concentration of methane was examined at the intake with the lowest average concentrations and the intake with the highest methane contents. The selected CHP plant was taken as the gas offtake point.

Analyzing the results, it can be seen that a great difference in concentration in the intake of up to 30% does not significantly affect the quality of the gas in the source, where the average concentration in 2019 was 54.3%. Intakes that have a decisive influence on the quality of the mixture that is supplied as fuel for gas engines were selected for the analysis. Figure 1 shows that the concentration of the JasMos intake is quite stable at around 70%, while the concentration of the Pniówek intake is significantly lower and has greater variability. However, it can be assumed that such changes in the concentrations in both intakes are significantly influenced by the exploitation of the deposits.

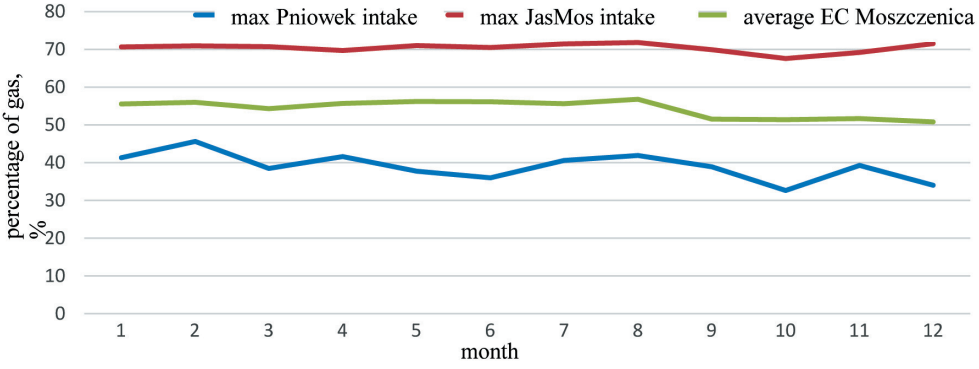

Fig. 1. Graph of methane concentration variation in 2019 depending on intake

Figure 2 shows the proportion of gas with a concentration above 60% of pure CH_4 in the mixture; this value averaged around 40% in the year under review. This 40% is a gas with a fairly constant composition and low dynamics of change, which has a strong influence on the stable composition of the gas mixture from the different intakes.

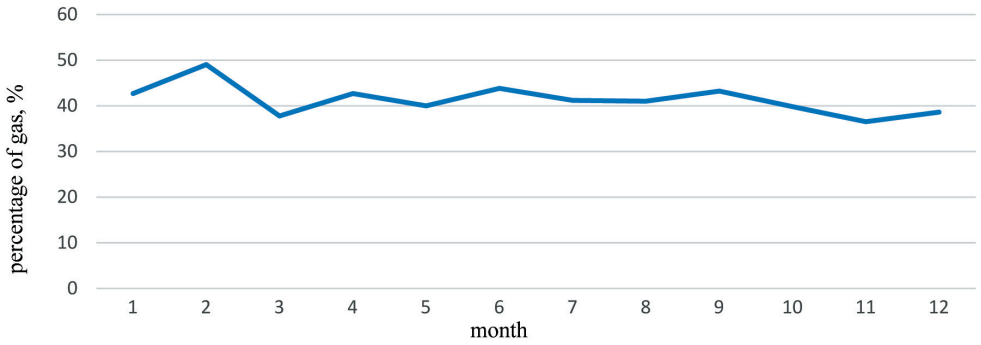

Fig. 2. Graph of percentage of gas with concentration above 60% in mixture

From Figure 3, it can be observed that, on September 5, 2019, one of the lowest gas concentrations was recorded in the gas engine feeder pipeline (i.e., 38.1% of methane in the mixture). This was an instantaneous value and did not cause any anomalies in the operation of the gas engine – the engine load was 100%, and the throttle opening ratio was 71% (a value that was as correct as possible). The only visible change in the engine performance with the changes in the concentration was the periodically changing amount of gas that was burned.

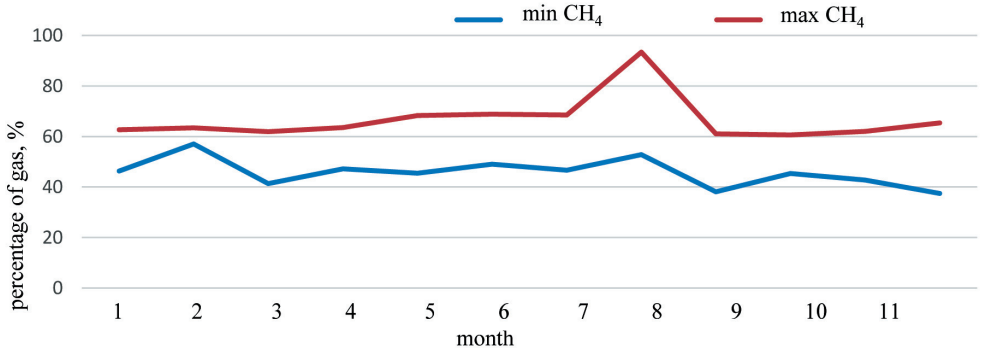

Fig. 3. Min and max concentrations on supply in 2019

3. Analysis of engine operating parameters

Figure 4 shows a graph of the engine load [kWe] and throttle opening rate [%]. The graph covers the period before replacing the filters in the gas paths to the individual cylinder rows. It can be seen that the load before and after the replacement of the filters remained at a level around 95–100%, and the throttle opening ratio was even higher than before after the replacement of the filters. The filters were changed six times in 2019; each time, there was no visible change in the parameters before and after the filter changes.

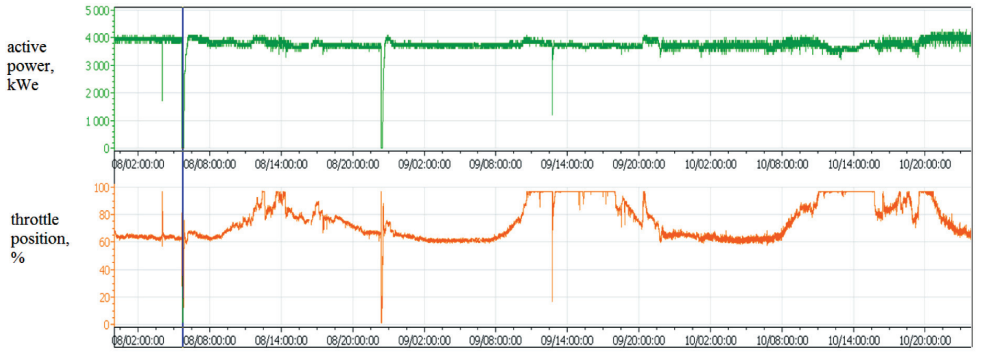

Legend

	unit	range	min	max	average	start	end	value increase	values range	color
active power	kW	0 _ 5000	0	4300	3579	4000	3800	-200	4300	
throttle position	%	0 _ 100	60,7	96,9	80,9	66	67	0.8001	96.3	

Fig. 4. Comparative graph of engine load and throttle opening rate after replacing filters on gas paths

The cleaning of the flame arrestors and the engine intake system was performed with a spare set of flame arrestors (a set of flame arrestors that were already used but after chemical cleaning). The required downtime for such an operation was from November 15–23, 2020, from 8:00 a.m. to 4:00 p.m., which totaled of 200 engine operating hours. During this downtime, turbocharger inspections were also performed.

Another service treatment that was related to the quality and contamination of the gas fuel was the cleaning of the engine intake system with the replacement of the flame arrestors. Figure 5 shows the power load of the engine and the throttle opening ratio a significant decrease in the throttle opening for the same power can be seen at first glance.

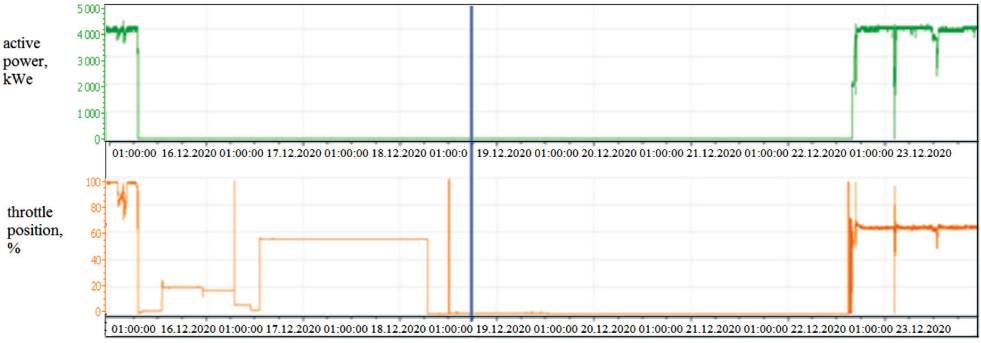

Legend

	unit	range	min	max	average	start	end	value increase	values range	color
active power	kW	0 _ 5000	0	4300	716	4000	4000	0	4300	
throttle position	%	0 _ 100	0	100	25	96	63	-33	99.7	

Fig. 5. Comparative graph of engine load and throttle opening rate after cleaning intake system and replacing flame arresters

Before the engine was put aside for cleaning, it could be seen that it had been running with the throttle opening of between 80 and 100%, and the power was at a level of 90–95% (as shown in Figure 6). A number of adjustment attempts and other diagnostic procedures were carried out, but these did not produce the desired results. The decision to clean the intake system was the correct one. The state of the cleanliness of the intake system is best illustrated in Figures 4–6.

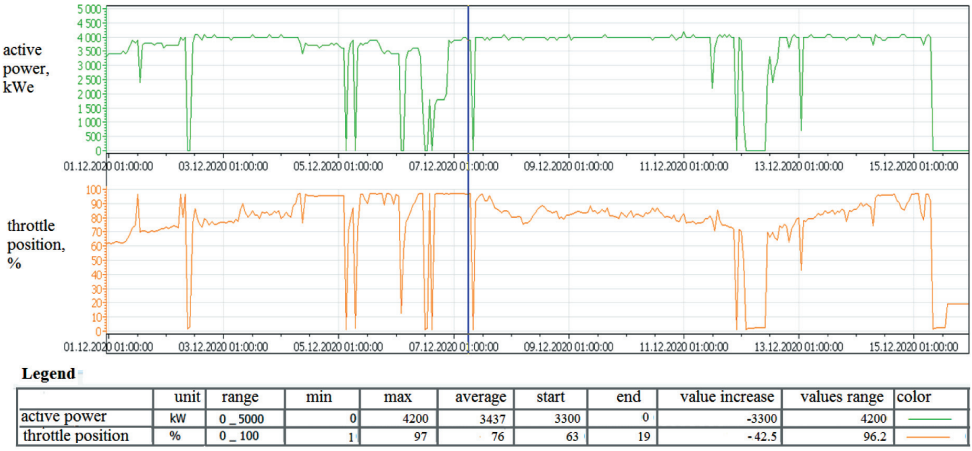

Legend

	unit	range	min	max	average	start	end	value increase	values range	color
active power	kW	0 _ 5000	0	4200	3437	3300	0	-3300	4200	
throttle position	%	0 _ 100	1	97	76	63	19	-42.5	96.2	

Fig. 6. Comparative graph of engine load and throttle opening rate after cleaning intake system and replacing flame arresters

Summarizing the results of the analyses, the following conclusions can be made:

– Changes in the concentration of the gas on the engine power supply – the changes in the concentration of the gas for combustion did not have a major impact on the operation of the gas engine; the engine control system quickly and efficiently coped with sufficiently over-regulating the engine and maintaining the preset power. The system of several interconnected gas supply sources had a positive effect on the stable operation of the entire gas network. There were no frequent nor abrupt changes in the concentration; if such a situation occurred, these were purely emergency cases.
– Contamination of filters on the gas system – the gas-filtration system perfectly coped with solid impurities; any contamination of the gas filters did not significantly affect the power availability of the engine. If it was necessary to replace the filters, the process was not a lengthy or complicated procedure (even though it required the engine to be shut down).
– Oil-borne impurities – due to the design of the compressors that are used in mine de-metalation facilities, oil-borne impurities enter the gas and, together with the moisture that is condensed from the gas (the pipeline runs along overhead catena-

ries as well as in the ground for the most part), resulted in the formation of impurities in the oil-water mixture; these were not captured by the required filtering equipment. These impurities reached as far as the cylinders, causing a gradual fouling of the flame arresters; this in turn caused a continuous reduction in the engine's power availability during the final stage (Laskowski, Smyk 2020).

4. Summary

Fossil gas is a fairly good fuel for electric power equipment; however, a rather sophisticated technical infrastructure is required to manage it in an optimal way.

REFERENCES

Laskowski R., Smyk A., 2020, *Współczesne zagadnienia termodynamiki*, Oficyna Wydawnicza Politechniki Warszawskiej, Warszawa.

Moran M.J., Shapiro H.N., Boettner D.D., Bailey M.B., 2014, *Fundamentals of Engineering Thermodynamics*, 8th Edition, Wiley.

Analysis of compressor units – operational issues

Franciszek Kurdziel ORCID ID: 0000-0572-1019-6083

PGNiG Termika Energetyka Przemysłowa S.A., Jastrzębie-Zdrój
email: franciszek.kurdziel@termika.pgnig.pl

Krzysztof Pytel ORCID ID: 0000-0002-1924-8351

AGH University of Science and Technology
Faculty of Mechanical Engineering and Robotics
Department of Power Systems and Environmental Protection Facilities, Krakow
email: krzysztof.pytel@agh.edu.pl

Adam Kalwar ORCID ID: 0000-0572-1019-4354

PGNiG Termika Energetyka Przemysłowa S.A., Jastrzębie-Zdrój
email: adam.kalwar@termika.pgnig.pl

Grzegorz Grzywnowicz ORCID ID: 0000-0007-2336-5439

PGNiG Termika Energetyka Przemysłowa S.A., Jastrzębie-Zdrój
email: grzegorz.grzywnowicz@termika.pgnig.pl

Andriy Zdobytskyi ORCID ID: 0000-0001-8044-9593

Lviv Polytechnic National University
Institute of Computer Science and Information Technologies
Department of Computer-Aided Design Systems, Lviv
email: andrii.y.zdobytskyi@lpnu.ua

ABSTRACT

The characteristics of compressor chiller operation for the generation of cooling for the central systems of mine air-conditioning installations are presented. The modes of operation of the units and their use in the final stage of chilled-water cooling are described. The construction of the screw compressor and the compression methods are discussed. The actual use of compressors in the third stage of chilled water generation is analyzed. The free-cooling installation as a solution for supporting chilled-water generation is presented.

Keywords: free cooling, thermodynamic cycles, coolness generation, compressors

1. Introduction

A compressor's refrigeration cycle belongs to the group of left-handed thermodynamic cycles. The most commonly used cycle is the compressor/evaporator circuit. Such a circuit consists of four units: two heat exchangers (i.e., an evaporator and a condenser), a compressor, and a throttling valve. In each of these, one thermodynamic process is carried out. In the evaporator, the evaporation of the circulating medium takes place as a result of heat extraction from space or the refrigerant. Frequently, there is also a slight superheating of the steam. The vapor is then transferred to the compressor, where it is compressed to increase the pressure (condensing pressure). The compressor cooler is driven by electricity. The effect of the compression process is raising the temperature of the steam to a point where heat can be transferred to the environment or the cooling medium. In the condenser, the vapor is initially cooled to a saturated state and then condensed (possibly subcooled). In the throttling valve, the resulting liquid is expanded through an isenthalpic process to a lower pressure (evaporation pressure), as is shown in Figure 1 (Moran et al. 2014). The characteristic transformations that occur in a compressor chiller are as follows: 1–2 – adiabatic irreversible compression; 2–3 – condensation; 3–4 – isenthalpic throttling; 4–1 – evaporation. Figure 2 shows the Linde cycle in the T-s system. Due to the occurrence of friction (which causes drops in pressure) and the uncontrolled heat exchange of the system with its surroundings, an actual compressor circuit differs from a theoretical circuit.

The energy efficiency ratio of a compressor chiller is described by the following formula:

$$COP_z = \frac{Q_L}{W_{in}} = \frac{Q_H - W_{in}}{W_{in}} \tag{1}$$

where:

Q_L – heat input in evaporator [W],
Q_H – heat output in condenser [W],
W_{in} – compressor drive energy [W].

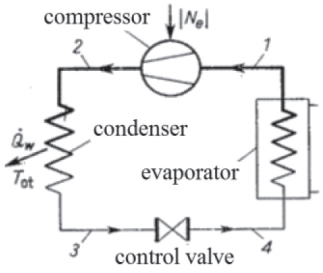

Fig. 1. Diagram of compressor chiller cycle. Explanation in text

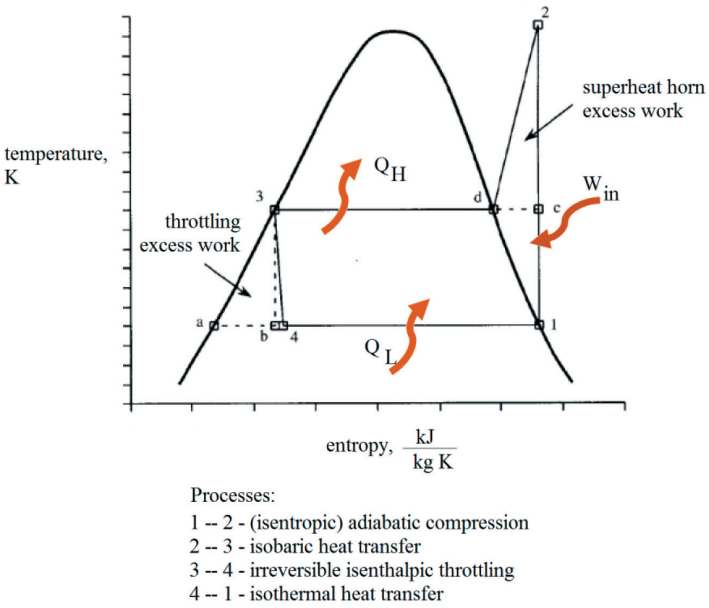

Fig. 2. Theoretical compressor refrigeration diagram (Linde diagram)

Circulating refrigerants for compressor chillers should be non-corrosive, non-toxic, non-flammable, chemically stable, have low evaporation temperatures, and have low GWP (global warming potential) values. Good thermodynamic properties are presented by aliphatic hydrofluorocarbon compounds called CFCs. Some of these have been phased out due to their destructive environmental impact. Alternative agents are azeotropic and zeotropic solutions, which are mixtures of homogeneous refrigerants that have respectively similar (no temperature slippage) or different (temperature slippage) evaporation and condensation temperatures. Commonly known and available chemicals also include propane, isobutane, ammonia, water, and carbon dioxide. Compression chillers have the advantage of a high energy-efficiency value (above unity) as compared to absorption chillers (below unity) (Moran et al. 2014).

2. Gas compression in compressor unit

A compressor (shown in Figure 3) is the basic component of a compressor unit. The main parts of the compressor are a body that is cast in quality cast steel and is suitably machined, bearings (for transmitting the radial and axial forces that arise from the rotors to the body during the compressor's operation), a capacity control mechanism (the main element of which is a control slider that slides in a suitably shaped cylindrical part of the body), a shaft seal assembly (which includes a stuffing box), a pair of rotors (which typically have an asymmetrical cross-section), and a main rotor (which is driven by the main drive shaft and has fewer teeth, while an auxiliary impeller has more teeth).

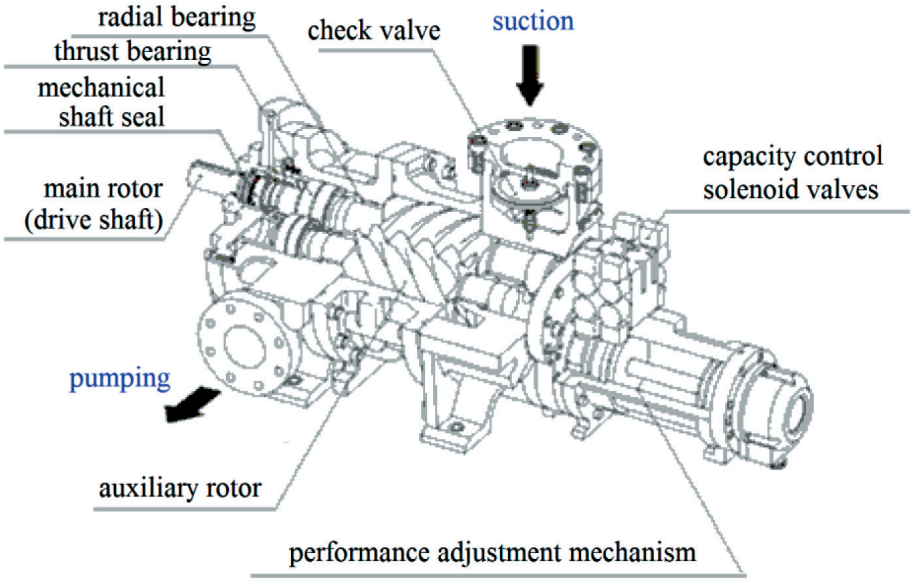

Fig. 3. Construction of screw compressor

The compressor rotors differ in the numbers and profiles of their teeth. The space between the teeth of the main and auxiliary rotors and the compressor housing enlarges on the suction side as the rotors rotate. When this space is at its largest, gas is trapped between the inter-tooth space and the compressor housing. With a further rotation of the rotors, the inter-tooth space is reduced toward the discharge port. The space between the rotor teeth and the compressor housing is reduced to a precisely defined size at the discharge port. A further rotation of the rotors causes the compressed gas to be ejected through the discharge port outside the compressor (Laskowski, Smyk 2020).

3. Operation of refrigeration installation

The ammonia refrigeration installation of the sixth stage of the combined system at the described CHP plant (shown in Figure 4) was made to cool the mine's return water to a temperature of about +1.5°C in an integrated refrigeration unit (with ammonia as the working medium).

The constructed water chiller acts as a supplementary system, which will be switched on when it is not possible to cool the water to the desired temperature of +1.5°C by the existing free cooling system and the existing absorption-compressor systems (as shown in Figure 5).

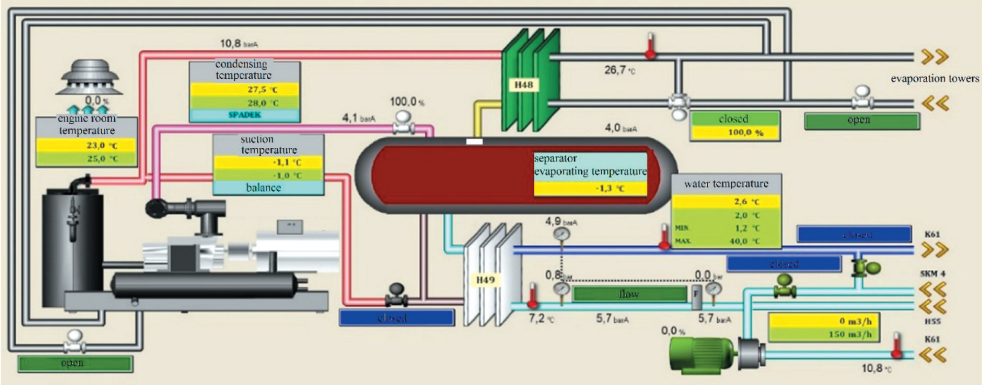

Fig. 4. Compressor cooler installation

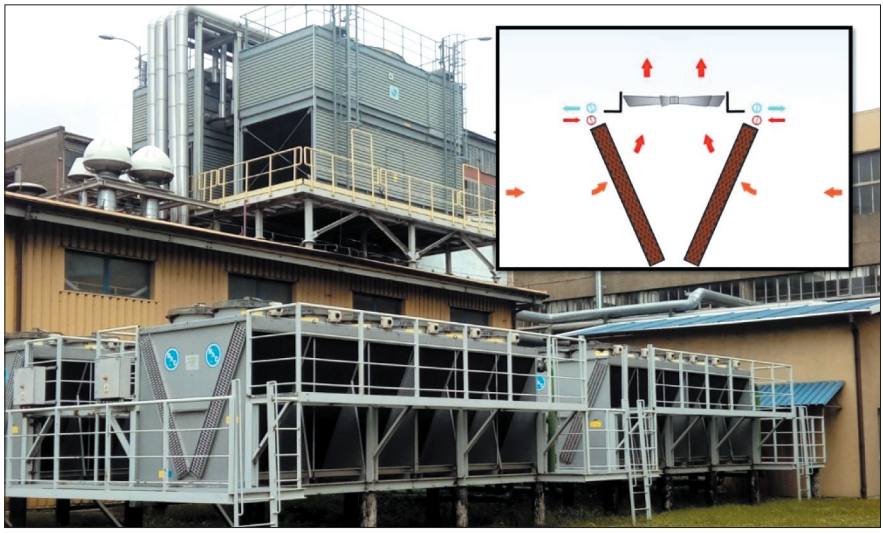

Fig. 5. Compressor cooler installation

If the hot water is not cooled to the desired temperature after passing through the existing absorption-compressor systems, shut-off valves with an actuator should automatically close the inflow of water to the cold chamber of the mine's water-pumping system and direct this water to the ammonia water cooling system (where the water will be cooled to the desired temperature of +1.5°C). The cooling of the water in the system is carried out in a plate heat exchanger in which ammonia circulates on one side and the cooled water from the mine circulates on the other. The exchanger is fed by gravity with liquid ammonia from a horizontal liquid separator, from which a compressor extracts dry NH_3 vapors; this maintains the required refrigerant evaporation temperature.

In the plate heat exchanger, the water is precisely cooled to a set point of +1.50°C, with an ammonia evaporation temperature of –10°C (as shown in Figure 4). The purpose of this system is to safely and steadily cool the water to the required temperature. This system has exchanger frost protection. During the autumn/winter/spring period when the outside air temperature drops below the mine's return water temperature, the new compressor cooling system is assisted by the existing free cooling system. When the water reaches the preset temperature of +1.50°C after cooling in the free cooling system, it is routed directly into the cold chamber; from here, the secondary pumps force it into the feed pipe of the three-chamber feeder. If the water does not reach the preset temperature of +1.50°C due to unfavorable weather conditions, it is redirected to the warm chamber and cooled in the compressor cooling units. The compressor cooling unit (chiller) is installed in a machine room that is prepared for this purpose (a dedicated enclosure). An SKM6 compressor unit draws in dry ammonia vapors from the liquid separator at a temperature of –10°C. The liquid ammonia that is contained in the liquid separator at –10°C gravitationally feeds the ammonia/water plate exchanger in which the flowing mine water is cooled. After leaving the exchanger, the water reaches a temperature of approximately +1.50°C. The ammonia that has evaporated in the exchanger returns to the liquid separator, where the liquid is separated from the ammonia vapors. The water that is cooled in the SKM chiller is pumped further into the mine circuit. The liquid separator is supplied with liquid ammonia from a condenser (plate heat exchanger) that is cooled by the processed water. The water system for cooling the ammonia condensers is a pressurized system in which a storage vessel is responsible for compensating for changes in the volume of the medium with a change in its temperature. An adequate flow of glycol in the system is ensured by a circulating pump. The compressor unit is enclosed by sandwich panels; the purpose of this enclosure is to soundproof and functionally isolate the ammonia systems from the rest of the equipment. The ammonia-refrigeration room is equipped with a residential ventilation system to ensure the removal of the heat gains from

the screw compressors as well as emergency ventilation and an ammonia-detection system. To protect against the effects of a possible ammonia leak in both rooms, the NH_3 content in the air (in units of ppm) is continuously measured via a detector head and transmitted to the central unit.

4. Summary

The operation of the system is fully automatic and fully interoperable with the existing free cooling systems as well as the existing absorption and compressor systems. All of the parameters of the ammonia and water installations (pressures, temperatures, coolant levels, equipment operating states, and the ammonia compressor and water pump capacities) are continuously displayed, monitored, and archived by the central controller, which controls the operation of all of the refrigeration and water systems.

REFERENCES

Laskowski R., Smyk A., 2020, *Współczesne zagadnienia termodynamiki*, Oficyna Wydawnicza Politechniki Warszawskiej, Warszawa.

Moran M.J., Shapiro H.N., Boettner D.D., Bailey M.B., 2014, *Fundamentals of Engineering Thermodynamics*, 8th Edition, Wiley.

Analysis of processes that take place in absorber of absorption chiller

Mykhaylo Lobur ORCID ID: 0000-0001-7516-1093

Lviv Polytechnic National University
Institute of Computer Science and Information Technologies
Department of Computer-Aided Design Systems, Lviv
email: mykhaylo.v.lobur@lpnu.ua

Franciszek Kurdziel ORCID ID: 0000-0572-1019-6083

PGNiG Termika Energetyka Przemysłowa S.A., Jastrzębie-Zdrój
email: franciszek.kurdziel@termika.pgnig.pl

Krzysztof Pytel ORCID ID: 0000-0002-1924-8351

AGH University of Science and Technology
Faculty of Mechanical Engineering and Robotics
Department of Power Systems and Environmental Protection Facilities, Krakow
email: krzysztof.pytel@agh.edu.pl

Adam Kalwar ORCID ID: 0000-0572-1019-4354

PGNiG Termika Energetyka Przemysłowa S.A., Jastrzębie-Zdrój
email: adam.kalwar@termika.pgnig.pl

Grzegorz Grzywnowicz ORCID ID: 0000-0007-2336-5439

PGNiG Termika Energetyka Przemysłowa S.A., Jastrzębie-Zdrój
email: grzegorz.grzywnowicz@termika.pgnig.pl

ABSTRACT

Methods of using absorption chillers are presented based on the example of a mine air-conditioning system. This paper presents the application of the possibility of using thermal energy as a waste product that results from the combustion of gas (methane; CH_4) in gas engines and the process of its processing into the production of a cooling medium. The principle of the operation of an absorption chiller is described – the processes in the absorber, the physicochemical changes in the system, and the method of producing chilled water. The actual application of cascade-connected refrigeration devices is presented in order to achieve a final product with specific parameters.

Keywords: free cooling, thermodynamic cycles, cold production, compressors

1. Introduction

As a related system in the analyzed mine, the energy and cooling system consists of several technological lines that were built in stages. The installations were created in such a way that it was possible to increase the cooling capacity in the case of increased demand. The first two technological lines included a gas engine with an electric power of 3.2 MW_{el} and a thermal power of 3.7 MW_t, two absorption chillers, and a compressor chiller with a cooling capacity of 2.5 MW_{ch}. The total cooling capacity that the system could generate is 5 MW_{ch}. At individual stages of the installation expansion, a third gas engine was launched with electric and thermal power of 3.9 MW_{el} and 4.3 MW_t, respectively. The cooling system that is shown in Figure 1 was built on the basis of heat recovery from a gas engine – a heat-recovery system from exhaust gases, and a heat-recovery system from the engine body.

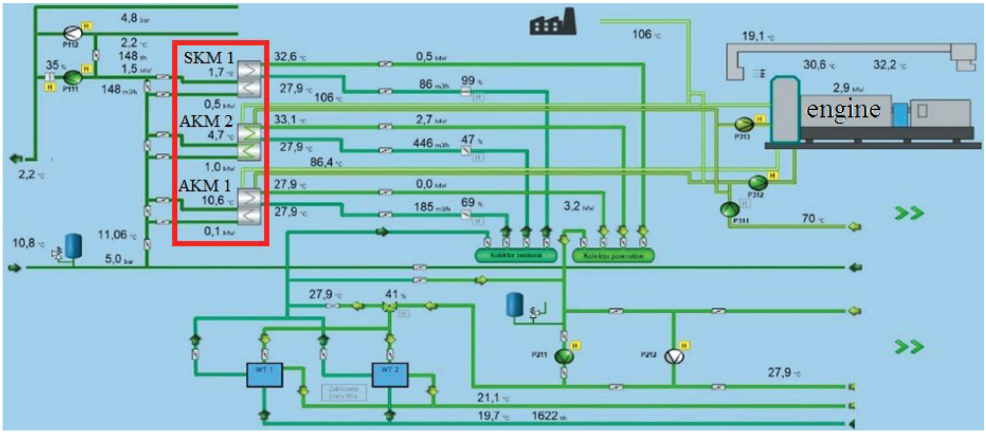

Fig. 1. Cooling system based on heat from gas engine

The heat exchange between the recovery systems is based on water heat exchangers (as shown in Figure 2). Heated water from the waste heat of a gas engine with a temperature of up to 130°C is used as an energy source in absorption chillers to produce cold water.

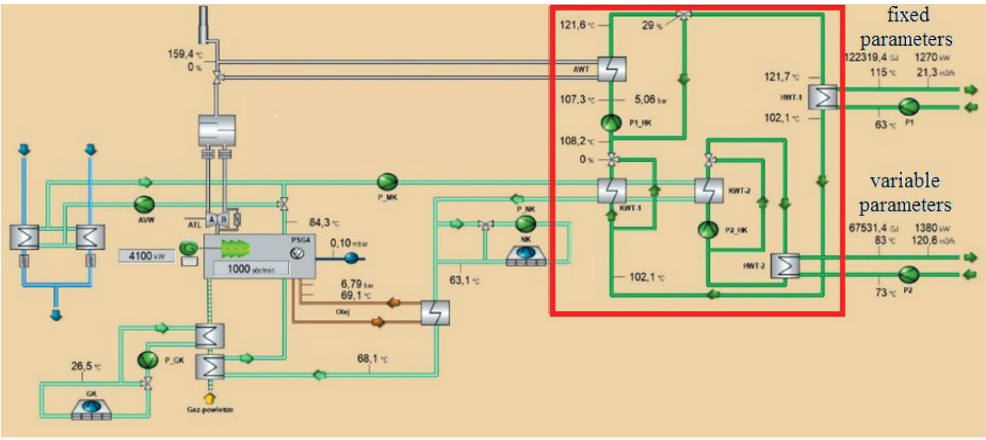

Fig. 2. Heat-recovery system from exhaust gas system and engine body: media distribution through heat exchangers in marked area

2. Cooling system

The general concept of the applied solution is to generate electricity in generators that are powered by gas piston engines using depleted methane from methane drainage in the mine, heat recovery from the engine body, and the exhaust gases of these engines; the transmission of cold with water at a temperature of approx. 1.5–2.0°C is produced in absorption refrigerators that are powered by the heat from gas engines and compressor refrigerators that are powered by electricity that is generated by generators. The chilled water that is sent down the mine after reducing the static pressure is directed to air coolers. The idea of the full association of the system provides for the priority of water cooling for the needs of the central mine air conditioning; therefore, the system is directly connected to the power and heating networks. In the absence of electricity generation or no heat being recovered from gas engines, the absorption chillers can be supplied from the district heating network, and the compressor chillers can be supplied from the power grid. However, with the proper operation of the system, it produces surplus electricity and heat (which are sold to power and heating networks).

The water-cooling system has three stages (as shown in Figure 1). Each segment uses different devices with different cooling powers. The first element of the system is

the AKM1 refrigerator, followed by the AKM2, and then the SKM compressor refrigerator in the final stage. The use of such a combination of devices ensures the stable operation of the system and its flexibility depending on the temperature of the water in the circuit. The water temperature at the outlet from the underground part of the mine is about 18°C. It flows through the first chamber (AKM1) with a capacity of 600 kW, where its temperature is reduced to 14.5°C. The cooler is used to fuel hot water that is obtained from the waste heat of the heat and power plant processes. In the next stage, the cooled water goes to the second refrigerator (AKM2) with a capacity of 1730 kW, where it is cooled to a temperature of 4.5°C. The last stage through which the cooled medium flows is the compressor cooler (SKM), which ultimately cools the water to a temperature of 1.5°C. The refrigerators that are used in the refrigerator system are bromolite devices ($LiBr + H_2O$) in which the absorber is a lithium bromide solution, while the refrigerant is composed of water (which reaches a temperature of 3°C as a result of the physicochemical processes that take place in the refrigerator.

A compressor cooler is an ammonia machine in which the working medium is ammonia and the absorber is water. Due to the harmfulness of ammonia, these devices operate in a closed system in separate chambers under the supervision of an ammonia-detection system with the use of emergency ventilation.

3. Operational problems – crystallization

Crystallization may occur in all absorption chillers that use lithium bromide and water as its solution and refrigerant. This is due to the fact that certain concentration levels of the liquid solution in certain areas of the system can only be obtained above the normal ambient temperature. The solution in a single-stage absorption unit generator typically contains 64.3% lithium bromide (by weight). LiBr solutions start to crystallize at 43.3°C; this crystallization occurs when the temperature of the LiBr solution becomes too low or the concentration is too high (then, the LiBr solution thickens). The LiBr solution then cannot absorb any more water and starts to solidify (crystallize). Crystallization takes place in the heat exchanger; this phenomenon can also occur in the generator. In addition, crystallization can occur in pipes that are not properly insulated and are located in rooms where the temperature can affect the solution that flows through the pipes. Crystallization can be prevented by keeping the solution temperature high and the optimum concentration percentage below 64%. Since the temperature of the solution in the generator is usually high enough to avoid crystallization, it is important to keep the temperature high. Before turning off the refrigeration unit, the solution must be sufficiently diluted in all areas of the system. This action helps

prevent crystallization during downtimes. Keep in mind that, after a while, the temperature of the solution will become equal to the ambient temperature. To avoid crystallization, a dilution cycle must be performed on this type of refrigeration equipment. Many chillers utilize a self-dilution system during a shutdown sequence to prevent crystallization during shutdowns. After carrying out the dilution cycle in an absorption chiller, the concentration of the solution will be less than 45% lithium bromide (by weight). Although the crystallization line (see graph) does not extend this far, it can be seen that a solution that is at a concentration of 45% will not crystallize at normal ambient temperatures.

The most common cause of crystallization is power failure. If the power supply to the full load chiller is disconnected for a sufficiently long time, the concentrated solution on the high-pressure side of the unit will cool down (Laskowski, Smyk 2020). As a dilution cycle is not possible, the concentration of the solution in some areas of the assembly will still be high. If the temperature of the concentrated solution drops sufficiently, it will reach the crystallization point. The time that is required for crystallization is influenced by the room temperature, the quality of the insulation, and the concentration of the solution (Moran et al. 2014).

4. Summary

Common engineering practices list several steps that should be followed in order to successfully decrystallize the lithium bromide solution of an absorption chiller. The final sequence and durations of the individual activities depend on the place and degree of the crystallization. The main activity is to force the refrigerant from the evaporator of the device to the absorber in order to reduce the concentration of the diluted solution that is pumped into the generator. This operation is also called refrigerant regeneration or purification, as it removes the small but harmful content of lithium bromide in the refrigerant (thus contributing to an increase in the cooling capacity of the unit). This procedure is also one of the simplest methods of decrystallization, as it only consists of the manual or automatic opening of an appropriate drain valve for a period that is necessary for pumping the entire amount of refrigerant (while the refrigerant pump is running at the same time). A significant reduction in the concentration of the working solution of a device as a result of the complete regeneration of the refrigerant in the absence of crystallization may cause the refrigerator to heat the cold water instead of cooling it for a period of several minutes after its completion. This phenomenon occurs most often in systems with low cold water inlet temperatures, where the condensation temperature of the refrigerant in the evaporator is higher than

the cold water inlet temperature. The next stage after the pumping of the refrigerant is completed should be to start the lithium bromide pump in order to force the appropriate amount of it into the generator. In the next step, the feed medium (hot water) is opened in order to heat the lithium bromide to the appropriate temperature. These activities are performed with the cold water flow on and the cooling water flow stopped. When the required solution temperature in the generator is reached, the hot water supply is stopped, and the circulation of lithium bromide is stopped; this causes the hot solution to return from the generator to the absorber. After several times of starting, heating, and stopping the circulation of the solution, it is possible to heat the entire volume of the device in order to decrystallize it. The procedure that is described above is commonly used to remove the crystallization that is formed in the most likely place; i.e., inside the regenerative exchanger of the solution on its concentrated (concentrated) side. Failure to apply the above procedure means that the crystallization occurs over a wider area – also in the pipelines and pumps of the concentrated working solution that returns from the generator to the absorber of the device. In the case of crystallization inside a solution pump, an effective method of removing it is to dismantle its impeller and rinse its interior with hot water. In the case of the crystallization of the lithium bromide solution in its pipelines, it is necessary to heat them to the appropriate temperature by using an external heating medium.

REFERENCES

Laskowski R., Smyk A., 2020, *Współczesne zagadnienia termodynamiki*, Oficyna Wydawnicza Politechniki Warszawskiej, Warszawa.

Moran M.J., Shapiro H.N., Boettner D.D., Bailey M.B., 2014, *Fundamentals of Engineering Thermodynamics*, 8th Edition, Wiley.

Control system for experimental model of robotic mobile platform with manipulator

Vataliy Mazur ORCID ID: 0000-0001-9477-854X

Lviv Polytechnic National University
Institute of Computer Science and Information Technologies
Department of Computer-Aided Design Systems, Lviv
email: vitaliy.v.mazur@lpnu.ua

Sofiia Panchak ORCID ID: 0000-0001-6169-0533

Lviv Polytechnic National University
Institute of Computer Science and Information Technologies
Department of Computer-Aided Design Systems, Lviv
email: sofiia.panchak@lpnu.ua

ABSTRACT

The control system for a robotic mobile platform with a manipulator witch that moves on orthogonal routes is considered in this work. To ensure the required speed and accuracy of the platform positioning, the method for changing the speed of the drive stepper motors is proposed. Features of the manipulator control system are considered. Methods of eliminating collisions during the movements in several mobile platforms on the marked surface are offered.

Keywords: robotic mobile platform, orthogonal routes, control system, manipulator, speed control, elimination of collisions

1. Introduction

Robotic mobile platforms are being increasingly used in the automation of technological processes. In the production process, one of the important tasks is to move components or materials in the territory of a shop or warehouse. For the uniformity of movements of bulk materials, liquids, and small details, it is expedient to use standardized containers. Various robotic mobile platforms that are equipped with manipulators have been developed and widely used to automate the movements of such containers and their placements on racks (Shneier, Bostelman 2015). The main requirements for developing and improving such platforms are to ensure high positioning accuracy and the required speed of movement on specified routes. When moving mobile platforms on arbitrary trajectories, ensuring these requirements is associated with the complexity and increases in the cost of control systems, which hinders the widespread introduction of such platforms. To simplify the control system and traffic planning, an experimental model of a robotic mobile platform for moving on orthogonal routes was proposed in Mazur and Panchak (2021). The possibility of the joint movement of several such platforms on a common marked surface provides an advantage of the mobile platform over other alternative variants for moving a manipulator with a container (on the principle of crane-beams or 3D CNC machines). The use of stepper motors and toothed rails in these variants allows for the high speed of a carriage with a manipulator and the accuracy of the container positioning; however, they involve moving only one container and do not allow for the use of multiple manipulators when crossing their trajectories. A kinematic scheme of a mobile platform manipulator was considered in Mazur (2021), as was ensuring the accuracy of its positioning when moving containers.

Since the mechanical part of a mobile platform significantly depends on the masses of containers and the speeds of their movements, the main attention in this work was paid

to studying and improving the control system of a mobile platform. In particular, this paper considered the problems of providing the movement of a platform with variable speeds to increase the accuracy of the positioning and ensure the joint movement of several platforms.

The purpose of the current work is to improve the control system for robotic mobile platforms with a manipulator and develop methods for planning their joint movements on orthogonal routes based on research of an experimental model.

To achieve this goal, the following tasks were solved in the work:

1) The development of methods for improving the positioning accuracy of the mobile platform on orthogonal routes based on controlled changes of the speeds of drive stepper motors.
2) Further improve route-planning methods to avoid collisions of multiple platforms that move together on a common marked surface.

2. Stepper motor speed control

Eliminating dynamic overloads and skipping steps (to ensure the required positioning accuracy) are based on the controlled smooth change of a stepper motor's speed (Fig. 1).

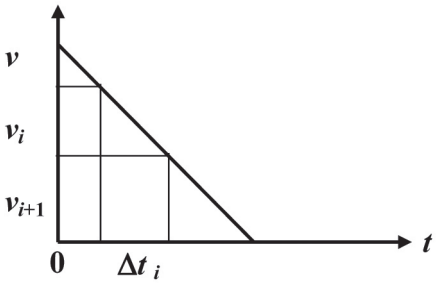

Fig. 1. Dependence of speed on pulse duration

To determine pulse duration Δt_i, which varies for each step of the motor during deceleration and acceleration, the following formula is proposed:

$$v_{i+1} = v_i + a \times \Delta t_i \tag{1}$$

where:

a – set deceleration (–3 cm/s^2),
v_i – initial value of platform speed (v_i = 3 cm/s),
v_{i+1} – value of platform speed after time Δt_i.

The distance s that the platform passes in one step of the motor is as follows:

$$s = \frac{(v_{i+1} + v_i) \times t_i}{2} = \frac{\pi \times d \times n}{k} \tag{2}$$

where:

d – diameter of wheel (38 mm),
n – number of gearbox shaft revolutions per second (0.25 rps),
k – number of pulses per one revolution of motor shaft (512 ppr).

At the specified values of d, n, k for the selected stepper motor with a reducer, the value of s will be equal to 0.058 mm/step.

Using Relationships (3) and (4), an array of Δt_i values (i = 1 to 256) are determined; these are used by the controller to generate pulses.

$$a \times \Delta t_i^2 + 2 \times v_i \times \Delta t_i - 2 \times s = 0 \tag{3}$$

$$\Delta t_i = \frac{-v_i + \left(v_i^2 + 2 \times s \times a\right)^{\frac{1}{2}}}{a} \tag{4}$$

Step motor pulse duration Δt_a, Δt_d and change of equivalent speed v_a, v_d (when accelerating and decelerating the mobile platform) are shown in Figure 2.

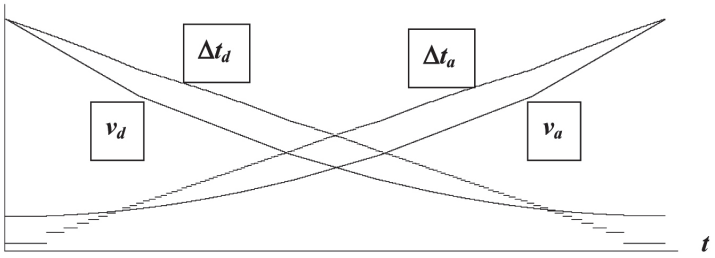

Fig. 2. Duration of stepper motor pulses and change in equivalent speed during acceleration and deceleration of the moving platform

3. Collisions elimination of several platforms

To plan the movements of several platforms and eliminate collisions between them, the marked surface is divided into zones of a size of 21 cm × 21 cm (Fig. 3). The size of the zone is determined by the size of the mobile platform (after taking a gap of 0.5 cm into account). The size of the buffers for storing 24 containers is 20.5 cm × 20.5 cm. To replenish the storage and issue containers to users, terminals of 20.5 cm × 4 cm are used with

a capacity of five containers. Mobile platforms provide the movements of the containers between the terminals and buffers (while storing them in the warehouse) or between the buffers (the movements of containers between workplaces).

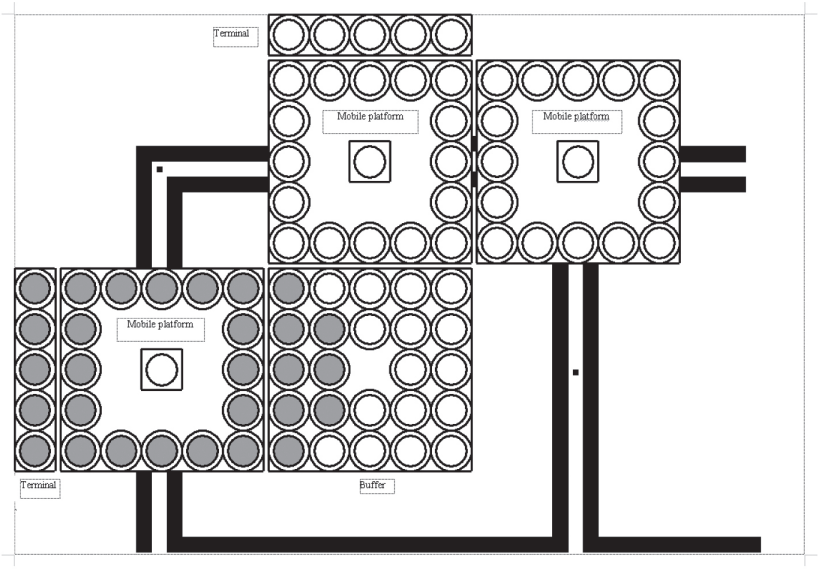

Fig. 3. Division of marked surface into zones

Appearance of manipulator with containers is presented in Figure 4.

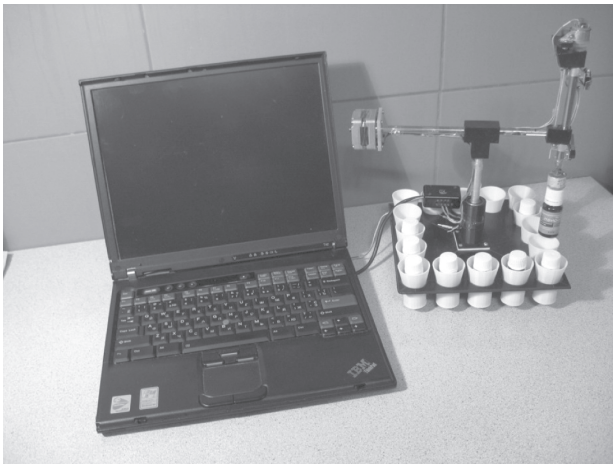

Fig. 4. Manipulator construction for mobile platform with containers

The proposed kinematic scheme of the manipulator (see Mazur 2021) provides the movements of the containers in 3D space and the required accuracies of their positioning.

The required angle of rotation of the vertical axis is provided by a stepper motor with a step of 0.9 deg. The length of the retractable horizontal beam is changed by using a stepper motor and a worm gear with an accuracy of 0.5 mm (after taking the backlash into account). The movement of the vertical retractable rod at the end of the beam is carried out by a servomotor with using tactile sensors. The electromagnet at the end of this rod ensures the captures and releases of containers with metal lids.

The process of moving the containers consists of two cycles:

1) At the giving of a control starting pulse and the switched-off electromagnet by means of the stepper motors, the necessary horizontal coordinates of a vertical rod are established. Then, the rod is lowered to the contact of the electromagnet with the container lid (which is fixed by a tactile sensor). The electromagnet is turned on, and the container is captured. Then, the rod rises to the upper position (which is determined by the limit switch).
2) By means of the stepper motors, the new position of the rod is established, and its lowering to contact of the container with a bottom of a nest (which is fixed by the tactile sensor) is carried out. The electromagnet is switched off, and the rod rises to the upper position.

To limit the length of the retractable horizontal beam of the manipulator (which determines the accuracy of the positioning of the container) only those containers in the buffer that are near the mobile platform are loaded and selected (see Fig. 3). The accurate positioning of the platform that is opposite of the buffer or terminal is provided by markers (the distance between which is 21 cm). Markers also provide the accurate positioning of the platform at intersections to change the directions of movements by 90 degrees.

The temporal-spatial relationships that describe the movement of the platform between the markers are presented in Figure 5. If the platform moves from one marker to an adjacent one, the movement time is 8 s (1 s is a movement with an acceleration of 3 m/s^2, 6 s is a movement with a nominal speed of 3 m/s, and 1 s is a movement with a deceleration of –3 m/s^2). If the platform moves between two markers without stopping at the nominal speed of 3 m/s, then the movement time is 7 s. The alignment of the platform centers and the marker is carried out to eliminate possible deviations that can be caused by wheel slippage by using an optical sensor during any additional time.

The route-planning and synchronization for multiple platforms is based on the approach that was proposed in Mazur (2013). All of the selected zones of the marked surface are divided into two groups: zones of intersections, and zones of buffers. In the zones of intersections, it is possible to change the directions of the platform movements by 90 degrees. Loading containers in buffers B or terminals T from the mobile platform is carried out by the manipulator when it is in the center of one of the zones of buffers. The centers of all of the zones are marked with markers that are recognized by an optical sensor. Each zone is determined by indices Z (i,j) (i is the row number, and j is the column number).

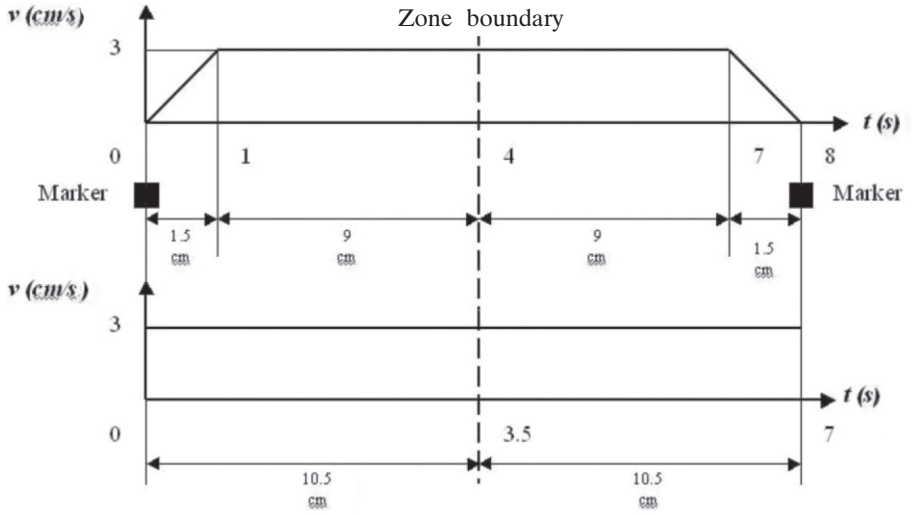

Fig. 5. Changing speed of mobile platform between markers

Depending on the location of the starting and ending points, the following options are possible for routing (Fig. 6):

- If the initial and final points are in adjacent zones Z (1, 1) and Z (1, 2) (Variant a), then the relocation is carried out in 8 s in accordance with Figure 5.
- If initial point Z (5, 2) and final point Z (5, 4) are on the same line horizontally (Variant b) or vertically, the relocation is carried out in $k \times 7 + 8$ s (k is the number of transit zones that the platform crosses at the rated speed without stopping).
- If initial point Z (3, 2) is on a horizontal line and final point Z (2, 1) is on a vertical line, then the direction of the platform movement is changed by 90 degrees within 1 s in zone of their intersection Z (3, 1) (Variant c).
- If initial point Z (4, 3) is on a vertical line and final point Z (1, 4) is on a horizontal line, then the direction of the movement is changed by 90 degrees (also within 1 s) in zone of their intersection Z (1, 3) (Variant d).
- If one of the coordinates of the zones of initial point Z (5, 6) and final point Z (1, 6) of the route are the same, then we have two equivalent routes with two zones of the direction change at the intersections: for Variant e, there are zones Z (5, 5) and Z (1, 5); for Variant f, there are zones Z (5, 7) and Z (1, 7). The choice of one of these two routes is made according to additional criteria.
- If the coordinates of initial point Z (5, 2) and final point Z (1, 6) are different (Fig. 7), there may be several routes that are identical in length (Variants a and b) that connect these points with the two zones of the direction change. The choice of one of them is made by taking possible collisions with other routes into account (for example, Route c).Thus, Route a is chosen, which in a zone of intersections that does not intersect with other previously laid routes in general (or during an intersection crossing).

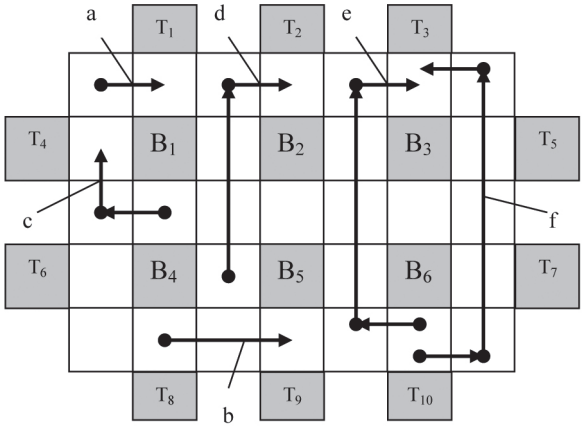

Fig. 6. Typical variants of orthogonal routes

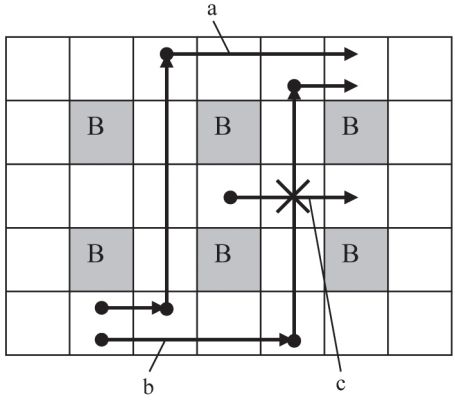

Fig. 7. Several orthogonal routes between specified points

Increasing the number of mobile platforms can increase the performance of the transport system, which is determined by the number of containers that are moved in a given amount of time. However, the probability of collisions increases with an excessive number of platforms; this can lead to additional delays and declining productivity.

Centralized planning is performed on the central computer of the transport system. At the same time, mobile platforms move according to the schedules that are received from a central computer (which provides traffic planning without collisions). For the centralized planning and synchronization of the joint movements of several platforms, a matrix model is proposed that ensures the elimination of collisions due to additional controlled delays.

When planning a movement, matrix M (i, j, m) is formed in which the model time of the beginning and end of platform [m/s] location in zone Z(i, j) are fixed. The time of the

platform location in zone Z (i, j) is determined on the basis of the real time of platform move beginning *ts*, acceleration time *ta*, time of movement with nominal speed *tv*, deceleration time *td* (see Fig. 5), time of platform turn at the intersection *tm* ($tm = 1$), time of the container loading/unloading *tc*, and adjustment time *tu* (alignment of the platform center with the center of the marker). Additional delay time *tz* is introduced to eliminate collisions based on an analysis of the matrix. The elimination of collisions due to the introduction of additional delays *tz* ($tz = 14.5$) is shown in Figure 8.

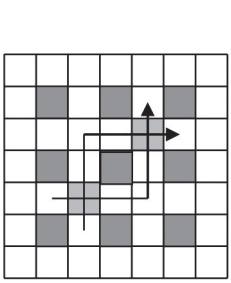

				37.5/45		
				30.5/45		
				23/37.5		
	0/7.5	**0/14.5**	7.5/22	14.5/30.5		

MP1

		14.5/30.5	23/37.5	**30.5/45**	37.5/45	
		7.5/22				
		0/14.5				
		0/7.5				

MP2

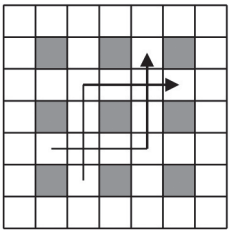

				37.5/45		
				30.5/45		
				23/37.5		
	0/7.5	**0/14.5**	7.5/22	14.5/30.5		

MP1

		29/45	37.5/52	**45/59.5**	52/59.5	
		22/36.5				
		14.5/29				
		0/14.5				

MP2

Fig. 8. Matrix model for collision elimination

4. Conclusions

The following new scientific and practical results were obtained in this work:

- A method for providing necessary positioning accuracy based on the movements of a mobile platform with variable speeds has been proposed.
- A control system for the manipulator to move containers has been developed.
- A matrix model for eliminating conflicts during the joint movements of several mobile platforms on a marked surface has been developed.

REFERENCES

Mazur V.V., 2013, *Synchronization of city bus routes*, 12th International Conference on the Experience of Designing and Application of CAD Systems in Microelectronics (CADSM 2013), Lviv.

Mazur V.V., 2021, *Robotic mobile platform for container transportation*, 16th International Conference on Experience of Designing and Application of CAD System (CADSM 2021), 10–13. DOI: https://doi.org/10.1109/CADSM52681.2021.9385212.

Mazur V.V., Panchak S.T., 2021, *Experimental model of a mobile platform for moving on orthogonal routes*, IOP Conference Series: Materials Science and Engineering, 1016, 012011. DOI: https://doi.org/10.1088/1757-899X/1016/1/012011.

Shneier M., Bostelman R., 2015, *Literature review of mobile robots for manufacturing*, NISTIR 8022, National Institute of Standards and Technology, U.S. Department of Commerce. DOI: http://dx.doi.org/10.6028/NIST.IR.8022.

Determination of thermal-stressed state of inhomogeneous orthotropic cylindrical shell under thermal heating

Roman Musii ORCID ID: 0000-0002-7169-2206

Lviv Polytechnic National University
Institute of Applied Mathematics and Fundamental Sciences
Department of Mathematics, Lviv
email: roman.s.musii@lpnu.ua

Nataliia Melnyk ORCID ID: 0000-0003-2337-2395

Lviv Polytechnic National University
Institute of Computer Science and Information Technologies
Department of Software, Lviv
email: nataliia.b.melnyk@lpnu.ua

Uliana Zhydyk ORCID ID: 0000-0002-1104-1946

Lviv Polytechnic National University
Institute of Applied Mathematics and Fundamental Sciences
Department of Mathematics, Lviv
email: uliana.v.zhydyk@lpnu.ua

Mykhaylo Melnyk ORCID ID: 0000-0002-8593-8799

Lviv Polytechnic National University
Institute of Computer Science and Information Technologies
Department of Computer-Aided Design Systems, Lviv
email: mykhaylo.r.melnyk@lpnu.ua

Oksana Oryshchyn ORCID ID: 0000-0002-8965-1891

Lviv Polytechnic National University
Institute of Applied Mathematics and Fundamental Sciences
Department of Mathematics, Lviv
email: oksana.h.oryshchyn@lpnu.ua

Krzysztof Pytel ORCID ID: 0000-0002-1924-8351

AGH University of Science and Technology
Faculty of Mechanical Engineering and Robotics
Department of Power Systems and Environmental Protection Facilities, Krakow
email: kpytel@agh.edu.pl

ABSTRACT

Systems of initial equations of the nonstationary problem of heat conductivity and the quasistatic problem of thermoelasticity for an inhomogeneous orthotropic cylindrical shell under its thermal heating by the external environment are recorded. Using double finite integral Fourier transforms in spatial coordinates and the Laplace transform over time, we obtained general solutions to the formulated thermoelasticity problems for a given finite hinged supported at the shell edges.

Keywords: thermal conductivity, thermoelasticity, cylindrical orthotropic shell, thermal heating

1. Introduction

Inhomogeneous cylindrical shells (in particular, those of layered structures) are widely used in many fields of modern technology (including aerospace construction) to increase the strength and rigidity of structures as well as protect them from low- or high-temperature heat. Therefore, the calculation of the thermal stress state of such structures is an important engineering task.

The elements of constructions of a layered structure have been considered in many works; particularly, in Reddy (2004) and Hetnarski (2014). Refined models that take the characteristics of composite materials into account (high anisotropy in the transverse direction in particular) were developed in Punera et al. (2018). Using the equation of interconnected thermoelasticity, the influence of the coefficient of cohesion on the dynamic behavior of composite shells was analyzed (Brischetto, Carrera 2010). The purpose of this section is to write down the systems of the initial equations of the nonstationary heat conductivity problem and the quasi-static thermoelasticity problem for inhomogeneous orthotropic cylindrical shells and to develop a method for constructing their general solutions under thermal heating by the external environment.

2. Formulation of problem and system of initial equations

Consider an inhomogeneous orthotropic circular cylindrical shell with a thickness of $2h$ and a finite length of l. The points of space of the shell are assigned to cylindrical coordinate system x, θ, z (which denotes the axial, circular, and radial coordinates, respectively). The origin is in the middle surface of the radius R shell. In the future, these coordinates will correspond to indices 1, 2, 3.

The shell is affected by external forces, and it can be heated by internal heat sources and the external environment. To study the thermoelastic behavior of such a shell, we use a mathematical model with six degrees of freedom. This model is based on

assumptions about the linear distribution of displacement vector $U_i(x, \theta, z, \tau)$ ($i = 1, 2, 3$) and temperature $t(x, \theta, z, \tau)$ over the thickness of the shell.

$$U_i(x,\theta,z,\tau) = u_i(x,\theta,\tau) + z\gamma_i(x,\theta,\tau) \tag{1}$$

$$t(x,\theta,z,\tau) = T_1(x,\theta,\tau) + \frac{z}{h}T_2(x,\theta,\tau) \tag{2}$$

Here, u_i are the components of the displacement vector of the points of the middle surface, γ_i are the components of the vector of normal rotation angles, and T_n are integral characteristics of temperature:

$$T_n = \frac{2n-1}{2h^n}\int_{-h}^{h} t\, z^{n-1}\, dz, (n = 1, 2) \tag{3}$$

In the general case, this model of thermoelasticity of the considered shell consists of interconnected systems of equations of heat conductivity and thermoelasticity. If we neglect the effect of deformation on the change in the temperature field, these systems will be independent. Consider these systems in stages.

3. System of equations of nonstationary heat conductivity for inhomogeneous anisotropic shells

Let a thin shell of a constant thickness of $2h$ exchange heat with the environment according to Newton's law (or be heated by internal heat sources). The shell material is inhomogeneous in thickness and anisotropic (with one plane of heat symmetry). Its orthotropy axes coincide with the coordinate axes. The temperature field $t(\alpha, \beta, z, \tau)$ in such a shell is described by a three-dimensional heat-conduction equation, which takes the following form in a curvilinear orthogonal coordinate system α, β, z according to the accuracy of the theory of thin shells:

$$\Delta t + \frac{\partial}{\partial z}\left(\lambda_{33}(z)\frac{\partial t}{\partial z}\right) + 2k_0\lambda_{33}(z)\frac{\partial t}{\partial z} - c_e(z)\frac{\partial t}{\partial \tau} + w_t = 0 \tag{4}$$

where:

w_t – density of heat sources,
$c_e(z)$ – specific heat capacity,
$\lambda_{ij}(z)$ – coefficients of heat conductivity,
τ – time,
A, B – corresponding Lamé coefficients,
k_0 – average curvature of shell, a dimensionless quantity.

Here $\Delta = \frac{1}{AB}\left[\lambda_{11}(z)\frac{\partial}{\partial\alpha}\left(\frac{B}{A}\frac{\partial}{\partial\alpha}\right)+\lambda_{22}(z)\frac{\partial}{\partial\beta}\left(\frac{A}{B}\frac{\partial}{\partial\beta}\right)+2\lambda_{12}(z)\frac{\partial^2}{\partial\alpha\partial\beta}\right]$ – the Laplace operator in a curvilinear orthogonal coordinate system α, β, *z*.

To make the solution of Equation (1) unambiguous, we use initial condition $t\big|_{\tau=0} = t_0(\alpha,\beta)$. Here, $t_0(\alpha, \beta)$ is a function that describes the initial temperature distribution in the shell. As boundary conditions, we use one of the $t = t^{\pm}$, $\lambda_{33}(\partial t/\partial z) = \mp q^{\pm}$, $\lambda_{33}(\partial t/\partial z) \pm \alpha_z^{\pm}\left(t - t^{\pm}_z\right) = 0$ conditions on the $z = \pm h$ surfaces of the shell. Here, $\alpha_z^{\pm}$ are the coefficients of the heat transfer from the $z = \pm h$ surfaces, and $t^{\pm}$, $q^{\pm}$, $t^{\pm}_z$ are the temperature, heat flux, and temperature of the environment, respectively, that are set on these surfaces. If the shell is not closed, then similar conditions must be set at its edges. To formulate a two-dimensional problem on the integral characteristics of temperature, it is necessary to set the temperature distribution law over the shell thickness with the further use of the method of averaging for the original Equation (4) according to Formula (3).

For the cubic temperature distribution over the shell thickness for its integral characteristics T_1 and T_2 we obtain the following system of equations:

$$\begin{aligned}
&\Delta_{(1)}T_1 + \Delta_{(6)}T_2 + \frac{5k_0}{2h}\left(\Lambda_{33}^{(1)} - \Lambda_{33}^{(3)}\right)T_2 - C^{(1)}\dot{T}_1 - \frac{5}{12}\left(3C^{(2)} - C^{(4)}\right)\dot{T}_2 + W_t^{(1)} = f_1,\\
&\Delta_{(2)}T_1 + \Delta_{(7)}T_2 + \frac{5k_0}{2h}\left(\Lambda_{33}^{(2)} - \Lambda_{33}^{(4)}\right)T_2 - \frac{5}{4h^2}\left(\Lambda_{33}^{(1)} - \Lambda_{33}^{(3)}\right)T_2 -\\
&\quad - C^{(2)}\dot{T}_1 - \frac{5}{12}\left(3C^{(3)} - C^{(5)}\right)\dot{T}_2 + W_t^{(2)} = f_2
\end{aligned} \tag{5}$$

Accordingly, the system of equations takes the following form for a linear temperature distribution for its integral characteristics T_1 and T_2:

$$\begin{aligned}
&\Delta_{(1)}T_1 + \Delta_{(2)}T_2 + \frac{2k_0}{h}\Lambda_{33}^{(1)}T_2 - C^{(1)}\dot{T}_1 - C^{(2)}\dot{T}_2 + W_t^{(1)} = F_1,\\
&\Delta_{(2)}T_1 + \Delta_{(3)}T_2 + \frac{2k_0}{h}\Lambda_{33}^{(2)}T_2 - \frac{1}{h^2}\Lambda_{33}^{(1)}T_2 - C^{(2)}\dot{T}_1 - C^{(3)}\dot{T}_2 + W_t^{(2)} = F_2
\end{aligned} \tag{6}$$

Here

$$\left\{\Lambda_{ij}^{(n)}, \Lambda_{33}^{(n)}, C^{(n)}\right\} = \int_{-h}^{h} \left\{\lambda_{ij}(z), \lambda_{33}(z), c_e(z)\right\} \left(\frac{z}{h}\right)^{n-1} dz, (n = 1, 2, ..., 5),$$

$$\Delta_{(k)} = \frac{1}{AB}\left[\Lambda_{11}^{(k)} \frac{\partial}{\partial\alpha}\left(\frac{B}{A}\frac{\partial}{\partial\alpha}\right) + \Lambda_{22}^{(k)} \frac{\partial}{\partial\beta}\left(\frac{A}{B}\frac{\partial}{\partial\beta}\right) + 2\Lambda_{12}^{(k)} \frac{\partial^2}{\partial\alpha\partial\beta}\right], (k = 1, 2, ..., 7), \quad (7)$$

$$\Lambda_{ij}^{(6)} = \frac{5}{12}\left(3\Lambda_{ij}^{(2)} - \Lambda_{ij}^{(4)}\right); \; \Lambda_{ij}^{(7)} = \frac{5}{12}\left(3\Lambda_{ij}^{(3)} - \Lambda_{ij}^{(5)}\right); \; W_i^t = \int_{-h}^{h} w_t \left(\frac{z}{h}\right)^{j-1} dz; \; \dot{T}_i = \frac{\partial T_i}{\partial\tau}$$

where: $F(\alpha, \beta, \tau)_1$, $F_2(\alpha, \beta, \tau)$, $f_1(\alpha, \beta, \tau)$, $f_2(\alpha, \beta, \tau)$ are functions that depend on boundary conditions on $z = \pm h$ surfaces of shell.

Note that Equations (5) that correspond to the cubic law of temperature distribution are obtained under the condition that the boundary conditions on the $z = \pm h$ surfaces are satisfied and have the same order as in Equation (6). To determine the integral $\Lambda_{ij}^{(n)}$, $\Lambda_{33}^{(n)}$, $C^{(n)}$ characteristics of the thermophysical properties of an inhomogeneous material using Formula (7), it is necessary to specify the distribution law of these properties over the thickness.

In a cylindrical x, θ, z coordinate system, the heat conduction Equations (6) take the following form with respect to the integral characteristics of the temperature in the absence of heat sources:

$$\begin{aligned}
&\left(\Delta_{(1)} - \varepsilon_1^t\right)T_1 + \left(\Delta_{(2)} + \frac{\Lambda_{33}^{(1)}}{hR} - \varepsilon_2^t\right)T_2 - C^{(1)}\dot{T}_1 = -F_1^z, \\
&\left(\Delta_{(2)} - \varepsilon_2^t\right)T_1 + \left(\Delta_{(3)} - \frac{\Lambda_{33}^{(1)}}{h^2} - \varepsilon_1^t\right)T_2 - C^{(3)}\dot{T}_2 = -F_2^z
\end{aligned} \quad (8)$$

Here, $\Delta_{(k)} = \Lambda_{11}^{(k)} \frac{\partial^2}{\partial x^2} + \frac{\Lambda_{22}^{(k)}}{R^2} \frac{\partial^2}{\partial\theta^2}$, $(k = 1, 2, 3)$; $F_1^z = \varepsilon_1^t t_1^z + \varepsilon_2^t t_2^z + W_1^t$;

$F_2^z = \varepsilon_2^t t_1^z + \varepsilon_1^t t_2^z + W_2^t$.

To unambiguously solve the system of Equations (8), let us set the following boundary conditions for the integral T_1 and T_2 characteristics at the $x = 0$ and $x = l$ edges of the shell:

$$T_1 = T_2 = 0 \quad (9)$$

as well as the initial conditions at the $\tau = 0$ moment of time:

$$T_1(x,\theta,0) = T_1^0(x,\theta),\ T_2(x,\theta,0) = T_2^0(x,\theta) \tag{10}$$

4. Technique for solving problem of heat conductivity

After applying the double finite integral Fourier transform in the x, θ coordinates according to the specified boundary conditions in Equation (9), the system of Equations (8) will take the following form:

$$\frac{dT_{1mn}}{d\tau_1} + g_1 T_{1mn} + g_2 T_{2mn} = F^z_{1mn}, \frac{dT_{2mn}}{d\tau_1} + g_3 T_{1mn} + g_4 T_{2mn} = F^z_{2mn} \tag{11}$$

Here, $g_1 = L^{(1)}_{11}\mu_n^2 + L^{(1)}_{22}\delta^2 m^2 + Bi_1;\ g_2 = L^{(2)}_{11}\mu_n^2 + L^{(2)}_{22}\delta^2 m^2 - \delta + Bi_2;\ \mu_n = \frac{\pi n h}{l};$

$$\delta = \frac{h}{R};\ g_3 = \tilde{C}\left(L^{(2)}_{11}\mu_n^2 + L^{(2)}_{22}\delta^2 m^2 + Bi_2\right);\ g_4 = \tilde{C}\left(L^{(3)}_{11}\mu_n^2 + L^{(3)}_{22}\delta^2 m^2 + Bi_1 + 1\right);$$

$$\tau_1 = \frac{\Lambda^{(1)}_{33}}{h^2 C^{(1)}}\tau;\ \tilde{C} = \frac{C^{(1)}}{C^{(3)}};\ L^{(j)}_{ii} = \frac{\Lambda^{(j)}_{ii}}{\Lambda^{(1)}_{33}};\ Bi_i = \frac{\varepsilon^t_i h^2}{\Lambda^{(1)}_{33}};$$

$$F^z_{1mn} = Bi_1 t^z_{1mn} + Bi_2 t^z_{2mn} + W^t_{1mn}\frac{h^2}{\Lambda^{(1)}_{33}};\ F^z_{2mn} = \left(Bi_2 t^z_{1mn} + Bi_1 t^z_{2mn} + W^t_{2mn}\frac{h^2}{\Lambda^{(1)}_{33}}\right)\tilde{C}.$$

The solution of the system of Equations (11) under the initial conditions in Equations (10) using the time τ integral Laplace transform will be written as follows:

$$T_1 = \sum_{n=1}^{\infty}\sum_{m=0}^{\infty}\sum_{\substack{j=1\\k\neq j}}^{2}\frac{\sin\frac{\pi n x}{l}\cos m\theta}{p_j - p_k}\Big\{\left(p_j - g_4\right)Q_{1nm}Z_1^{(j)}(\tau) + g_2 Q_{2nm}Z_2^{(j)}(\tau) +$$

$$+\left[\left(p_j - g_4\right)T^0_{1nm} + g_2 T^0_{2nm}\right]\exp(-p_j\tau_1)\Big\},$$

$$T_2 = \sum_{n=1}^{\infty}\sum_{m=0}^{\infty}\sum_{\substack{j=1\\k\neq j}}^{2}\frac{\sin\frac{\pi n x}{l}\cos m\theta}{p_j - p_k}\Big\{\left(p_j - g_1\right)Q_{2nm}Z_2^{(j)}(\tau) + g_3 Q_{1nm}Z_1^{(j)}(\tau) + \tag{12}$$

$$+\left[\left(p_j - g_1\right)T^0_{2nm} + g_3 T^0_{1nm}\right]\exp(-p_j\tau_1)\Big\}$$

Here

$$\left\{Q_{inm}, T^0_{inm}\right\} = \frac{\varsigma}{\pi l}\int_0^l\int_{-\pi}^{\pi}\left\{Q_i, T_i^0\right\}(x,\theta)\sin\frac{\pi n}{l}x\cos m\theta\, dx\, d\theta,\ \varsigma = \begin{cases}1, & m=0\\ 2, & m\neq 0\end{cases} \tag{13}$$

$$p_j = \frac{g_1+g_4}{2} + (-1)^j\sqrt{\frac{(g_1-g_4)^2}{4}+g_2g_3}\,Z_i^{(j)} = \int_0^{\tau_1}\tilde{F}_i(u)\exp\left(-p_j(\tau_1-u)\right)du, \tag{14}$$

$(i,\ j=1,\ 2)$

Taking Equations (13) and (14) into account, we obtain a general solution of the heat conductivity problem by substituting the expressions in Formula (12) into the linear law of temperature distribution over the entire thickness of the considered shell. Note that, using the same technique for the system of Equations (5), we wrote down the general solution of the heat conductivity problem for a given shell and in the case of a cubic law of temperature distribution over its thickness.

5. System of equations of thermoelasticity

The kinematic relationships for the e_{ij} deformation components of an arbitrary point of the shell are as follows:

$$\begin{gathered}e_{11} = \varepsilon_{11} + z\text{æ}_{11},\ e_{22} = \frac{\varepsilon_{22}+z\text{æ}_{22}}{1+\frac{z}{R}},\ e_{33} = \varepsilon_{33},\\ e_{12} = \frac{\varepsilon_{12}+z\text{æ}_{12}+z^2\omega_{12}}{1+\frac{z}{R}},\ e_{13} = \varepsilon_{13}+z\text{æ}_{13},\ e_{23} = \frac{\varepsilon_{23}+z\text{æ}_{23}}{1+\frac{z}{R}}\end{gathered} \tag{15}$$

Here, the components of the deformation of the e_{ij}, æ_{ij} middle surface in terms of generalized displacements u_i, γ_i are described by the following formulas:

$$\begin{gathered}\varepsilon_{11} = \partial_1 u_1,\ \varepsilon_{22} = \frac{1}{R}(u_3+\partial_2 u_2),\ \varepsilon_{33} = \gamma_3,\ \varepsilon_{12} = \frac{1}{R}\partial_2 u_1 + \partial_1 u_2,\\ \varepsilon_{23} = \gamma_2 + \frac{1}{R}(\partial_2 u_3 - u_2),\ \varepsilon_{13} = \gamma_1 + \partial_1 u_3,\ \omega_{12} = \frac{1}{R}\partial_1\gamma_2,\ \text{æ}_{11} = \partial_1\gamma_1,\\ \text{æ}_{22} = \frac{1}{R}(\gamma_3+\partial_2\gamma_2),\ \text{æ}_{13} = \partial_1\gamma_3,\ \text{æ}_{12} = \partial_1\gamma_2 + \frac{1}{R}(\partial_2\gamma_1+\partial_1 u_2),\ \text{æ}_{23} = \frac{1}{R}\partial_2\gamma_3\end{gathered} \tag{16}$$

The physical equations for the stresses and strains take the following form:

$$\begin{pmatrix}\sigma_{11}\\ \sigma_{22}\\ \sigma_{33}\\ \sigma_{12}\end{pmatrix}=\begin{pmatrix}c_{11} & c_{12} & c_{13} & \\ c_{12} & c_{22} & c_{23} & \\ c_{13} & c_{23} & c_{33} & \\ & & & c_{66}\end{pmatrix}\begin{pmatrix}e_{11}\\ e_{22}\\ e_{33}\\ e_{12}\end{pmatrix}-\begin{pmatrix}\beta_{11}^{t}\\ \beta_{22}^{t}\\ \beta_{33}^{t}\\ \end{pmatrix}t,\ \begin{pmatrix}\sigma_{13}\\ \sigma_{23}\end{pmatrix}=\begin{pmatrix}c_{44} & \\ & c_{55}\end{pmatrix}\begin{pmatrix}e_{13}\\ e_{23}\end{pmatrix} \tag{17}$$

where:

$c_{ij}(z)$ – coefficients of elasticity,

$\beta_{ii}^{t}(z)=c_{i1}\alpha_{11}^{t}+c_{i2}\alpha_{22}^{t}+c_{i3}\alpha_{33}^{t}$ – coefficients of thermoelasticity,

$\alpha_{ij}^{t}(z)$ – coefficients of thermal linear expansion.

The physical equations for internal efforts N_{ij} and moments M_{ij} are obtained from the following relationships:

$$\begin{aligned}
\{N_{11},N_{12},N_{13}\}&=\int_{-h}^{h}\{\sigma_{11},\sigma_{12},\sigma_{13}\}\left(1+\frac{z}{R}\right)dz,\\
\{N_{22},N_{21},N_{23}\}&=\int_{-h}^{h}\{\sigma_{22},\sigma_{12},\sigma_{23}\}\,dz,\\
\{M_{11},M_{12},M_{13}\}&=\int_{-h}^{h}\{\sigma_{11},\sigma_{12},\sigma_{13}\}\left(1+\frac{z}{R}\right)z\,dz,\\
\{M_{22},M_{21},M_{23}\}&=\int_{-h}^{h}\{\sigma_{22},\sigma_{12},\sigma_{23}\}\,z\,dz,\ N_{33}=\int_{-h}^{h}\sigma_{33}\left(1+\frac{z}{R}\right)dz
\end{aligned} \tag{18}$$

The equilibrium equations will be as follows:

$$\begin{aligned}
&\partial_1 N_{11}+\frac{1}{R}\partial_2 N_{21}=-q_1,\ \partial_1 N_{12}+\frac{1}{R}(\partial_2 N_{22}+N_{23})-q_2,\\
&\partial_1 N_{13}+\frac{1}{R}(\partial_2 N_{23}-N_{22})=-q_3,\\
&\partial_1 M_{11}+\frac{1}{R}\partial_2 M_{21}-N_{13}=-m_1,\ \partial_1 M_{12}+\frac{1}{R}\partial_2 M_{22}-N_{23}=-m_2,\\
&\partial_1 M_{13}+\frac{1}{R}(\partial_2 M_{23}-M_{22})-N_{33}=-m_3
\end{aligned} \tag{19}$$

Here, q_i, m_i are the components of the $\partial_1 = \partial/\partial x$ and $\partial_2 = \partial/\partial\theta$ surface loads. Using the above relationships, we write down a system of equilibrium Equations (19) in generalized displacements:

$$\sum_{k}^{6} L_{rk} y_k = b_r \quad (r,k = 1,2,...,6) \tag{20}$$

Here, $y_i = u_i$; $y_{3+i} = \gamma_i$ (i = 1, 2, 3)are generalized movements. Differential operators L_{rk} ($L_{rk} = L_{kr}$)and members b_r in system of Equations (20) take the following form:

$$L_{11} = A_{11}\partial_{11}^2 + \frac{A_{66}}{R^2}\partial_{22}^2,\ L_{12} = \frac{A_{12} + A_{66}}{R}\partial_{12}^2,\ L_{13} = \frac{A_{12}}{R}\partial_1,\ L_{14} = B_{11}\partial_{11}^2 + \frac{B_{66}}{R^2}\partial_{22}^2,$$

$$L_{15} = \frac{B_{12} + B_{66}}{R}\partial_{12}^2,\ L_{16} = \left(A_{13} + \frac{B_{12}}{R}\right)\partial_1,\ L_{22} = A_{66}\partial_{11}^2 + \frac{1}{R^2}\left(A_{22}\partial_{22}^2 - k'A_{55}\right),$$

$$L_{23} = \frac{A_{22} + k'A_{55}}{R^2}\partial_2,\ L_{24} = \frac{B_{12} + B_{66}}{R}\partial_{12}^2,\ L_{25} = B_{66}\partial_{11}^2 + \frac{B_{22}}{R^2}\partial_{22}^2 + \frac{k'A_{55}}{R},$$

$$L_{26} = \left(\frac{A_{23}}{R} + \frac{B_{22} + k'B_{55}}{R^2}\right)\partial_2,\ L_{33} = -k'A_{44}\partial_{11}^2 - \frac{k'A_{55}}{R^2}\left(k'A_{55}\partial_{22}^2 + A_{22}\right),$$

$$L_{34} = \left(\frac{B_{12}}{R} - k'A_{44}\right)\partial_1,\ L_{35} = \frac{1}{R}\left(\frac{B_{22}}{R} - k'A_{55}\right)\partial_2,$$

$$L_{36} = -k'B_{44}\partial_{11}^2 + \frac{1}{R^2}\left(B_{22} - k'B_{55}\partial_{22}^2\right) + \frac{A_{23}}{R},$$

$$L_{44} = D_{11}\partial_{11}^2 + \frac{D_{66}}{R^2}\partial_{22}^2 - k'A_{44},\ L_{45} = \frac{D_{12} + D_{66}}{R}\partial_{12}^2,\ L_{46} = \left(\frac{D_{12}}{R} + B_{13} - k'B_{44}\right)\partial_1,$$

$$L_{55} = D_{66}\partial_{11}^2 + \frac{D_{22}}{R^2}\partial_{22}^2 - k'A_{55},\ L_{56} = \frac{1}{R}\left(B_{23} - k'B_{55} + \frac{D_{22}}{R}\right)\partial_2,$$

$$L_{66} = A_{33} + \frac{2B_{23}}{R} + \frac{1}{R^2}\left(D_{22} - k'D_{55}\partial_{22}^2\right) - k'D_{44}\partial_{11}^2,\ b_1 = A_{11}^t\partial_1 T_1 + \frac{B_{11}^t}{h}\partial_1 T_2 - q_1,$$

$$b_2 = \frac{A_{22}^t}{R}\partial_2 T_1 + \frac{B_{22}^t}{Rh}\partial_2 T_2 - q_2,\ b_3 = \frac{A_{22}^t}{R}T_1 + \frac{B_{22}^t}{Rh}T_2 + q_3,$$

$$b_4 = B_{11}^t\partial_1 T_1 + \frac{D_{11}^t}{h}\partial_1 T_2 - m_1,\ b_5 = \frac{B_{22}}{R}\partial_2 T_1 + \frac{D_{22}^t}{Rh}\partial_2 T_2 - m_2.$$

Here, $\left\{A_{ii}, B_{ij}, D_{ij}\right\} = \int\limits_{-h}^{h} c_{ij}\left\{1, z, z^2\right\}dz, \left\{A_{ii}^t, B_{ii}^t, D_{ii}^t\right\} = \int\limits_{-h}^{h} \beta_{ii}^t\left\{1, z, z^2\right\}dz$ (k'– shear coefficient).

For the solution of system of Equations (20) to be unambiguous, it is necessary to set the appropriate boundary conditions. In the case of a cylindrical shell of a finite length, one value from each of the following pairs are set at its and ends:

$$\{N_{11}, u_1\};\ \{N_{12}, u_2\};\ \{N_{13}, u_3\};\ \{M_{11}, \gamma_1\};\ \{M_{12}, \gamma_2\};\ \{M_{13}, \gamma_3\}.$$

The system of Equations (20) together with the boundary conditions form the boundary value problem of quasi-static thermoelasticity for inhomogeneous anisotropic cylindrical shells in displacements. According to the known displacements from the relationships in Formula (16), we determine the deformations of the mean surface and the forces and moments according to the equations is:

$$\begin{pmatrix} N_{11} \\ N_{22} \\ N_{33} \\ M_{11} \\ M_{22} \end{pmatrix} = \begin{pmatrix} A_{11} & A_{12} & A_{13} & B_{11} & B_{12} \\ A_{12} & A_{22} & A_{23} & B_{12} & B_{22} \\ A_{13} & A_{23} & A_{33} & B_{13} & B_{23} \\ B_{11} & B_{12} & B_{13} & D_{11} & D_{12} \\ B_{12} & B_{22} & B_{23} & D_{12} & D_{22} \end{pmatrix} \begin{pmatrix} \partial_1 u_1 \\ (\partial_2 u_2 + u_3)/R \\ \gamma_3 \\ \partial_1 \gamma_1 \\ (\partial_2 \gamma_2 + \gamma_3)/R \end{pmatrix} - \begin{pmatrix} A_{11}^t \\ A_{22}^t \\ A_{33}^t \\ B_{11}^t \\ B_{22}^t \end{pmatrix} T_1 - \begin{pmatrix} B_{11}^t \\ B_{22}^t \\ B_{33}^t \\ D_{11}^t \\ D_{22}^t \end{pmatrix} T_2/h, \tag{21}$$

$$\begin{pmatrix} N_{12} \\ M_{12} \end{pmatrix} = \begin{pmatrix} A_{66} & B_{66} \\ B_{66} & D_{66} \end{pmatrix} \begin{pmatrix} \partial_1 u_2 + \partial_2 u_1/R \\ \partial_1 \gamma_2 + \partial_2 \gamma_1/R \end{pmatrix}, \begin{pmatrix} N_{13} \\ M_{13} \end{pmatrix} = k' \begin{pmatrix} A_{44} & B_{44} \\ B_{44} & D_{44} \end{pmatrix} \begin{pmatrix} \gamma_1 + \partial_1 u_3 \\ \partial_1 \gamma_3 \end{pmatrix},$$

$$\begin{pmatrix} N_{23} \\ M_{23} \end{pmatrix} = k' \begin{pmatrix} A_{55} & B_{55} \\ B_{55} & D_{55} \end{pmatrix} \begin{pmatrix} \gamma_2 + (\partial_2 u_3 - u_2)/R \\ \partial_2 \gamma_3/R \end{pmatrix}$$

According to the obtained forces and moments, Formulas (15) and (17), we write down the temperature stresses and strains in the cylindrical shell.

6. Methods for solving thermoelasticity problem

Consider a cylindrical shell that is antisymmetric relative to the middle surface and composed of an even number of orthotropic layers with the same thickness and properties – the material axes of which are oriented at angles of 0° or 90° to the axis of the shell. Let the $x = 0$ and $x = l$ edges of the shells be hinged, and a temperature of 0°C is set on them.

Then, we would have the following boundary conditions:

$$u_3 = u_2 = 0;\ \gamma_3 = \gamma_2 = 0;\ N_{11} = M_{11} = 0 \tag{22}$$

$$T_1 = T_2 = 0 \tag{23}$$

At the initial moment, the temperature characteristics are set by the coordinate functions:

$$T_1(x,\theta,0) = T_1^0(x,\theta),\ T_2(x,\theta,0) = T_2^0(x,\theta) \tag{24}$$

The solution of the system of equilibrium Equations (20) that satisfies the boundary conditions in (22) for the known integral characteristics of temperatures T_1 and T_2 is obtained by means of finite integral Fourier transforms in the x, θ coordinates. As a result, we obtain a system of algebraic equations to determine the Fourier coefficients of the y_{kmn} required functions. We write this system of equations in matrix form:

$$\mathbf{AY} = \mathbf{S}T_{1mn} + \mathbf{G}T_{2mn} \tag{25}$$

where: corresponding matrices will be $\mathbf{A} = (a_{rk})_{6\times6}$, $\mathbf{Y} = (y_{kmn})_{6\times1}$, $\mathbf{S} = (s_k)_{6\times1}$, $\mathbf{G} = (g_k)_{6\times1}$.

Here, $y_{imn} = U_{imn}$ are the Fourier coefficients for displacements u_i, and $y_{3+i,mn} = \Gamma_{imn}$ are the Fourier coefficients for displacements γ_i (i = 1, 2, 3). The coefficients of the a_{rk}, s_k and g_k matrices are calculated using finite integral Fourier transforms in spatial coordinates to the expressions of the differential operators of the system of Equations (20).

After the transformations, we obtain the solution of system of Equations (25) in the following form:

$$y_{kmn} = \frac{1}{|A|}\sum_{r=1}^{6}(s_r T_{1mn} + g_r T_{2mn})B_{rk},\ (k = 1, 2, ..., 6)$$

Here, $|A|$ is the determinant of matrix **A**, and is an algebraic addition to the element a_{rk} of this matrix. The generalized displacements are written by the following expressions in terms of the corresponding Fourier coefficients:

$$\{u_1, \gamma_1\} = \sum_{n=0}^{\infty}\sum_{m=0}^{\infty}\{U_{1mn}, \Gamma_{1mn}\}\cos\frac{\pi n}{l}x\cos m\theta,$$

$$\{u_2, \gamma_2\} = \sum_{n=1}^{\infty}\sum_{m=1}^{\infty}\{U_{2mn}, \Gamma_{2mn}\}\sin\frac{\pi n}{l}x\sin m\theta, \tag{26}$$

$$\{u_3, \gamma_3\} = \sum_{n=1}^{\infty}\sum_{m=0}^{\infty}\{U_{3mn}, \Gamma_{3mn}\}\sin\frac{\pi n}{l}x\cos m\theta$$

According to the known generalized displacements (26) and the temperature field, all of the other characteristics of the stress and strain state of the shell are determined by Formulas (15)–(17) and (21).

REFERENCES

Brischetto S., Carrera E., 2010, *Coupled thermo-mechanical analysis of one-layered and multilayered isotropic and composite shells*, Computer Modeling in Engineering and Sciences, 56(3), 249–301.

Hetnarski R.B. (Ed.), 2014, *Encyclopedia of Thermal Stresses*, Springer.

Punera D., Kant T., Desai Y., 2018, *Thermoelastic analysis of laminated and functionally graded sandwich cylindrical shells with two refined higher order models*, Journal of Thermal Stresses, 41(1), 54–79.

Reddy J.N., 2004, *Mechanics of Laminated Composite Plates and Shells. Theory and Analysis*, CRC Press, New York.

Development of algorithmization bases for jet treatment evaluation modes of product curvilinear surfaces

Zinoviy Stotsko ORCID ID: 0000-0003-0423-8561

Lviv Polytechnic National University
Institute of Mechanical Engineering and Transport
Department of Equipment Design and Automotive Engineering, Lviv
email: zinoviy.a.stotsko@lpnu.ua

Tetyana Stefanovych ORCID ID: 0000-0002-8577-4755

Lviv Polytechnic National University
Institute of Computer Science and Information Technologies
Department of Computer-Aided Design, Lviv
email: tetyana.o.stefanovych@lpnu.ua

ABSTRACT

A method and algorithm for evaluating the angular and linear velocities of jet nozzles or products are proposed to ensure uniform jet treatment for the curvilinear surfaces of products. This is considered for two cases such as maintaining a constant distance from the nozzle end to the surface and maintaining a constant attack angle. Uniform processing is achieved by adjusting these velocities. This approach can be used in jet processing for ensuring a surface's quality, which will have different applications in the future.

Keywords: jet treatment, technological equipment, mechanical movement, process modes, curvilinear surface

1. Introduction

Any machine-building production requires productive and cheap methods for processing the metal parts of technological equipment. Such methods include a group of methods that are collectively known as "jet processing" in which multiphase jets are used as a tool. Depending on the physical nature and number of phases, there are methods of treatment with dry abrasives (or shots), those with wet abrasives (or shots), those that use cavitation in the liquid phase (or flooded jets), and so on. These methods can be used in both final technological operations (for example, to strengthen or decorate the surfaces of products) and in the preparation of surfaces for further processing (in particular, for coating operations). The advantages of jet processing are especially evident with the increases in size and complexity of a product's shape, making it a sometimes non-alternative method for achieving the desired quality characteristics of product surfaces. One of the basic requirements for any method of treatment is the predictability of the accuracy and quality of the products that are obtained after applying this method. The proper choice of technological modes can guarantee perfect results of any jet treatment. However, the need to take a significant amount of input data into account (namely, the parameters of the equipment, the jet, the working medium, the physical and mechanical properties of the material, the shape of the treated surfaces, and the lack of clear recommendations) significantly complicate this process – especially in the case of processing curved surfaces. Therefore, an urgent task is the mathematical modeling of a jet treatment for curved surfaces of products by utilizing automated computing systems. The results of mathematical modeling will form the basis of design and technological solutions for those industries in which jet treatment is implemented or used.

An analysis of the literature revealed a significant number of experimental studies for different methods of jet processing. The purpose of these studies was to solve spe-

cific tasks that are related to the processing of certain grades of materials (Li, Jiang 2020; Liu, Liao 2010; Slat et al. 2018; Wang et al. 2015). In Ukraine, the basics of the theoretical research of jet processing were developed in Salenko O.F. et al. (2005) and Salenko A.F. et al. (2016). The mathematical modeling of jet processing that uses the energy concept is discussed in detail in Stotsko and Stefanovych (2011a, 2011b). The energy concept is based on the energy conservation law, according to which the energy that is provided by the working medium of a jet (except for losses at different processing stages) is converted into work to change the shape and stress state of a product's surface. Determining the mass distribution of the working medium along a treated surface trajectory with variable processing modes for the case of jet movement along a flat stationary surface and for the case of jet movement along the radius of a rotating faceplate surface was described in Stotsko and Stefanovych (2013). Analytical dependencies for determining a jet's attack angle of the working medium for any point of a surface during treatment by a stationary jet were obtained in Stotsko and Stefanovych (2013). The change of an attack angle is simulated for flat-surface treatment with shock and sliding jets, for spherical and cylindrical surface cross-sections, and curvilinear surfaces of arbitrary shapes that are given by the corresponding analytical equations.

The literature analysis allowed to determine those problems that required further theoretical research. One such task is developing an approach for determining the modes of jet treatment for curvilinear surfaces in order to ensure uniform processing. This can be achieved by maintaining a constant distance from the nozzle end to the surface and maintaining the perpendicularity of the nozzle axis to the curved surface generatrix at the process point by moving the treated surface and changing the nozzle inclination.

To achieve this aim, the following tasks need to be solved:

- formalize jet treatment for curvilinear surfaces of product;
- developing mathematical models to determine processing modes;
- performing quantitative assessment of processing modes that provide uniformity of treatment over entire curved surface in its movement relative to jet apparatus nozzle.

2. Developing mathematical models

2.1. Formalize jet treatment for curvilinear surfaces of product

The essence of jet treatment affects a treated surface with a multiphase jet. While interacting with a surface, a jet changes its state, modifying and removing the surface layers of a material or having a combined effect.

The jet-treatment scheme of a curved surface is shown in Figure 1. The jet apparatus' nozzle (1) forms a multiphase jet (2). The working medium of the jet moves to the curved surface (3) at a high speed. The treatment is performed in the area of the contact of the jet's working medium (2) with the surface (3).

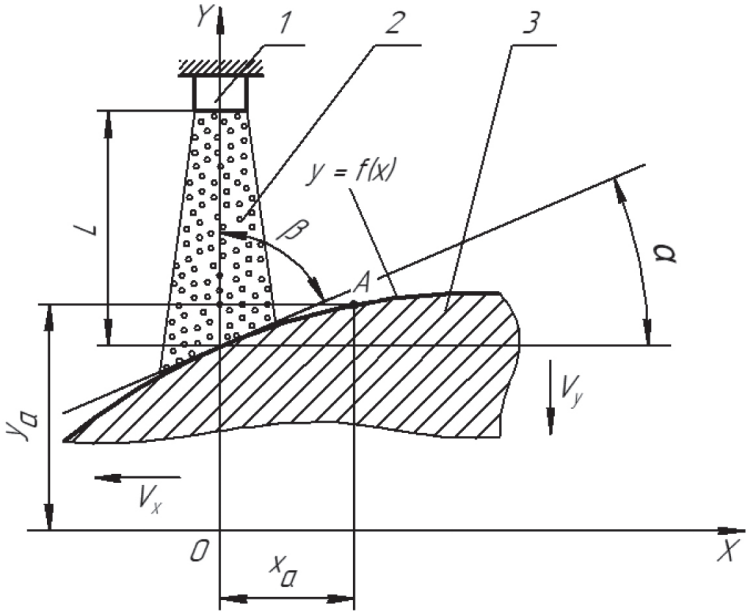

Fig. 1. Scheme of jet treatment of curved surface for L = const, $\alpha \neq$ const, and $\beta \neq$ const: 1 – nozzle; 2 – jet; 3 – surface; L – distance from nozzle to surface; α – angle of surface inclination; β – impingement angle; V_x, V_y – velocities of surface

During the treatment of a product with a curved surface, however, both distance L from the nozzle to the surface and jet attack angle β will change if the product moves relative to the nozzle. This causes a change in the treatment mode and, accordingly, the instability of the quality parameters of the treated surface. The stability of the surface-processing modes can be ensured if the nozzle axis of the jet apparatus (1) will remain permanently perpendicular to the generatrix of the treated surface; i.e., the attack angle of the jet must be equal to β = 90° (Fig. 2), and the distance from the nozzle end to the surface must be constant (L = const). Depending on the treated surface profile, the jet apparatus nozzle must oscillate with an angular velocity ù along an arc trajectory in order to fulfill these conditions. The position of the nozzle axis is determined by the angle of generatrix inclination α to the OX axis. The cross-section of the curved surface (3) is given in the plane by the equation $y = f(x)$. During the treatment, the cross-section performs a plane-parallel motion that consists of translational motions along the OX

and OY axes. The velocity as related to the OX axis is denoted as V_x, and that as related to the OY axis is denoted as V_y.

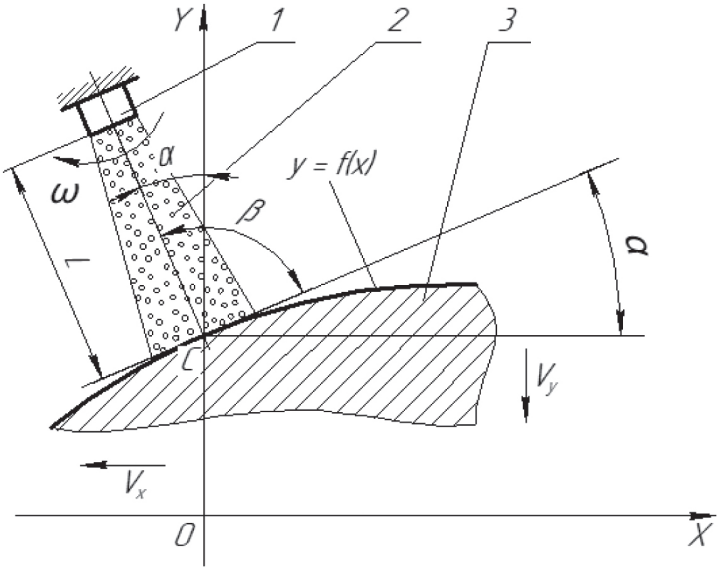

Fig. 2. Scheme of jet treatment of curved surface for L = const, $\alpha \neq$ const, and $\beta = 90°$: α – nozzle angular velocity; C – center of jet treatment

2.2. Developing mathematical models to determine processing modes

A case of treating a curved surface is under consideration according to the scheme in Figure 1. The treated surface moves at a constant velocity V_x. It is necessary to determine the velocity of surface movement V_y, provided a constant distance L from the nozzle end to the surface.

According to the geometric constructions (Fig. 1), it will be discovered how V_x and V_y relate to each other with reference to the curved surface shape.

The shape of the curved surface can be set by the angle of surface generatrix inclination α to the OX axis. The value of α is defined as $\mathrm{tg}\alpha = dy/dx$. Linear velocity V_x is given as a derivative of coordinate x from time t; namely, $V_x = dx/dt$ (where $dx = V_x dt$). Substitute dx into the formula for determining $\mathrm{tg}\alpha$ and we get $\mathrm{tg}\alpha = dy/V_x dt$ or $\mathrm{tg}\alpha = V_y/V_x$. Thus, the ratio between the V_x and V_y linear velocities will be $V_y = V_x \mathrm{tg}\alpha$:

$$V_y = V_x \frac{df(x)}{dx} \tag{1}$$

For the partial case when the product surface is a plane ($\alpha = 0$), velocity V_y will be equal to zero – this is true when the product does not move in the transverse direction.

It is possible to determine surface velocity V_y under a predetermined V_x and provided a constant distance L from the nozzle end to the surface using Formula (1).

Consider how to mathematically describe a curved surface in an XOY fixed-coordinate system depending on its shape and nature of motion. When $V_x = 0$ and $V_y = 0$, the equation of the surface in the cross-section will look like $y = f(x)$ for a stationary surface. The equation takes the form of $y = f(x, t)$ if the surface moves and V_x and $V_y \neq 0$. For an arbitrary Point A (Fig. 1) that lies on a curved surface and moves translationally along the OX and OY axes, the equation of its motion can be written as follows:

$$\begin{aligned} x &= x_a + V_x t \\ y &= y_a + V_y t \end{aligned} \tag{2}$$

Assume as a partial case that the surface cross-section is a straight line – the equation of which can be given by analytical dependence:

$$y = a + bx \tag{3}$$

Substituting Formulas (2) into Equation (3) and given the motion of Point A, $y_a + V_y t = a + b(x_a + V_x t)$ or $y_a = a + b(x_a + V_x t) - V_y t$ is obtained.

In the general case, the line equation for its displacement with velocities V_x and V_y is obtained:

$$y = a + b\left[x + (V_x - V_y)t\right] \tag{4}$$

At the initial moment of time $t = 0$ and under the conditions of $V_x = 0$ and $V_y = 0$, Equation (4) will turn into Equation (3); this confirms the correctness of its derivation. Thus, the surface that is given in the cross-section as the line can be described using Equation (4), which takes its shape and nature of motion into account.

Suppose as a partial case that the surface cross-section is a cubic parabola that is given by the following analytical dependence:

$$y = x^3 \tag{5}$$

Substituting Formulas (2) into Equation (5) given the motion of Point A, $y_a + V_y t = (x_a + V_x t)^3$ or $y_a = x_a^3 + 3x_a{}^2 V_x t + 3x_a V_x^2 t^2 + V_x^3 t^3 - V_y t$ is obtained.

In the general case, the cubic parabola equation for its displacement with velocities V_x and V_y can be written as follows:

$$y = x^3 + (3x^2 V_x - V_y)t + 3xV_x^2 t^2 + V_x^3 t^3 \tag{6}$$

At the initial moment of time $t = 0$ and under the conditions of $V_x = 0$ and $V_y = 0$, Equation (6) will turn into Equation (5); this confirms the correctness of its derivation. Thus, the surface that is given in the cross-section as the cubic parabola can be described using Equation (6), which takes its shape and nature of motion into account.

Consider the case according to Figure 2 for determining nozzle angular velocity ω. The nozzle must oscillate with angular velocity ω along an arc trajectory for ensuring uniform processing. Angular velocity ω is given as the derivative of angle α over time t; i.e., $\omega = d\alpha/dt$. In turn, angle α depends on the curved surface shape, which is $\text{tg}\alpha = df(x, t)/dx$; whence:

$$\alpha = \text{arctg}\frac{df(x,t)}{dx} \tag{7}$$

Residually, nozzle angular velocity ω along the arc trajectory is as follows:

$$\omega = \frac{d\left(\text{arctg}\dfrac{df(x,t)}{dx}\right)}{dt} \tag{8}$$

2.3. Recommendations for ensuring uniform jet treatment

Therefore, to comply with the conditions of uniform treating (namely, providing a constant distance from the nozzle end to treated surface $L = \text{const}$ and providing a constant attack angle of the jet to treated surface $\beta = 90°$; in other words, the perpendicularity of the nozzle axis of the jet apparatus to the curved surface generatrix), it is necessary to set the following processing modes:

- product must carry out translational motion that is described in Formulas (2);
- linear velocities of product or nozzle of jet apparatus must correspond to Relationship (1);
- nozzle angular velocity must comply with Equation (8).

Based on the above theoretical approach, an algorithm can be proposed for determining the V_x, V_y, ω modes:

1) determine curve equation $y = f(x)$ as line of intersection of XOY plane and curved surface of product;
2) choose Point C with coordinates $(0, y_c)$ in which curve $y = f(x)$ intersects with OY axis and in which center of jet treatment is located;
3) set L (i.e., distance from Point C to nozzle end of jet apparatus);

4) set surface velocity V_x relative to OX axis as constant value;
5) define time function for curve as $f(x, t)$;
6) determine surface velocity $V_y(x, t)$ relative to OY axis;
7) determine angle of surface inclination α at Point C as $f(x, t)$;
8) determine nozzle angular velocity ω as derivative of α in time t (namely, $\omega = d\alpha/dt$).

This algorithm can be used to obtain the graphical dependencies for the analysis of the jet-processing modes for different surface shapes.

3. Results and discussion

Consider one of the simplest cases for which a curved surface cross-section is a straight line – the general equation of which is given by Formula (3). Take the value of constant term a that is equal to 0 and coefficient b that is equal to 1; then, Formula (3) will be $y = x$. The coordinates of Point C (where the line intersects with the OY axis) are (0, 0). Distance L from C to the nozzle end is set as being equal to 1, as to the surface velocity V_x. If velocity V_x is equal to 1, then $x(t) = t$, and the time function for the curve can be written as $y(t) = t$. Determine surface velocity $V_y(x, t)$ by (1); i.e., $V_y = V_x$. That is, when moving the workpiece surface that is given by cross-sectional equation $y = x$ relative to the OX axis at a constant velocity of 1 to ensure a constant distance from the nozzle end to the workpiece, this surface must be moved relative to the OY axis at a velocity of 1 as well. Obviously, the tangent of the angle of the surface inclination will be equal to 1, and the angle itself will be 45°. For the constant angle, the value of the angular velocity for Equation (8) will be 0; i.e., it is enough to orient the nozzle that is fixed relative to the treated surface providing an attack angle of 90°.

Consider the case in which the curved surface cross-section is a cubic parabola – the equation of which is given by Formula (5). The cubic parabola equation as it moves with velocities V_x and V_y is described by Expression (6). Similar to the previous case, the coordinates of Point C are (0, 0). Distance L from Point C to the nozzle end is set as being equal to 1, as is surface velocity V_x relative to the OX axis. If velocity V_x is 1, then $x = t$, and the time function for the curve can be written as $y(t) = t^3$. Surface velocity $V_y(x, t)$ by Equation (1) is defined as $V_y(t) = 3t^2$. Graphs of the linear velocities for a curved surface (the cross-section of which is given by a cubic parabola) are shown in Figure 3. The angle of surface inclination α at Point C is determined by Equation (7) as $\alpha(t) = \text{arctg}(3t^2)$, and angular velocity ω is determined by Formula (8) as $\omega(t) = 6t/(9t^4+1)$. Graphs for the angle of surface inclination α and angular velocity ω are shown in Figure 4.

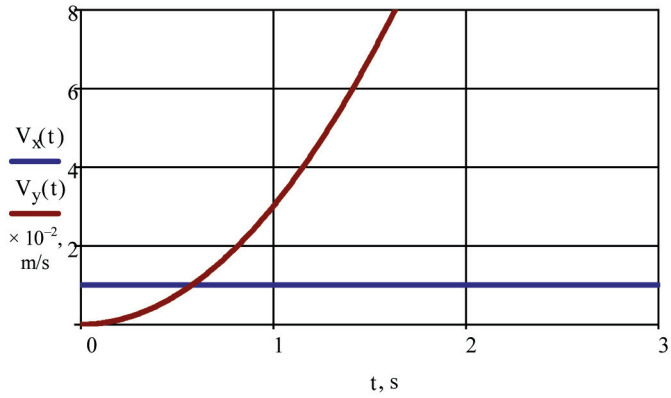

Fig. 3. Linear velocities of treated surface:
V_x – relative to OX axis; V_y – relative to OY axis

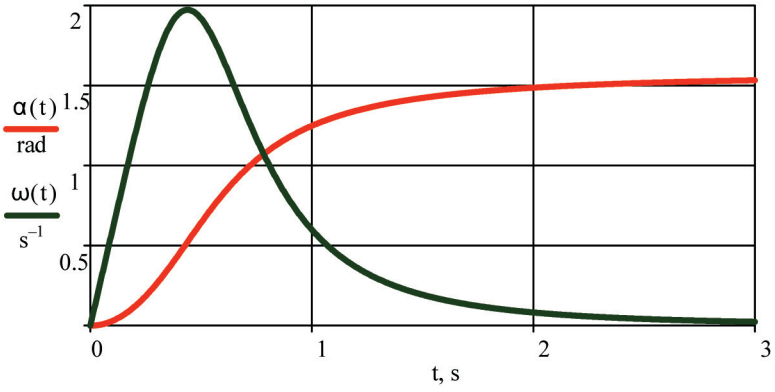

Fig. 4. Jet-processing modes associated with oscillating movement of nozzle:
$\alpha(t)$ – angle of surface inclination; $\omega(t)$ – nozzle angular velocity

4. Conclusions

A mathematical approach that will allow for the uniform jet treatment of curved surfaces by determining the processing modes (namely, the linear and angular velocities of the product or the jet apparatus) is proposed. This is considered for cases for which the uniformity of a curved-surface treatment is achieved by maintaining a constant distance from the nozzle end to the surface or maintaining a constant attack angle of the jet. For these cases, mathematical dependencies were obtained for determining the linear and angular velocities by using a graphical representation of the jet treatment. Based on the developed mathematical approach, an algorithm for determining the jet-treatment modes has been proposed, and the graphs of the linear and angular

velocities for different surface shapes over time have been obtained. In further research, it is planned to evaluate the quality characteristics of a product's curvilinear surfaces that can be obtained by jet treatment.

REFERENCES

Li X., Jiang C., 2020, *Numerical simulation analysis of shot peening residual stress on aluminum alloy surface based on finite element method*, 6th International Conference on Dependable Systems and Their Applications (DSA), 183–190.

Liu J., Liao R., 2010, *Simulation of shot peening process using combined hardening model*, International Conference on E-Product, E-Service and E-Entertainment, 1–4.

Salenko A.F., Shchetinin V.T., Gabuzyan G.V., Nikitin V.A., Novikov N.V., Klimenko S.A., 2016, *Cutting of polycrystalline superhard materials by jet methods*, Journal of Superhard Materials, 38(5), 351–362.

Salenko O.F., Strutyns'kyy, Zahirnyak M.V., 2005, *Efektyvne hidrorizannya*, KDPU, Kremenchuk.

Slat W.S., Malau V., Iswanto P.I., 2018. *The effects of shot peening treatment on the hardness and fatigue strength of HQ 805*, International Conference on Applied Science and Technology (ICAST), 142–145.

Stotsko Z.A., Stefanovych T.O., 2011a, *Investigations on the machine parts treatment by non-bound blast particles*, Journal of Achievements in Materials and Manufacturing Engineering, 49(2), 440–459.

Stotsko Z.A., Stefanovych T.O., 2011b, *Surface layer modelling and diagnostic after loose solid balls treatment*, Przetwórstwo Tworzyw, 17(6), 529–533.

Stotsko Z.A., Stefanovych T.O., 2013, *Modelling of abrasive blasting technological modes for curvilinear surfaces of machine parts*, Przetwórstwo Tworzyw, 19(1), 54–57.

Wang R., Xu J., Li G., 2015, *Intelligent prediction of jet shot peening surface roughness*, 4th International Conference on Computer Science and Network Technology (ICCSNT), 786–789.

Development of microcontroller-based temperature and humidity data logger

Andriy Holovatyy ORCID ID: 0000-0001-6143-648X

Lviv Polytechnic National University
Institute of Computer Science and Information Technologies
Department of Computer-Aided Design Systems, Lviv
email: andrii.i.holovatyi@lpnu.ua

Roman Panchak ORCID ID: 0000-0002-6422-7656

Lviv Polytechnic National University
Institute of Computer Science and Information Technologies
Department of Computer-Aided Design Systems, Lviv
email: roman.t.panchak@lpnu.ua

Mykhaylo Lobur ORCID ID: 0000-0001-7516-1093

Lviv Polytechnic National University
Institute of Computer Science and Information Technologies
Department of Computer-Aided Design Systems, Lviv
email: mykhaylo.v.lobur@lpnu.ua

ABSTRACT

In this paper, the developed hardware and software of a microcontroller-based temperature and humidity data logger has been described. The device measures temperature and humidity, displays the temperature and humidity values on an LCD screen, and writes them to a microSD memory card. The microcontroller-based temperature and humidity data logger has a menu that allows users to set up its operation mode. The microcontroller-based temperature and humidity data logger consists of an Arduino Uno R3 board on an ATmega328P-PU microcontroller, an HTU21D digital temperature and humidity sensor, a RobotDyn shield with RTC IC DS1307, and an HD44780 alphanumeric LCD micro SD memory card reader. The electrical circuit of the microcontroller data logger was designed in the Proteus CAD system. An operation algorithm of the microcontroller temperature and humidity data logger was developed. The software modules for communicating with the HTU21D digital temperature and humidity sensor and outputting information to the alphanumeric LCD module (based on the HD44780 controller) have been created, along with the main data-processing software. The model of the microcontroller-based temperature and humidity data logger in Proteus ISIS was created and simulated. A prototype of the microcontroller-based temperature and humidity data logger was also created and tested.

Keywords: microcontroller-based temperature and humidity data logger, HTU21D digital humidity and temperature sensor, RobotDyn shield micro SD card reader + RTC DS1307, HD44780 alphanumeric LCD module, ATmega328P-PU microcontroller, Proteus VSM, C/C++, embedded software, Arduino IDE

1. Introduction

The current state of the development of electronics makes it possible to create cheap measuring systems that are based on microcontrollers and various sensors. In particular, a microcontroller data logger (temperature and humidity data logger) can be created. Temperature and humidity data loggers are compact stand-alone devices that record ambient temperature and humidity values for a specified time at specified intervals, store them, and transmit this data to external devices in a specified format.

Temperature and humidity data loggers are widely used in production and other activities in which there are increased requirements for the quality of the environmental parameters:

- in health care institutions – in special medical buildings, laboratories, and operating rooms;
- in repositories of valuables, objects of historical significance, and art objects;
- in premises of exact and ultrapure production;
- in agricultural premises of livestock and poultry complexes (in food storage);
- in pharmaceutical production and storage of products;
- in logistics companies for transportation and storage of products that are critical for storage conditions.

The range of the tasks that can be solved by using temperature and humidity data loggers are as follows:

- environment monitoring and detection of violations of storage conditions or production;
- use of data-logger information to organize technological process control;
- prevention of violation of technological requirements in production and storage of products.

Autonomous temperature and humidity data loggers are used to record measured temperature and humidity readings into their memory for further analysis and processing on a computer. These autonomous data loggers consist of a wide range of models that are suitable for different tasks depending on the measuring range and other characteristics (*Data loggers for temperature and humidity – the fields of application* n.d.)

The purpose of this work is to develop the hardware and software of a microcontroller-based temperature and humidity data logger.

Nowadays, many modern devices are built on microcontrollers. The important feature of microcontrollers is that their use makes it easier and cheaper to develop a device. A microcontroller can control various devices and receive data from them with a minimum number of additional nodes (because quite a lot of peripherals are already on the chip). Devices that are built on microcontrollers feature smaller dimensions and low power consumption.

2. Hardware design of microcontroller-based temperature and humidity data logger in Proteus VSM

A microcontroller-based data logger must measure temperature and humidity and write these values on a microSD memory card. In Figure 1, a block diagram of a microcontroller-based temperature and humidity data logger is shown. The data logger hardware consists of an Arduino Uno R3 board with an ATmega328P-PU MCU (Banzi 2011; Gertz, Di Justo 2012; Oxel, Blemings 2009), an HTU21D digital temperature and humidity sensor (*Temperature and humidity sensor HTU21D datasheet* n.d.), a RobotDyn module with RTC IC DS1307 and microSD card reader (*Description of RTC+microSD-card shield from RobotDyn* n.d., *Real-time Clock DS1307 datasheet* n.d.), a four-key keypad, and an HD44780 alphanumeric 16 × 2 LCD module (*Liquid-Crystal Display HD44780 controller/driver datasheet* n.d.). The Arduino Uno microcontroller reads data from the HTU21D sensor, processes it, and writes it to the memory card

according to its operation algorithm in real time. The current temperature and humidity values and date are displayed on the alphanumeric LCD module.

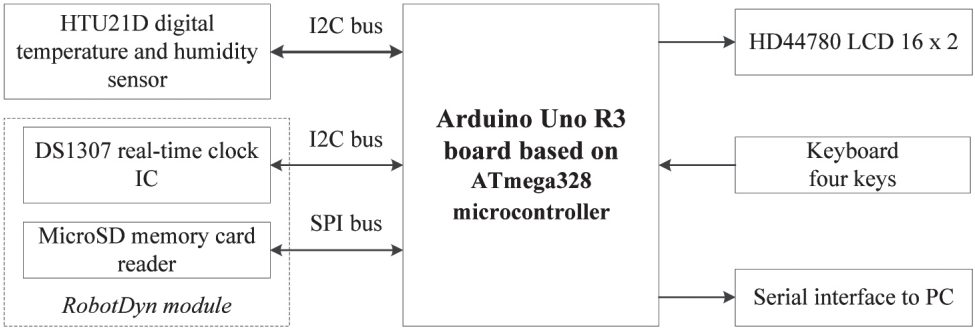

Fig. 1. Block diagram of microcontroller-based temperature and humidity data logger

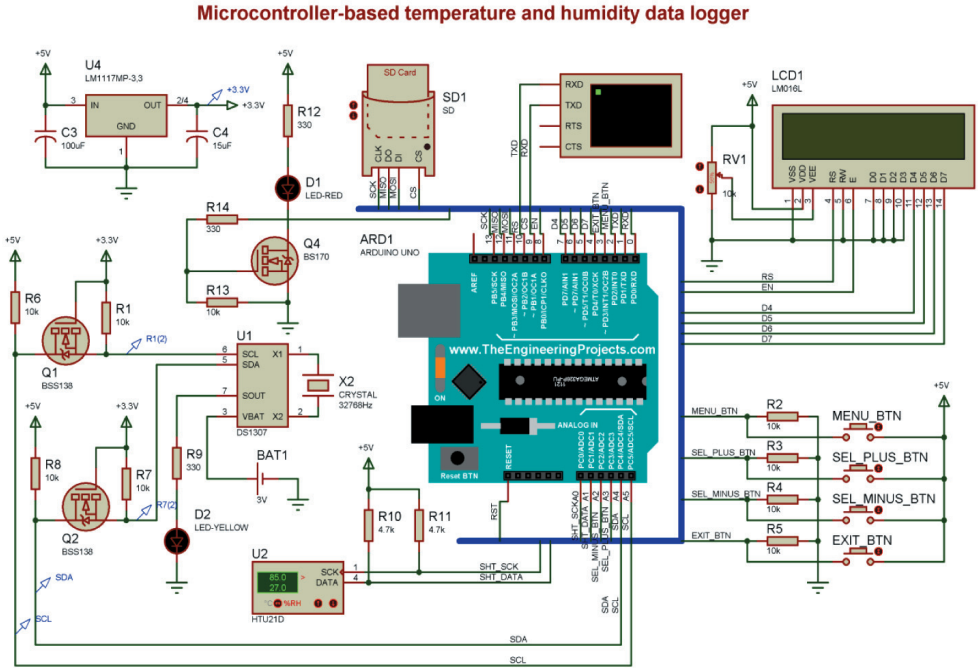

Fig. 2. Hardware of microcontroller-based temperature and humidity data logger designed in Proteus VSM

In Figure 2, the designed hardware of the data logger in CAD Proteus is shown. The HTU21D temperature and humidity sensor module is connected to the Arduino Uno board using the I2C interface. The synchronization (SCK) and data (SDA) pins of

the sensor are connected according to the A4 (SDA) and A5 (SCL) pins of the I2C bus of the Arduino Uno board. The RTC IC DS1307 is connected to the Arduino Uno board on the I2C bus. The synchronization (SCL) and data (SDA) lines of the I2C interface bus on the Arduino Uno board are located on Pins 19 (A5/SCL) and 18 (A4/SDA). The microSD card reader is connected to the Arduino Uno card via the SPI interface. The SCK pin of the card reader is connected to Pin 13 (PB5/SCK), the MISO pin – Pin 12 (PB4/MISO), the MOSI pin – Pin 11 (~ PB3/MOSI/OC2A), and the CS pin – Pin 9 (CS) of the Arduino Uno board.

The HD44780 LCD module is connected to the pins of the PBx and PDx ports. The RS output of the LCD module is connected to Pin 10 (PB2) of the Arduino Uno board. The LCD E output is connected to Pin 8 (PB0) of the Arduino Uno board. Data outputs D4…D7 are connected to Pins 7…4 (PD7/AIN1, ~ PD7/AIN2, PD5/T1/OC0B, PD4/T0/XCK) of the Arduino Uno board. The MENU_BTN button is connected to Pin 2 (PD2/INT0), the SEL_PLUS_BTN (select/enlarge) button – Pin 17 (PC3/ADC3), the SEL_MINUS_BTN button (select/reduce) – Pin 16 (PC2/ADC2), and the EXIT_BTN for exiting from the menu to the operation mode – Pin 3 (~PD3/INT1/OC2B) of the Arduino Uno board. When the MENU_BTN button is pressed, the INT0 interrupt will be generated, and the program will call its processing function.

3. Operation algorithm of microcontroller-based temperature and humidity data logger

In Figures 3 and 4 (on the interleaf), the block diagrams of the operation algorithm of the microcontroller-based temperature and humidity data logger are shown.

4. Simulation and prototype testing of microcontroller-based temperature and humidity data logger

The data-logger software is compiled and linked to the hex file that is programmed into the MCU flash memory. The data-logger software is written in C/C++ using Arduino IDE (Arduino n.d.). Before downloading the firmware to the device (data logger), its operation can be checked on the created model in Proteus ISIS. A simulation of the device allowed us to detect existing errors in the software and eliminate them without loading it several times into the microcontroller's flash memory. In Proteus, the simulation and debugging of quite complex projects can be performed that can have several microcontrollers and even from different families. In Figure 5, the simulation of the microcontroller temperature and humidity data logger is shown.

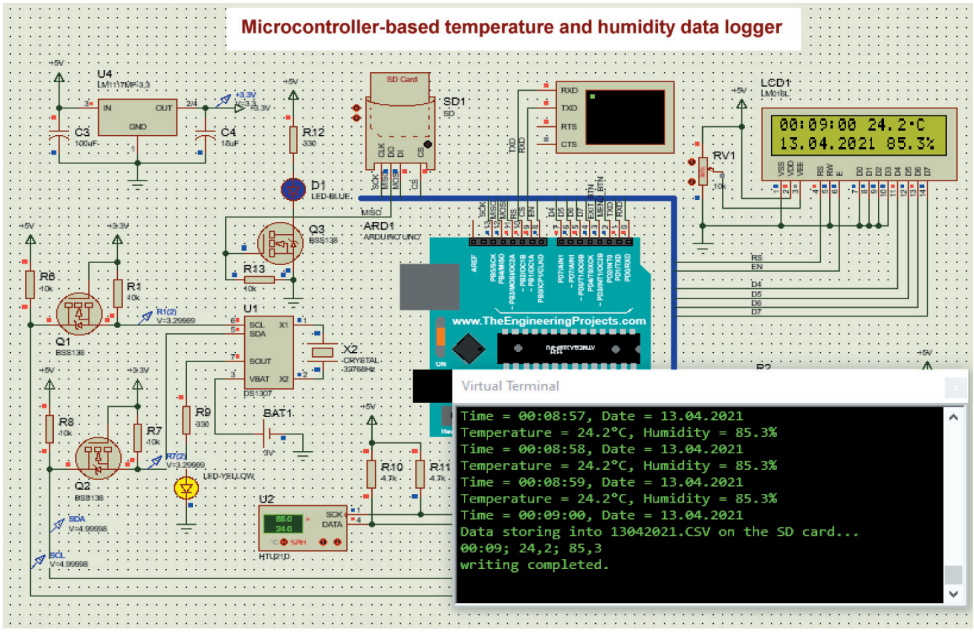

Fig. 5. Simulation of microcontroller-based temperature and humidity data logger in Proteus ISIS

In Figure 6, the test circuit (prototype) of the microcontroller-based temperature and humidity data logger is shown. In Figures 7 and 8, the obtained results of the testing of the microcontroller-based temperature and humidity data logger are shown

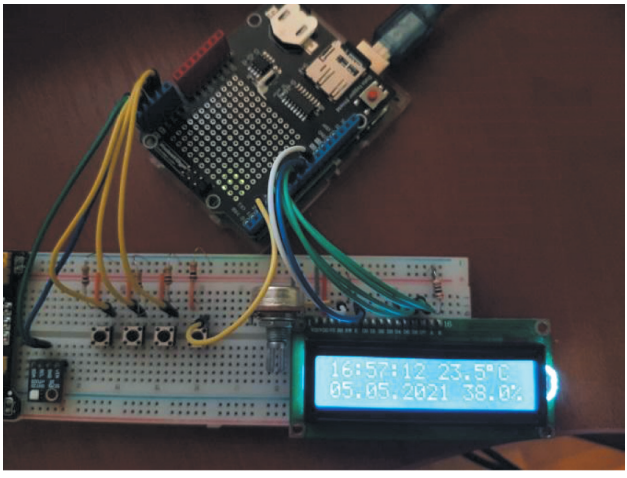

Fig. 6. Test circuit (prototype) of microcontroller-based temperature and humidity data logger

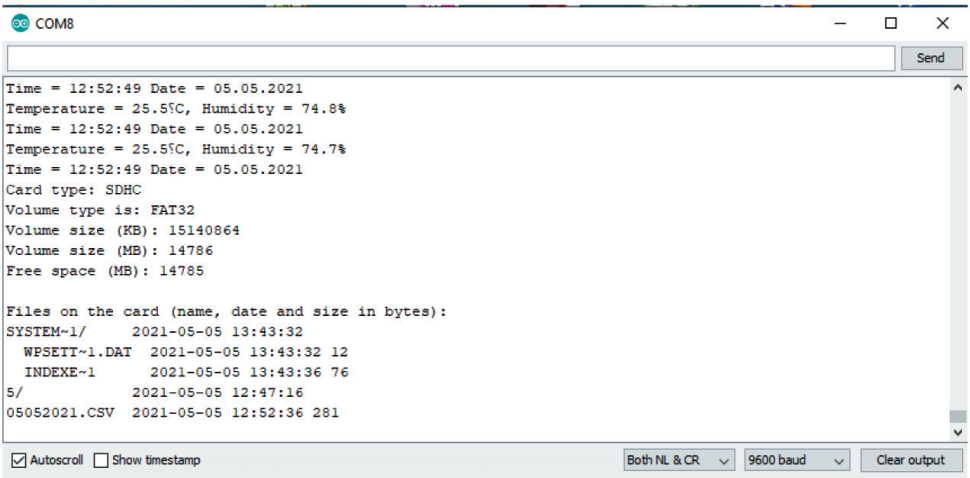

Fig. 7. Information output to serial monitor

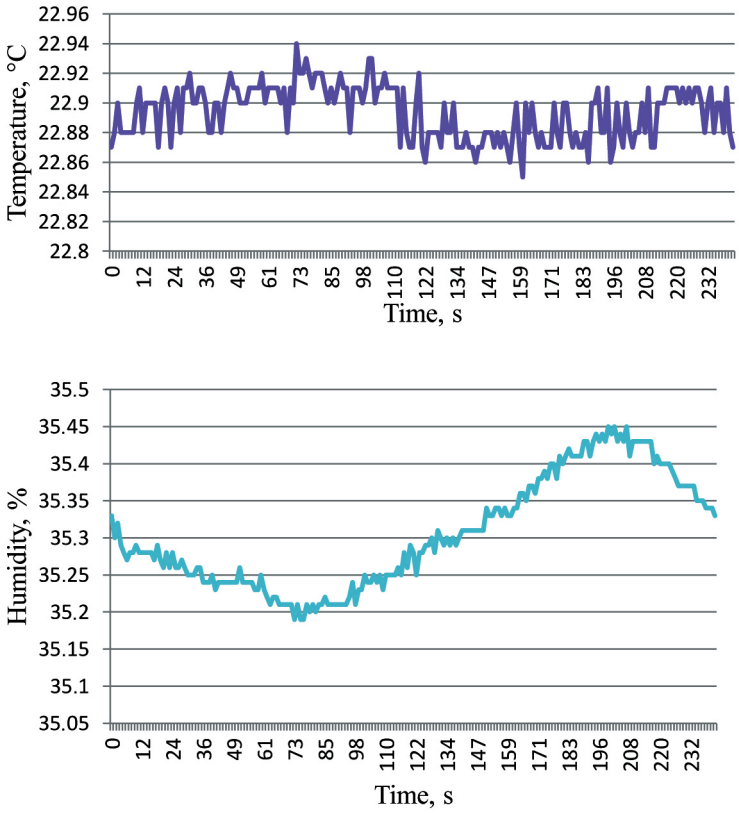

Fig. 8. Excel graphs of temperature and humidity data that was collected by data logger

5. Conclusions

In this work, the hardware and software of a microcontroller temperature and humidity data logger have been developed. The device measures temperature and humidity, displays the measured temperature and humidity values on an HD44780 alphanumeric 16 × 2 LCD module, and writes them in a .csv file to a microSD memory card. An electronic circuit of the microcontroller temperature and humidity data logger in the Proteus CAD system has been designed. The operation algorithm and data-processing software of the microcontroller-based temperature and humidity data logger have been developed. The software modules for communicating with an HTU21D digital temperature and humidity sensor for outputting information to the HD44780 alphanumeric LCD module have been created. The model of the microcontroller-based temperature and humidity data logger in Proteus ISIS has been created and tested.

The prototype of the microcontroller-based temperature and humidity data logger has been developed and tested.

REFERENCES

Arduino [electronic resource on Arduino IDE]: https://www.arduino.cc/en/Main/Software [10.11.2021].

Banzi M., 2011, *Getting Started with Arduino*, 2nd Edition, O'Really Media Inc., Sebastopol, CA, USA.

Data loggers for temperature and humidity – the fields of application [electronic resource]: https://www.testo.com/en-IN/products/datalogger-humiditys [10.11.2021].

Description of RTC+microSD-card shield from RobotDyn [electronic resource]: https://arduino.ua/prod2645-shild-rtcsd-card-dlya-arduino-uno-ot-robotdyn, https://copperhilltech.com/blog/robotdyn-data-logger-shield-for-arduino-development-resources/ [10.11.2021].

Gertz E., Di Justo P., 2012, *Environmental Monitoring with Arduino: Building Simple Devices to Collect Data about the World around Us*, O'Really Media Inc., Sebastopol, CA, USA.

Liquid-Crystal Display HD44780 controller/driver datasheet [electronic resource]: https://www.sparkfun.com/datasheets/LCD/HD44780.pdf [10.11.2021].

Oxer J., Blemings H., 2009, *Practical Arduino: Cool Projects for Open Source Hardware*, Springer-Verlag, New York.

Temperature and humidity sensor HTU21D datasheet [electronic resource]: https://datasheetspdf.com/pdf-file/1087268/TE/HTU21D/1, https://cdn-shop.adafruit.com/datasheets/1899_HTU21D.pdf [10.11.2021].

Real-time Clock DS1307 datasheet [electronic resource]: https://pdf1.alldatasheet.com/datasheet-pdf/view/123888/DALLAS/DS1307.html, https://datasheets.maximintegrated.com/en/ds/DS1307.pdf [10.11.2021].

Numerical tests of the power coefficient the VAWT with ODGV

Radosław Ptak

AGH University of Science and Technology
Faculty of Mechanical Engineering and Robotics
Department of Power Systems and Environmental Protection Facilities, Krakow
email: ptak@agh.edu.pl

Krzysztof Kołodziejczyk ORCID: 0000-0001-9479-7505

AGH University of Science and Technology
Faculty of Mechanical Engineering and Robotics
Department of Power Systems and Environmental Protection Facilities, Krakow
email: krzysztof.kolodziejczyk@agh.edu.pl

ABSTRACT

The article contains results of numerical tests and an analysis of the operation of a wind turbine with a vertical axis of rotation equipped with air guides. The studies show that the analyzed solution has a higher value of the power factor than the classic wind turbines with a vertical axis of rotation. As part of the numerical tests, the value of the power coefficient was determined depending on the speed ratio in the entire operating range, for several values of the air inflow velocity.

Keywords: vertical axis wind turbine, numerical modeling

1. Introduction

Obtaining energy from renewable sources, like never before, has become one of the most important areas. This is the result of many factors at the same time, incl. due to the greenhouse effect publicized in the media, the need to reduce CO_2 emissions, the shrinking of natural resources, and thus the desire to protect them, including maintaining the welfare (including natural resources) for future generations.

The article presents a numerical analysis of the operation of a wind turbine with a vertical axis of rotation with air blades. The conducted analyzes indicate that the obtained value of the power factor is higher than in classic wind turbines with a vertical axis. Currently, the typical design solution used in wind farms are horizontal axis turbines (HAWT) (Wiser et al. 2016). The basic element determining their popularity is much higher efficiency of obtaining energy from wind than other design solutions. The achievable power factor *Cp* (Hau 2006) is 0.4–0.5, while solutions with a vertical axis of rotation have a *Cp* value of 0.1–0.2. In addition, the HAWT design solutions allow for the creation of very tall structures, which allows the use of very large diameter rotors, which at the same time allows for the creation of units with relatively high power (Wiser et al. 2016). These constructions, however, are not free from disadvantages, e.g. landscape pollution and nuisance noise resulted in the introduction of restrictions related to their location, in particular the necessity to keep the distance from the spaces inhabited by people. The exhaustion of the available space allowing for the creation of new investments – wind farms, resulted on the one hand in the development of "off shore" solutions (Green, Vasilakos 2011), and on the other hand, increased interest in design solutions that are less burdensome for humans, i.e. vertical axis turbines (VAWT) (Bai et al. 2019; Leguizamón, Avellan 2020; Sobczak et al. 2020; Wicaksono, Tjahjana 2017; Wicaksono et al. 2018). One of the biggest problems with standard vertical axis wind turbine designs is their low efficiency. One of the ways to increase the *Cp* coefficient is the introduction of air deflectors (ODGV – Omni-Directional Guide Vanes), such a solution allows to increase the efficiency from a dozen to several dozen percent (Wicaksono, Tjahjana 2017).

The issue of the use of air deflectors in vertical wind farms is not fully understood. There are few studies in this field in the literature (Wicaksono, Tjahjana 2017, Wicaksono et al. 2018), in which it was verified whether the use of air deflectors would reduce the negative effect of "negative pressure". The tests were carried out by testing the turbine operating parameters for various blade configurations. The research shows that the use of guides allows not only to limit the impact of the incoming wind stream on the returning blades, but also increases the pressure on the propelling blades.

2. Numerical research

The subject of the research is an existing wind farm with a vertical axis of rotation, equipped with air guides. The structure of the power plant consists of the outer ring forming the guide vanes, and the inner ring, connected to the generator shaft, forming the turbine assembly (Fig. 1).

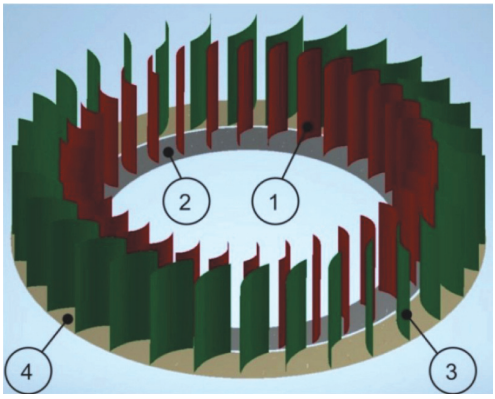

Fig. 1. Construction of one stage of the turbine: 1 – turbine blades, 2 – the inner ring of the turbine blades, 3 – air guide vanes, 4 – the outer ring forming the set of blades (Ptak, Kołodziejczyk 2021)

A numerical analysis of the flow through a wind turbine with a vertical axis of rotation was performed, including determination of the torque and power possible to be obtained.

The analyzed design solution was represented in a flat system as a cross-section in a plane perpendicular to the axis of the turbine. ANSYS Fluent software was used for the analysis. The flowing medium is air with parameters at a temperature of 20°C. The range of rotational speed of the rotating space was initially determined on the basis of the literature data for the speed ratio of the Savonius turbine and then finally determined on the basis of the simulations. The k-omega SST turbulence model was adopted in the analysis.

The analyzes were carried out for three different inflow velocities (on inlet scheme in Figure 2) from 4, through 8, and finally 12 m/s. Free outflow was modeled by setting relative pressure 0 Pa at the outlet. On both sides of computation domain free sleep walls was applied. The spinning domain, simulated as frame motion, was rotating with angular speed varying from 0 to 12 rad/s.

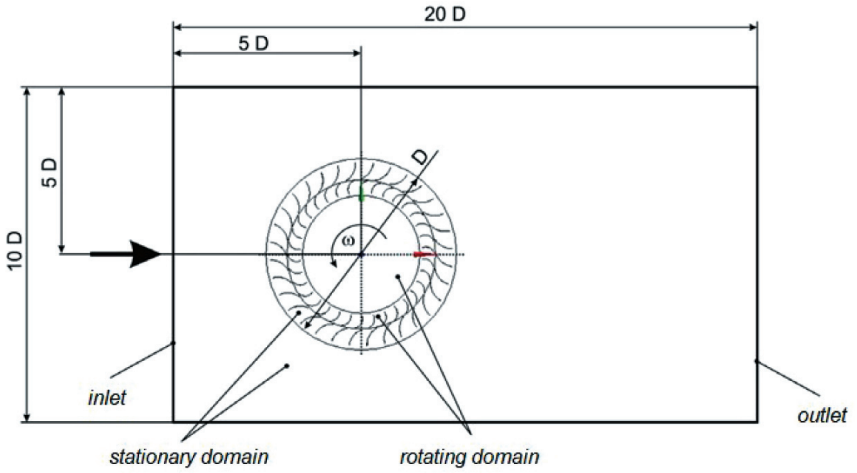

Fig. 2. Computational domain scheme
(Ptak, Kołodziejczyk 2021)

The computational grid, consisting of 1.0 million elements, ranging in size from 0.004 m to 0.3 m, was divided into five areas with varying degrees of compaction. The largest elements were in the outer sector of the computing domain, they decreased with the approach to the turbine, while the smallest elements, giving the highest accuracy of calculations, were located around the turbine blades and air guides.

The assumed EMS iterative convergence at the level of 10^{-4} was received. Also the value of torque changes was monitored (Tab. 1), the value of the changes in torque was below 1% during the calculation.

Table 1
The changes in torque during the calculation

Iteration number	1000	1500	2000	2500	3000
Torque [Nm]	57.421	57.107	57.074	56.925	56.901

The tip speed ratio (λ) is the quotient of the circumferential speed of the blade tip to the average speed of the wind entering the turbine. In other words it represents angular velocity in certain wind conditions regardless of the turbine's diameter. Simulations were performed for different values of the tip speed ratio and different values of the velocity of the incoming air stream. As a result of the simulation, the flow

through the wind turbine was obtained. The velocity and pressure distributions in the computational domain were obtained. The power coefficient was the relationship between the power generated by the turbine and the power of the wind stream that moves the turbine. For different values of the tip speed ratio at different wind speed the distribution of the power coefficient was obtained.

In the velocities distribution for lower tip speed ratios (Fig. 3) we can observe a few interesting occurrences. Before the turbine velocity is lower. On both sides velocity increases. Behind the turbine we can observe a characteristic aerodynamic shadow. And what is most the important, for the turbine itself (Fig. 4), a variable speed distribution in the rotor zone. In the velocity distribution for higher TSR (Fig. 5), beside all similarities for lower TSR, we can also observe swirling movements.

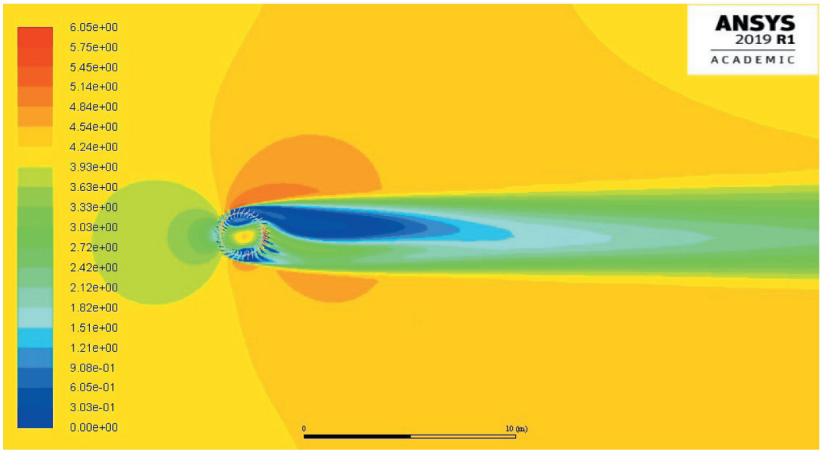

Fig. 3. Distribution of velocity [m/s] for lower TSR values

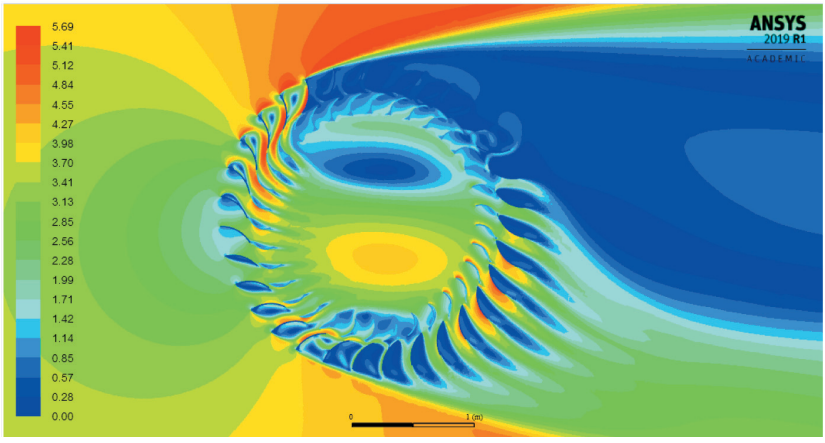

Fig. 4. Distribution of velocity [m/s] in rotor zone

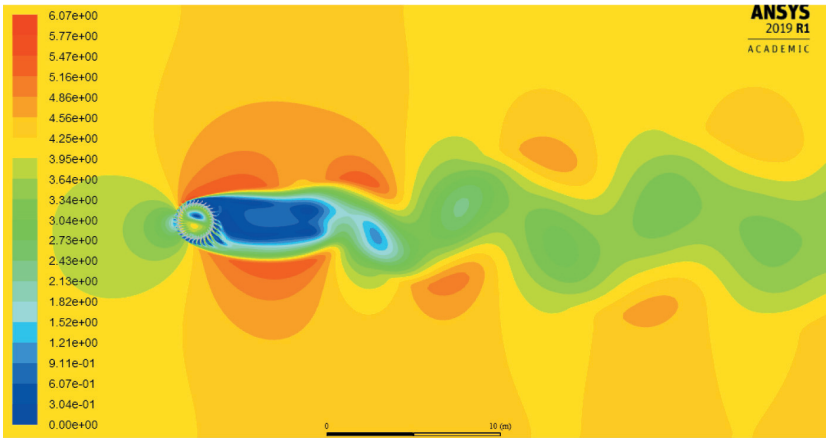

Fig. 5. Distribution of velocity [m/s] for higher TSR values

Analyzing pressure distribution (Fig. 6) we can draw a conclusion that the rotor driving force will be the result of both the hydrodynamic action of the air stream on the blades and the generation of force due to the pressure difference resulting from the shape of the rotor blade.

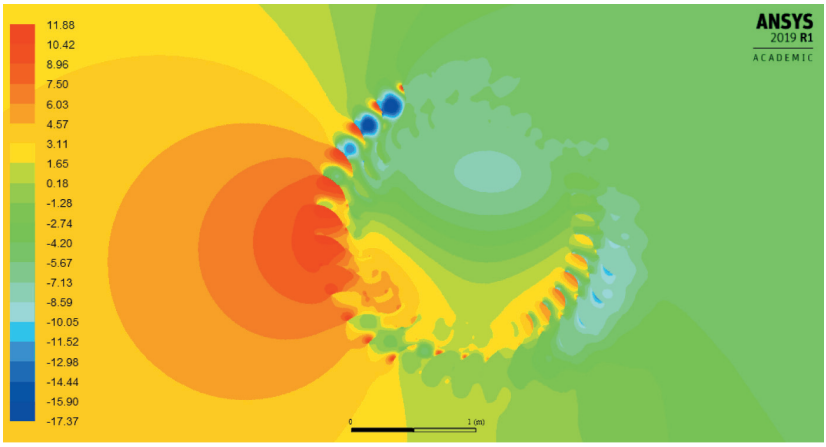

Fig. 6. Distribution of static pressure [Pa] in rotor zone

The chart (Fig. 7) shows the resulting power coefficient as a function of the speed ratio. As we can see, the curve is similar to the inverted parabola, typical for turbines with a vertical axis. After analyzing power coefficient for various values of inlet velocity we see that, regardless of the speed of inflow, the obtained values are at a similar level. With the tip speed ratio $\lambda = 0.7$, for the wind speed of 8 m/s, the power coefficient reached the highest value: $Cp = 25.4\%$.

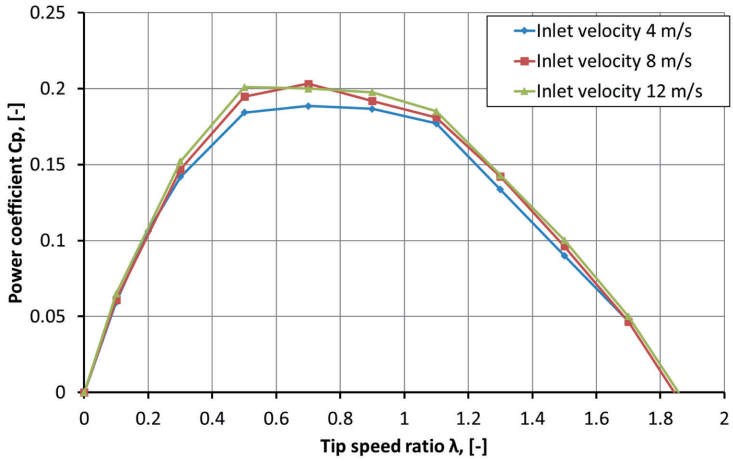

Fig. 7. Power coefficient for inlet velocities: 4 m/s, 8 m/s, 12 m/s

For various tip speed ratios, the torque chart has been created. Chart (Fig. 8) illustrates torque for a constant velocity inlet 8 m/s. As we can observe in the existing turbine it shows high starting torque. When the wind occurs, the turbine accelerates to the point where the torque generated on the turbine shaft is balanced by the generator load.

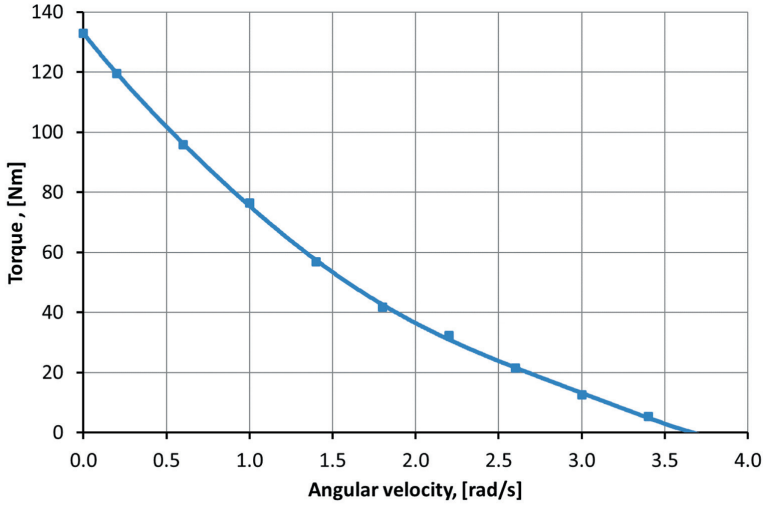

Fig. 8. The relationship between torque and angular velocity

3. Conclusions

The achieved maximum value of the power coefficient for considered wind turbine was above 25% for the tip speed ratio $\lambda = 0.7$. It locates the analyzed design solution in the

upper limit of the *Cp* coefficient value achieved by HAWT, however commercial solutions of horizontal axis wind turbines achieves more than 40% *Cp* coefficient, therefore VAWT's could be used in case when HAVT's cannot be used, but for the general purpose it would require further studies.

The high starting torque of the vertical wind turbine causes that such a structure does not require a starter, as in the case of many other wind turbines. It is worth noticing that such a constructional solution works with relatively low angular speed. This is a feature that has to be considered in two aspects. Wind turbines working with a high speed of rotation generate noise that is disruptive to the residents living nearby, therefore the installation of high-speed turbines is inadvisable in the vicinity of residential buildings where VAWT, working with lower rotational speed, could find their place. On the other hand lower angular speed, causes requirement to either apply a low speed generators, which are usually more expensive, either use multiplier, what one way or another increases costs.

The considered VAWT shows a high optimization potential. In the near future, we will be studying the ratio of the width of the blade ring to the turbine. It can also be valuable to check the geometry of the turbine blades and guiding vanes.

REFERENCES

Bai H.L., Chan C.M., Zhu X.M., Li K.M., 2019, *A numerical study on the performance of a Savonius-type vertical-axis wind turbine in a confined long channel*, Renewable Energy, 139, 102–109.

Green R., Vasilakos N., 2011, *The economics of offshore wind*, Energy Policy, 39(2), 496–502.

Hau E., 2006, *Wind Turbines – Fundamentals, Technologies, Application, Economics*, Springer-Verlag, Berlin – Heilderberg.

Leguizamón S., Avellan F., 2020, *Computational parametric analysis of the design of cross-flow turbines under constraints*, Renewable Energy, 159, 300–311. DOI: https://doi.org/10.1016/j.renene.2020.03.187.

Ptak R., Kołodziejczyk K., 2021, *Analiza numeryczna pracy turbiny wiatrowej o pionowej osi obrotu z kierownicami powietrza*, Przemysł Chemiczny, 100(9), 867–870.

Sobczak K., Obidowski D., Reorowicz P., Marchewka E., 2020, *Numerical Investigations of the Savonius Turbine with Deformable Blades*, Energies, 13(14), 3717. DOI: https://doi.org/10.3390/en13143717.

Wicaksono Y.A., Tjahjana D., 2017, *Computational study: The influence of omni-directional guide vane on the flow pattern characteristic around Savonius wind turbine*, AIP Conference Proceedings, 1788(1), 030016. DOI: https://doi.org/10.1063/1.4968269.

Wicaksono Y.A., Tjahjana D., Hadi S., 2018, *Influence of omni-directional guide vane on the performance of cross-flow rotor for urban wind energy*, AIP Conference Proceedings, 1931(1), 030040. DOI: https://doi.org/10.1063/1.5024099.

Wiser R., Hand M., Seel J., Paulos B., 2016, *The Future of Wind Energy, Part 3: Reducing Wind Energy Costs through Increased Turbine Size: Is the Sky the Limit*, Lawrence Berkeley National Laboratory, Electricity Markets and Policy Group, Berkeley.

Engineering drawing education using CAD tools

Andrzej Łukaszewicz ORCID ID: 0000-0003-0373-4803

Bialystok University of Technology
Faculty of Mechanical Engineering
Department of Machine Design and Exploitation, Bialystok
email: a.lukaszewicz@pb.edu.pl

Grzegorz Skorulski ORCID ID: 0000-0002-0022-7016

Bialystok University of Technology
Faculty of Mechanical Engineering
Department of Materials and Production Engineering, Bialystok
email: g.skorulski@pb.edu.pl

Mykhaylo Melnyk ORCID ID: 0000-0002-8593-8799

Lviv Polytechnic National University
Institute of Computer Science and Information Technologies
Department of Computer-Aided Design Systems, Lviv
email: mykhaylo.r.melnyk@lpnu.ua

Andriy Kernytskyy ORCID ID: 0000-0001-8188-559X

Lviv Polytechnic National University
Institute of Computer Science and Information Technologies
Department of Computer-Aided Design Systems, Lviv
email: andriy.b.kernytskyy@lpnu.ua

Andriy Zdobytskyi ORCID ID: 0000-0001-8044-9593

Lviv Polytechnic National University
Institute of Computer Science and Information Technologies
Department of Computer-Aided Design Systems, Lviv
email: andrii.y.zdobytskyi@lpnu.ua

Kostyantyn Kolesnyk ORCID ID: 0000-0001-9396-595X

Lviv Polytechnic National University
Institute of Computer Science and Information Technologies
Department of Computer-Aided Design Systems, Lviv
email: kostyantyn.k.kolesnyk@lpnu.ua

ABSTRACT

This paper presents selected aspects of engineering drawing education that are used in the Faculty of Mechanical Engineering, Bialystok University of Technology (BUT), and the Department of Computer-Aided Systems, Lviv Polytechnic National University (LPNU). Nowadays, this concept is inextricably linked with CAD and CAx techniques. Some issues of engineering drawing with 2D CAD education are outlined based on the authors' many years of experience in the teaching of mechanical engineering drawing, MCAD, ECAD, and MEMS.

Keywords: CAD, engineering drawing, online teaching, COVID 19

1. Introduction

Engineering drawing is an essential subject in engineering education (Bajkowski 2011; Bajkowski, Bajkowski 2019; Madsen, Madsen 2016; Morling 2010). Technical drawing – made in accordance with regulations and applicable rules – is the language that is used by engineers and technicians of all countries to communicate with each other. The universal and international importance of technical drawing enables inventions and improvements from around the world. Technical drawing is a form of the idealization and simplification of actual features of depicted objects in order to facilitate their descriptions. Technical drawing is a graphical representation that conventionally forwards accurate information about the shape, dimensions, and performance characteristics of individual parts, assemblies, and whole devices.

The extended experience of the authors in technical university teaching processes supported by many papers (Bortnikova et al. 2019; Jabłoński, Łukaszewicz 2013; Jabłoński et al. 2013; Kolesnyk et al. 2017; Łukaszewicz 2006; 2008a; 2008b; 2009a; 2009b; 2009c; 2010a; 2010b; 2011; 2014; Łukaszewicz, Kernytskyy 2011; 2012; Łukaszewicz et al. 2021; Melnyk et al. 2015; Panas, Łukaszewicz 2013; Zdobytskyi et al. 2021) provides an opportunity for a historical analysis and the forecasting of further methods of technical drawing teaching using CAD systems in both the mechanical and electromechanical fields (e.g., MEMS).

The paper presents selected aspects of engineering drawing education methods that are used in the Faculty of Mechanical Engineering, Bialystok University of Technology, and the Department of Computer-Aided Systems, Lviv Polytechnic National University, following the exile into online teaching due to COVID-19 (starting in March 2020 in Poland). Nowadays, this concept is inextricably linked with CAD techniques. Some issues of engineering drawing are outlined, along with CAD education and the possibility of online classes during pandemic times.

CAx (CAD/CAM/CAE) tools are widely used in engineering fields (Dankwort et al. 2004; González-Lluch et al. 2021; Havrylenko et al. 2020; Łukaszewicz et al. 2018a; 2018b; 2021). The main advantage of using CAx systems is the shortening of a product's time development. The ability to perform many types of CAE analyses (e.g., Mircheski et al. 2019; Sidun, Łukaszewicz 2017), visualizations, and technical documentations in design phases allows us to better fit the assumptions.

2. Problem statement

Engineering drawing and CAD learning in mechanical engineering education are the main prerequisites for further subjects such as the basics of machine design and others design subjects (e.g., Dankwort et al. 2004; Kok, Bayaga 2019; Łukaszewicz et al. 2018b; Ramos, Melgosa 2020).

After the introduction of compulsory online teaching in connection with the Covid-19 pandemic (March 2020), the use of CAD systems in a 2D module forced the use of computer tools in the process of teaching technical drawing during the first semester of studies in the case of "mechanics and mechanical engineering" and related fields.

As a result, the following challenges arose:

- possibility of online classes (official pandemic time starting in March 2020);
- ability for students to easily correct errors on drawings;
- easy possibility for teachers to check and make comments in drawings;
- in industry, practically no one uses handmade 2D documentation.

With the use of online learning platforms (e.g., Teams), this has become possible.

3. Mechanical engineering drawing education case

Figures 1 and 2 present drawings that were made by students during the first semester; the subject was "Engineering Drawing," and these drawings were made during the winter semester of the 2020/21 academic year. For 2D, CAD was used with the SolidWorks "drawing" environment (without a 3D model). Figures 3 and 4 show the teachers' comments and grades (each mark was made in the comments, and basic comments were in the conclusions). The main assumption is that 2D CAD can and should be used by students during the first semester of teaching technical drawing. No knowledge of 3D techniques is required at this stage of their education.

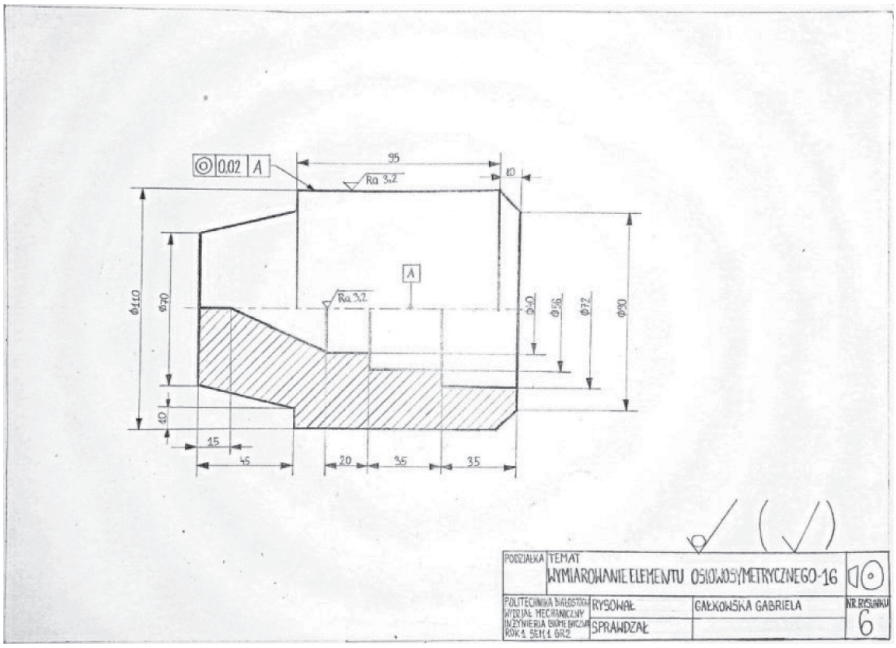

Fig. 1. Hand-drawn work, axi-symmetry part

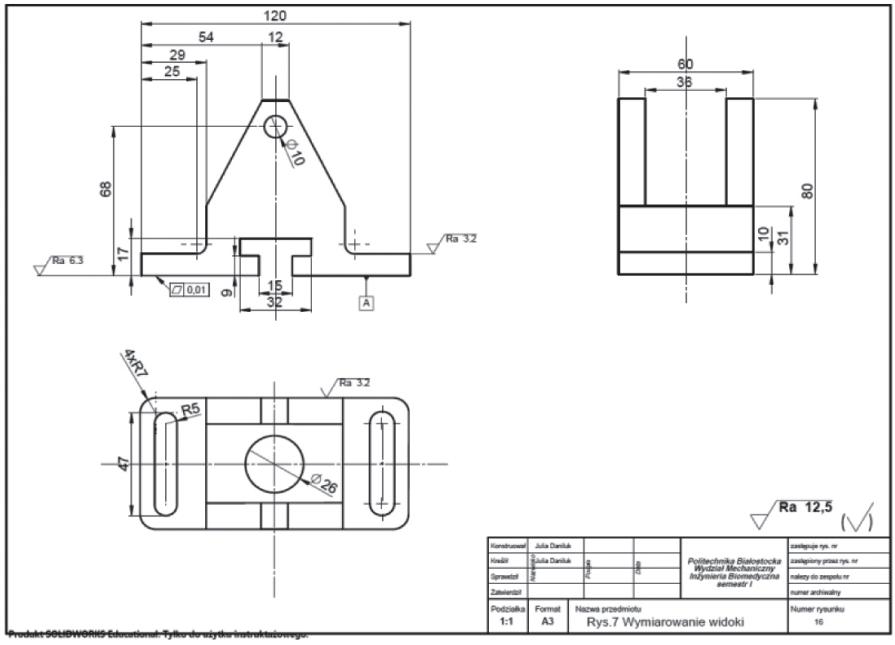

Fig. 2. 2D CAD-made drawing, three-view possibility part

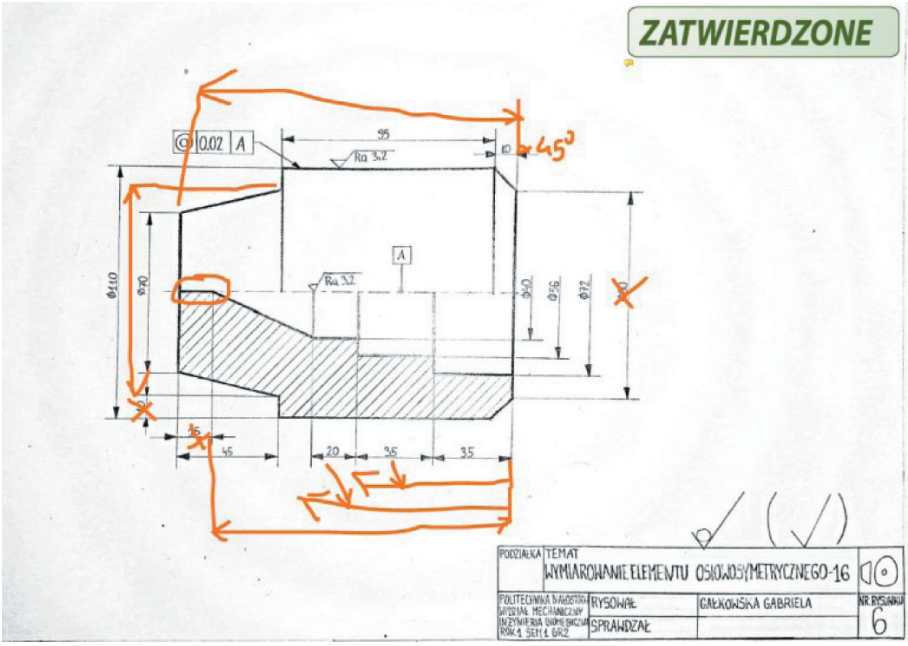

Fig. 3. Student's hand-drawn work (Fig. 1) with teacher's comment

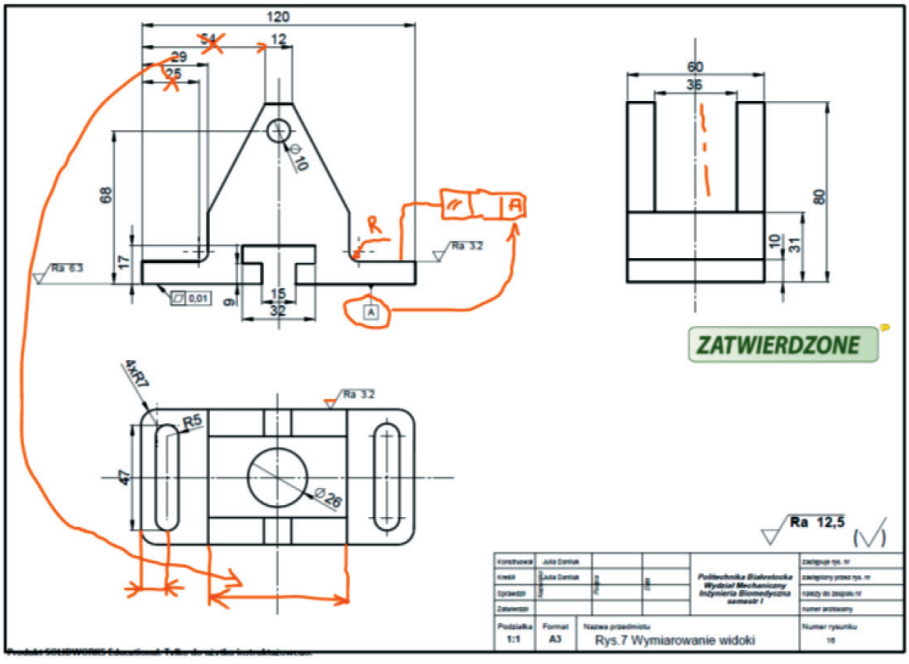

Fig. 4. Student's work using 2D CAD (Fig. 2) with teacher's comment

4. Conclusions

The following conclusions can be drawn from the presented work:

1) Technical drawing using 2D CAD is more legible and easier to correct.
2) The possibility of using many commercial and non-commercial CAD systems.
3) Saving 2D drawings in the form of generally available formats (e.g., pdf) is a standard in modern CAD systems.
4) Information exchange via Internet communication tools (e.g., Teams) is much easier with 2D CAD drawings.
5) Easy migration for students to 3D CAD systems.

Acknowledgments and Funding

This research was founded through a subsidy of the Ministry of Science and Higher Education of Poland for the discipline of mechanical engineering at the Faculty of Mechanical Engineering, Bialystok University of Technology WZ/WM-IIM/4/2020.

REFERENCES

Bajkowski J., 2011, *Podstawy zapisu konstrukcji*, Oficyna Wydawnicza Politechniki Warszawskiej, Warszawa.

Bajkowski J., Bajkowski J.M., 2019, *Podstawy zapisu konstrukcji. Materiały do ćwiczeń projektowych. Zadania z rozwiązaniami*, Wydawnictwo Naukowe PWN, Warszawa.

Bortnikova V., Yevsieiev V., Maksymova S., Nevliudov I., Chala O., Kolesnyk K., 2019, *Mathematical model of equivalent stress value dependence from displacement of RF MEMS membrane*, 15th International Conference on Perspective Technologies and Methods in MEMS Design (MEMSTECH). Proceedings, 83–86.

Dankwort C.W., Weidlich R., Guenther B., Blaurock J.E., 2004, *Engineers' CAx education – it's not only CAD*, Computer-Aided Design, 36(14), 1439–1450.

González-Lluch C., Plumed R., Pérez-López D., Company P., Contero M., Camba J.D., 2021, *A constraint redundancy elimination strategy to improve design reuse in parametric modelling*, Computers in Industry, 129, 103460.

Havrylenko Y., Cortez J.I., Kholodniak Y., Alieksieieva H., Garcia G.T., 2020, *Modelling of surfaces of engineering products on the basis of array of points*, Tehnički vjesnik, 27(6), 2034–2043.

Jabłoński M., Łukaszewicz A., 2013, *Approaches to assemblies modelling in MCAD systems*, Proceedings of XXI Polish-Ukrainian Conference on: CAD in Machinery Design. Implementation and Educational Issues, 15–16.

Jabłoński M., Panas K., Łukaszewicz A., 2013, *Koncepcyjne projekty urządzeń wykonane przy użyciu oprogramowania 3D CAD*. In: Mikołajczyk T. (red.), *Komputerowe wspomaganie nauki i techniki CAx*, T. 1, Uniwersytet Techniczno-Przyrodniczy, Bydgoszcz, 43–52.

Kok P.J., Bayaga A., 2019, *Enhancing graphic communication and design student teachers' spatial visualisation skills through 3D solid computer modelling*, African Journal of Research in Mathematics, Science and Technology Education, 23(1), 52–63.

Kolesnyk K., Panchak R., Pylypenko V., Abliazizov I., Fedosyeyev O., Ferens R., 2017, *Managing robot kinematics based on Arduino controllers using a unity system*, 13th International Conference on Perspective Technologies and Methods in MEMS Design (MEMSTECH). Proceedings, 44–46.

Łukaszewicz A., 2006, *Rola i rozwój współczesnych systemów CAD*, V Konferencja naukowo-praktyczna „Energia w Nauce i Technice", Suwałki, 95–98.

Łukaszewicz A., 2008a, *CAx education as an inseparable part of integrated product development*. In: Rochatyński R. (Ed.), *Design methods for industrial practice*, Oficyna Wydawnicza Uniwersytetu Zielonogórskiego, Zielona Góra, 313–320.

Łukaszewicz A., 2008b, *Selected aspects of parametric CAD systems education*, Proceedings of XVI Ukrainian-Polish Conference on: CAD in Machinery Design. Implementation and Educational Issues, 42–44.

Łukaszewicz A., 2009a, *General advices to the CAx education directed for needs of the industry*. In: Józwik J. (Ed.), *Advanced technologies in production engineering*, Societas Scientiarum Lublinensis, Lublin, 73–86.

Łukaszewicz A., 2009b, *General rules of parts and assemblies modelling in parametric CAD systems*, Machine Dynamics Problems, 33(3), 49–55.

Łukaszewicz A., 2009c, *Selected problems of CAD education directed for industrial practice*, Scientific Gerald of Lviv Polytechnic National University, 651, 225–231.

Łukaszewicz A., 2010a, *SolidWorks based CAx Education Directed for Industrial Practice*, SolidWorks World 2010, Anaheim, USA, 23.

Łukaszewicz A., 2010b, *Zagadnienia wdrażania parametrycznych systemów CAx w sektorze przemysłowym branży mechanicznej*, Mechanik, 1, 142–146.

Łukaszewicz A., 2011, *Sources of innovative UAV design*, Proceedings of XIX Polish-Ukrainian Conference on: CAD in Machinery Design. Implementation and Educational Issues, 27–28.

Łukaszewicz A., 2014, *Approach to understanding of design process at parametric, history-based CAD systems*, Proceedings of XXII Ukrainian-Polish Conference on: CAD in Machinery Design. Implementation and Educational Issues, 186–187.

Łukaszewicz A., Kernytskyy A., 2011, *Rapid prototyping in UAV applications on the example of 3D printing technique*, Proceedings of XIX Polish-Ukrainian Conference on: CAD in Machinery Design. Implementation and Educational Issues, 29–30.

Łukaszewicz A., Kernytskyy A., 2012, *CAx System as an education platform in mechanical branch*, Proceedings of XX Ukrainian-Polish Conference on: CAD in Machinery Design. Implementation and Educational Issues, 31–33.

Łukaszewicz A., Panas K., Szczebiot R., 2018a, *Design process of technological line to vegetables packaging using CAx tools*, Proceedings of 17th International Scientific Conference on: Engineering for Rural Development, 871–876.

Łukaszewicz A., Skorulski G., Szczebiot R., 2018b, *The main aspects of training in the field of computer-aided techniques (CAx) in mechanical engineering*, Proceedings of 17th International Scientific Conference on: Engineering for Rural Development, 865–870.

Łukaszewicz A., Trochimczuk R., Melnyk M., Kernytskyy A., 2021, *Design of mechatronics systems using CAx environment*. In: Butryło B. (Ed.), *Methods and Tools in CAD – Selected Issues*, Oficyna Wydawnicza Politechniki Białostockiej, Białystok, 7–14.

Madsen D.A., Madsen D.P., 2016, *Engineering drawing and design*, Cengage Learning.

Melnyk M., Kernytskyy A., Lobur M., Szermer M., Zajac P., Maj C., Zabierowski W., 2015, *Custom method for automation of microbolometer design and simulation*, Proceedings of the 22nd IEEE International Conference: Mixed Design of Integrated Circuits and Systems (MIXDES), 301–304.

Mircheski I., Łukaszewicz A., Szczebiot R., 2019, *Injection process design for manufacturing of bicycle plastic bottle holder using CAx tools*, Procedia Manufacturing, 32, 68–73.

Morling K., 2010, *Geometric and engineering drawing*, 3rd Edition, Elsevier.

Panas K., Łukaszewicz A., 2013, *Effective work in design of new product in MCAD systems*, Proceedings of XXI Polish-Ukrainian Conference on: CAD in Machinery Design. Implementation and Educational Issues, 43–44.

Ramos B., Melgosa C., 2020, *CAD learning in mechanical engineering at universities*, Computer-Aided Design and Applications, 18(1), 24–41.

Sidun P., Łukaszewicz A., 2017, *Verification of ram-press pipe bending process using elasto-plastic FEM model*, Acta Mechanica et Automatica, 11(1), 47–52.

Zdobytskyi A., Lobur M., Panchak R., Sika R., Kalinowski K., 2021, *Increasing the strength of materials by topological optimization methods*, Proceedings of 16th International Conference on the Experience of Designing and Application of CAD Systems, 6–9.

Concept of using unmanned aerial vehicles to locate pollution in industrial area

Dawid Nowicki ORCID ID: 0000-0002-9118-1518

AGH University of Science and Technology
Faculty of Mechanical Engineering and Robotics
Department of Power Systems and Environmental Protection Facilities, Krakow
email: dnowicki@agh.edu.pl

Katarzyna Suder-Dębska ORCID ID: 0000-0003-1945-6799

AGH University of Science and Technology
Faculty of Mechanical Engineering and Robotics
Department of Power Systems and Environmental Protection Facilities, Krakow
email: suder@agh.edu.pl

Ireneusz Czajka ORCID ID: 0000-0003-0013-8467

AGH University of Science and Technology
Faculty of Mechanical Engineering and Robotics
Department of Power Systems and Environmental Protection Facilities, Krakow
email: iczajka@agh.edu.pl

ABSTRACT

More and more attention is being paid to the impact of industry on the environment and people's surroundings. One type of pollution is the noise that is generated by technological apparatus. It is necessary to develop new tools that will be able to survey noise in large industrial areas. This paper presents a concept of using unmanned aerial vehicles to generate acoustic maps of a surveyed area. One of the tools that is required for this purpose is aerial photogrammetry, which is used to generate a numerical terrain model from a series of photographs. The methodology and results of the simulation study of the effect of the data-acquisition-process parameters (flight altitude and transverse and longitudinal overlay levels of images) on the quality of the generated numerical terrain model and the generating time are presented in this paper.

Keywords: UAV, pollution, photogrammetry, environmental protection, OpenDroneMap, noise

1. Introduction

In addition to the benefits it brings, human technical activity is also a source of many types of pollution. One type of pollution is the noise that is emitted as a result of human industrial activity (Gołaś et al. 2013). Increasing attention is being paid to the impact of noise on the environment and humans. In order to counteract noise pollution, it is necessary to know the locations and sound power values of any potential noise sources. In large urban areas, the monitoring of the sound power of multiple sound sources can be difficult to ascertain with traditional methods. It seems reasonable to develop alternative tools that are capable of localizing noise sources and estimating their acoustic power (Gołaś et al. 2015).

2. Unmanned aerial vehicles in area surveys

Industrial sites cover large areas, so their noise sources are difficult to localize. One of the modern remote tools for field investigations is an unmanned aerial vehicle (Nex, Remondino 2014). Its detection capabilities depend on the type of apparatus with which it is equipped (Fig. 1).

By using a microphone array, it is possible to localize sound sources (Martinez-Carranza, Rascon 2020). Acoustic waves that are generated by sources that are located on the surface of the ground reach the microphones at different times; based on the differences in the times of arrival of the sound at the given receivers, it is possible to determine the localizations of where the sources are located (Ohata et al. 2017; Yamada et al. 2020). By using a camera that takes aerial photographs of an area, it is

possible to reconstruct a numerical terrain model from the collected set of images (Liu et al. 2018). Using both channels of information (sound and image) would allow us to develop a tool for generating acoustic maps (Iannotti et al. 2016) of a studied area.

Fig. 1. Possibility of using peripherals in unmanned aerial vehicles

3. Photogrammetry

To create a map and a numerical terrain model using a series of photographs, it is necessary to use photogrammetry techniques. This is a field in which reliable information on the surface shapes of objects is obtained only from the series of photos in which the object is present (Al-Qadri, Cheng 2020). The parameters of the data-acquisition process have a significant impact on the process and the results of the image processing (Mokrane et al. 2019). A simulation study of the effects of data-acquisition parameters

such as flight altitude and the longitudinal and transverse overlap levels of images on the quality of a generated numerical model was conducted, along with the time that is required to generate it.

4. Methodology

Due to the cost of conducting field tests for a number of changing input parameters, it was decided to carry out tests based on a computer simulation. The scheme of the experiment to be carried out is shown in Figure 2, and the simulation environment consisted of an input numerical terrain model. At specific positions above the terrain, photographs were taken. Control points, which were needed for the model's quality evaluation (Casella et al. 2020), were inserted into the input numerical terrain model. Then, for the assumed parameters of the data-acquisition process, photographs of the model were realized; based on these, an output numerical terrain model was generated. Access to both models allows for the reproduction error to be determined by the control point measurements.

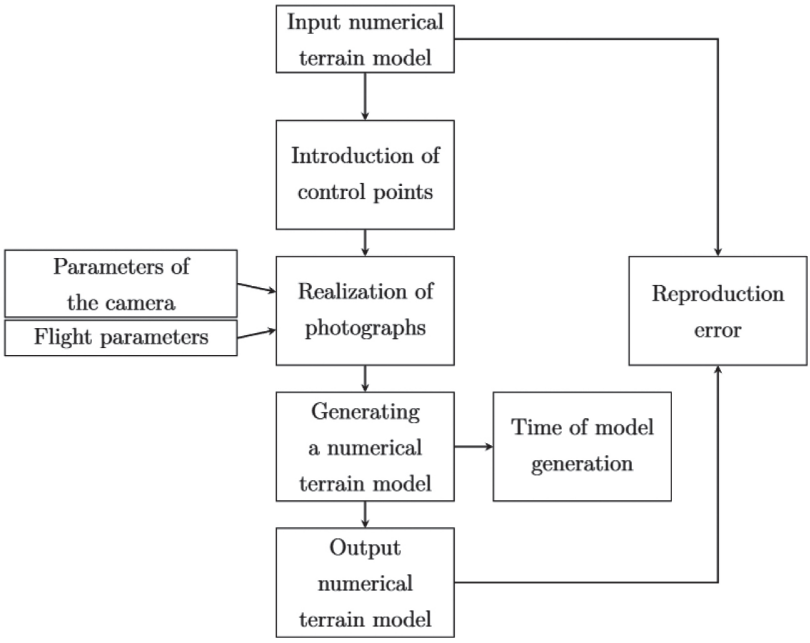

Fig. 2. Scheme of experiment

Figure 3 shows an input terrain model of about 330 m × 180 m. This represents a low-urbanized terrain with a maximum elevation of several meters. Two types of

points were placed on the surface of the model: a main point (which was used to set up the measured coordinate system), and 12 control points (Fig. 4) (which were used to determine the reproduction error).

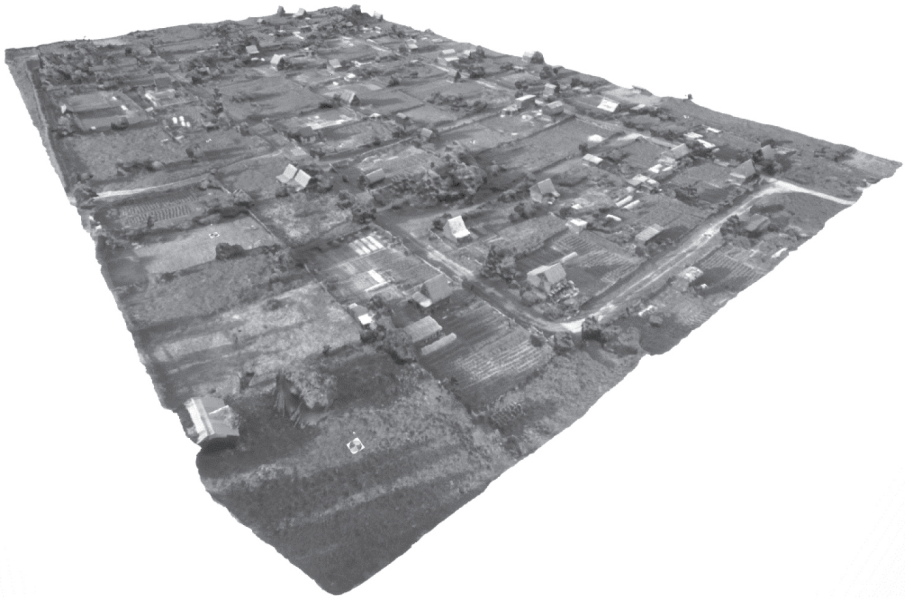

Fig. 3. View of input numerical terrain model

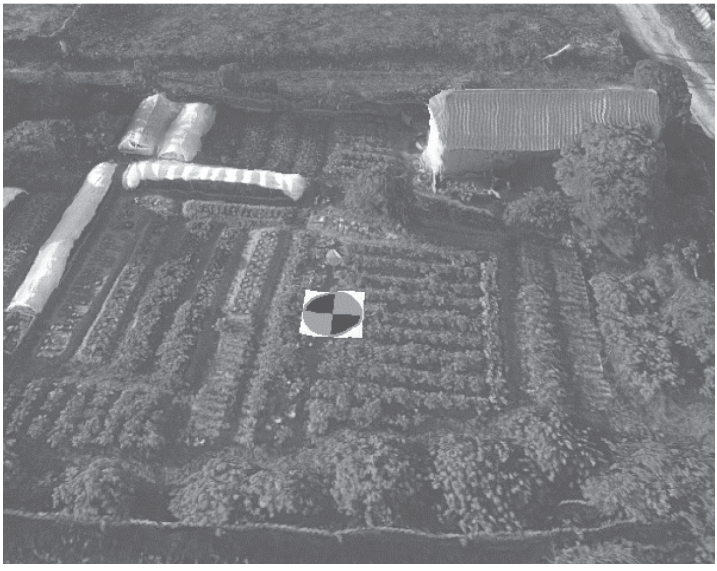

Fig. 4. View of checkpoint

The range of the changes in the input parameters of the conducted experiment was between a 65 and 95% overlap of the images in both directions, and the range of the altitude was between 90 and 130 m above the surface. Figure 5 shows the localization of the control points. The main point was placed in the center of the study area. The localizations of the control points were chosen randomly.

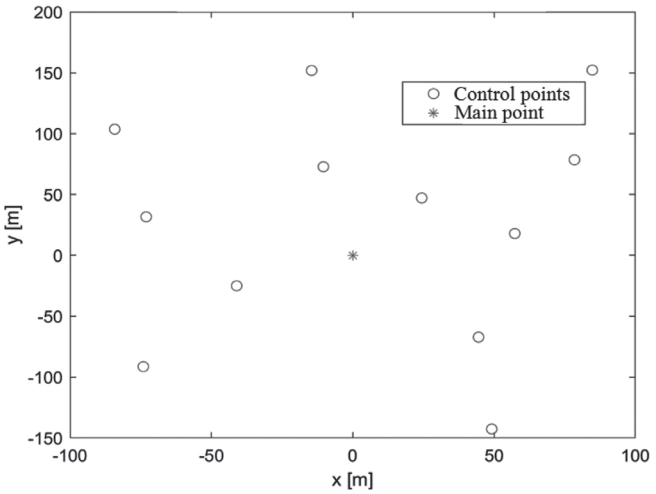

Fig. 5. Localizations of control points

5. Results and conclusions

The numerical experiment consisted of 32 simulations. Each series of photographs was processed in OpenDroneMap photogrammetric software. For each numerical terrain model that was generated, the image-processing parameters were the same. Figure 6 graphically shows the relationship between the time that was required to generate a numerical terrain model at a given point in the experiment and the number of images that were taken in a given series. The experimental data was approximated by a quadratic function with a fit factor of 96%.

Figure 7 presents the response surfaces after being fitted to the experimental data. These show the dependence of the number of images depending on the levels of the overlap. It can be seen that, within a range of 65 to 85%, there was a low increase in the number of photos; however, the increase was much more rapid for the range above 85%. Reducing the flight altitude from 130 to 90 m resulted in a doubling of the number of photos that needed; this simply translated into a significant increase in the time that was needed to generate a numerical terrain model. To determine the representation error, a coordinate system was set in the output models at the main point (relative to which the positions of the control points were measured). The box plots (Fig. 8) show

the relative vertical reproduction error. It can be seen that the medians of the errors were not at zero. To eliminate the influence of the systematic error that was associated with the translation of the models to a common coordinate system from the evaluation, an analysis of the error distribution was carried out. A chi-square test for fit to the normal distribution was performed for the errors from each axis. The normal distributions were then fitted, and a percentile of 97.5 was evaluated. The absolute error was then assembled geometrically from the errors.

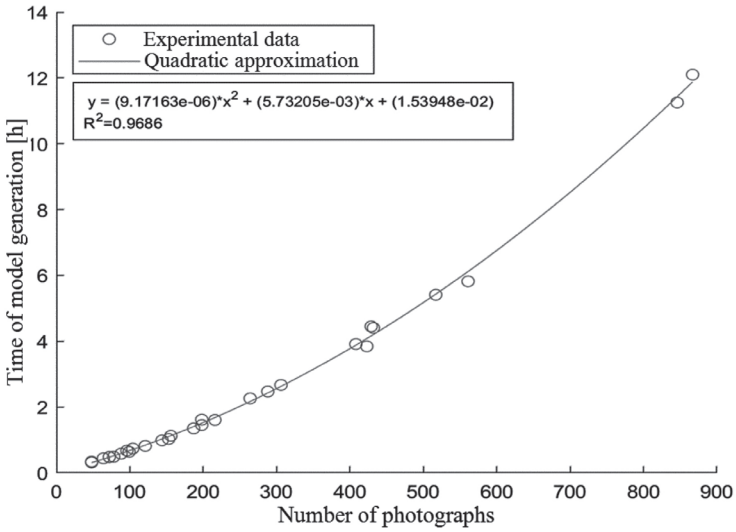

Fig. 6. Relationship of numerical terrain model generating time to number of images

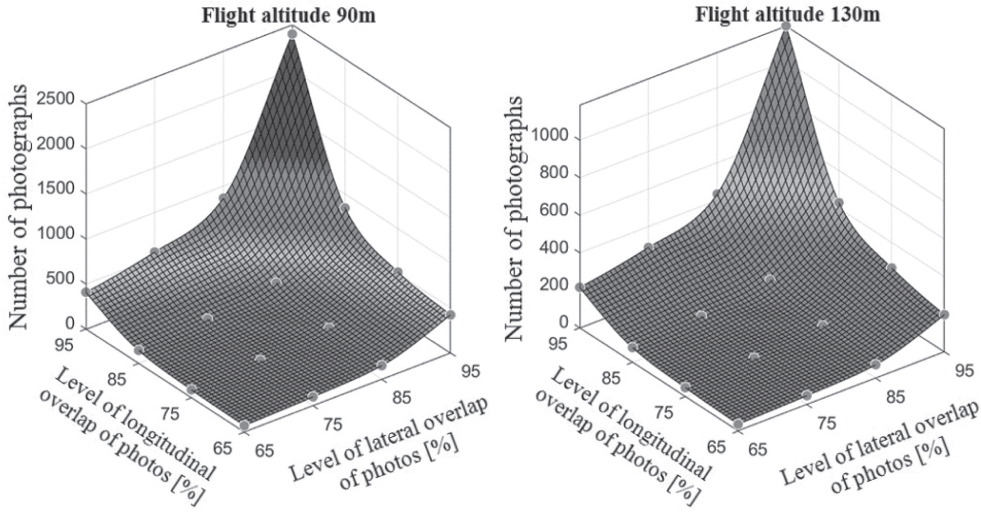

Fig. 7. Response plots for number of images depending on parameters of capturing them

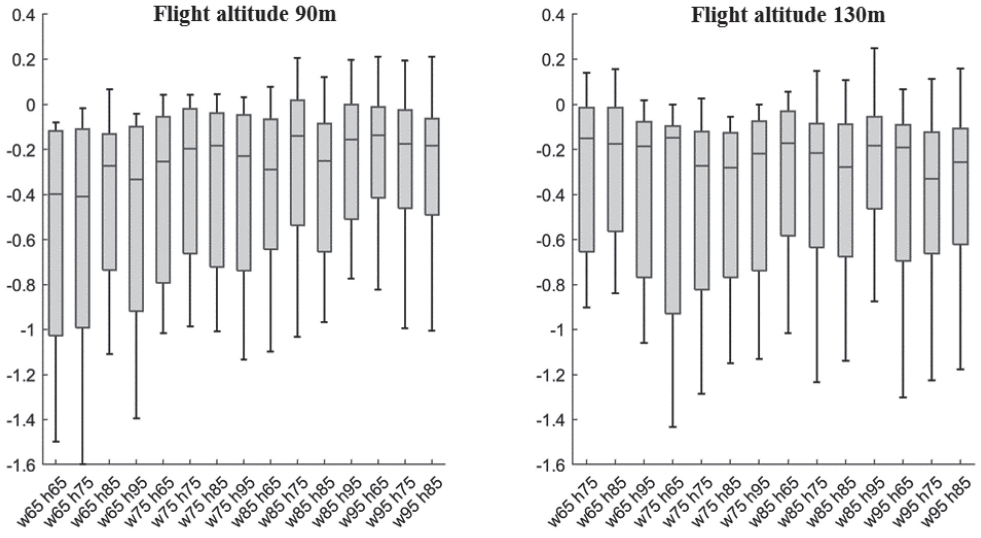

Fig. 8. Distribution of vertical representation errors for models in experiment

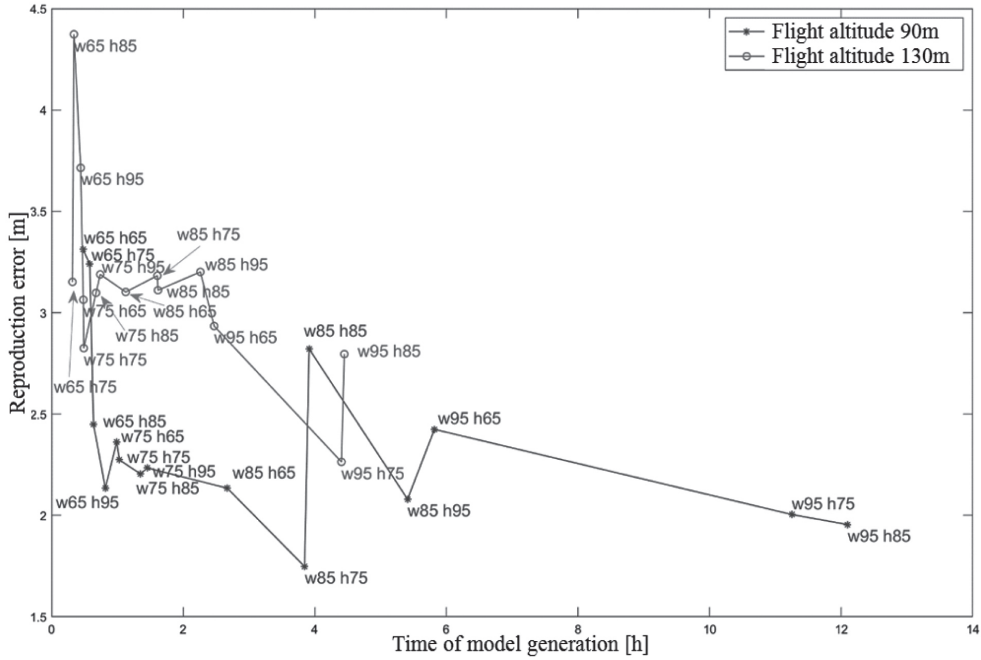

Fig. 9. Dependence of mapping accuracy on generation time of numerical terrain model

A graph that shows the results in the time-quality domain is included in Figure 9. In these results, the best in terms of quality was the model whose parameters were a flight altitude of 90 m and longitudinal and lateral overlap levels that were 85%

and 75%, respectively. It took four hours to generate this model, which was three times quicker than the longest time that was needed in the experiment to generate the numerical terrain model. Based on the results, it can be seen that reducing the flight altitude to 90 m resulted in a 45% increase in the mapping accuracy with a similar generation time (two hours).

6. Summary

Environmental protection is a field that is constantly evolving, and modern tools for localizing and identifying the sources of pollution are in demand. Unmanned aerial vehicles are modern measurement tools with a growing list of applications – one of which may be detecting sources of various types of pollution.

Work is underway to implement a microphone array for the unmanned aerial vehicles that are being developed. The ability to locate sound sources in conjunction with photogrammetry will make it possible to generate acoustic maps of an area under study; these are necessary for localizing sources of pollution such as noise or solid particle contamination.

REFERENCES

Al-Qadri M., Cheng J., 2020, *Study on using single UAV's image for extraction measurement of flat area*, E3S Web of Conferences, 165, 1–6.

Casella V., Chiabrando F., Franzini M., Manzino A., 2020, *Accuracy assessment of a UAVblock by different software packages, processing schemes and validation strategies*, ISPRS International Journal of Geo-Information, 9(3), 164.

Gołaś A., Suder-Dębska K., Czajka I., 2013, *Modelowanie rozkładu pola akustycznego wokół wiertni przy poszukiwaniu I eksploatacji gazu łupkowego*. In: Damijan Z., Wiciak J., Kasprzak C., XX Konferencja Inżynierii Akustycznej i Biomedycznej, Kraków – Zakopane, 15–19 kwietnia 2013, 67–68.

Gołaś A., Ciesielka W., Czajka I., Czechowski M., Filipek R., Suder-Dębska K., Śliwiński M., Wołoszyn J., Żywec W., Szopa K., 2015, *Mechanical engineering in smart grid technology*, Wydział Inżynierii Mechanicznej i Robotyki AGH, Kraków.

Iannotti A., Serpilli F., Secchiaroli A., Ricci R., 2016, *Acoustic analysis of wind turbine generators*, Euronoise 2016 Conference, Tampere, Finland.

Liu Y., Zheng X., Ai G., Zhang Y., Zuo Y., 2018, *Generating a high-precision true digital orthophoto map based on UAV images*, ISPRS International Journal of Geo-Information, 7(9), 333.

Martinez-Carranza J., Rascon C., 2020, *A review on auditory perception for unmanned aerial vehicles*, Sensors, 20(24), 7276.

Mokrane A., Choukchou-Braham A., Cherki B., 2019, *DEM generation based on UAV photogrammetry*, International Conference on Advanced Electrica Engineering (ICAEE).

Nex F., Remondino F., 2014, *UAV for 3D mapping applications: a review*, Applied Geomatics, 6(1), 1–15.

Ohata T., Nakamura K., Nagamine A., Mizumoto T., Ishizaki T., Kojima R., Sugiyama O., Nakadai K., 2017, *Outdoor sound source detection using a quadrocopter witch microphone array*, Journal of Robotics and Mechatronics, 29(1), 177–187.

Yamada T., Itoyama K., Nishida K., Nakadai K., 2020, *Sound source tracking using multiple microphone arrays mounted to an Unmanned Aerial Vehicle*, Sound Source Tracking by Drones with Microphone Arrays, 796–801.

Numerical analysis of cold extrusion of tubes using CAx system

Grzegorz Skorulski ORCID ID: 0000-0002-0022-7016

Bialystok University of Technology
Faculty of Mechanical Engineering
Department of Materials and Production Engineering, Bialystok
email: g.skorulski@pb.edu.pl

Andrzej Łukaszewicz ORCID ID: 0000-0003-0373-4803

Bialystok University of Technology
Faculty of Mechanical Engineering
Department of Machine Design and Exploitation, Bialystok
email: a.lukaszewicz@pb.edu.pl

ABSTRACT

This paper presents a numerical analysis of the cold extrusion of pipes with the use of DEFORM 3D software. As a result, a CAE system was obtained with the help of CAD, and diagrams of the effective stress distribution are presented. Additionally, some aspects of the quality of the final product were discussed.

Keywords: cold extrusion, tubes, friction, effective stress distribution

1. Introduction

CAx (CAD/CAM/CAE) tools are widely used in engineering fields (Łukaszewicz et al., 2018; Łukaszewicz et al. 2021). The main advantage of using CAx systems is the shortening of a product's time development. The ability to perform many types of CAE analyses (Mircheski et al. 2019; Sidun, Łukaszewicz 2017), visualizations, and technical documentations in the design phase allows us to better fit the assumptions.

Cold extrusion is defined as a compressive forming process (push-through) in which the source material is a billet (slug); the process is carried out at room temperature. The basics of cold-extrusion processes are described in Filice et al. (2008) and Stepanenko et al. (1987).

The design and manufacture of dies must be obtained by modern manufacturing methods from the appropriate die materials to ensure an acceptable die life at a reasonable cost (Dieter et al. 2003). Detailed knowledge about the process will help streamline die production processes (Hrycaj et al. 1991; Nine 1982; Oden, Pires 1983).

The friction factor μ in non-lubricated hot extrusion has a fixed value of $\mu = 1$. In lubricated hot extrusion, $0.1 \leq \mu \leq 0.4$, with an estimated average μ value of about 0.25 (Webster, Davis 1982).

Flow stress is a function of the temperature, strain, strain rate, and structure. Thus, a calculated flow stress value can be used for estimating the extrusion pressures for other extrusion ratios and shapes (Bhattacharyya et al. 1982). The possible loads are influenced by the different process variables (Dieter et al. 2003; Oden, Pires 1983) as well.

2. Die design in CAx systems

The objectives of applying CAE techniques to extrusion have been explained in several papers (Abou-El-Lail Mohsen, Farag Mahmound 1981; Bhattacharyya et al. 1982; Dieter et al. 2003; Hrycaj et al. 1991). The model of our die was created using the Deform 3D CAD/CAE system (Fig. 1).

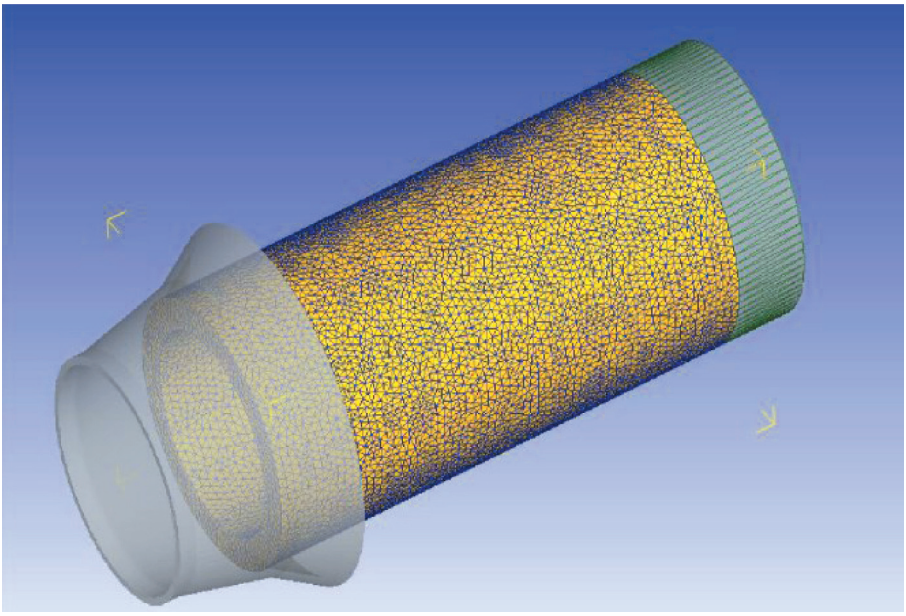

Fig. 1. Die, workpiece (tube), and punch designed in CAD/CAE system

The mesh of this model is available within this system. In the same way, the mesh of a workpiece (e.g., tube) was obtained in works (Abou-El-Lail Mohsen, Farag Mahmound 1981; Oden, Pires 1983).

3. Preparing simulation

Before commencing the simulation of the extrusion process, a number of conditions needed to be fulfilled. It was necessary to check whether all of the required files and dates were available (Altan et al. 2004; Samper, Felder 1990).

The model of the workpiece (i.e., tube) contained the following data:

- density: 7.8 e–09 kg/mm^3,
- Young's modulus: 2.1 e+05 MPa,
- Poisson ratio: 0.3,
- thickness: 4 mm.

The hardening curve of the tube material is described as a function of the stress and plastic strain:

$$\sigma_p = 976 \cdot (\varepsilon_p + 0.2)^{0.14} \tag{1}$$

The punch data was comprised of the following information:

- density: 7800 kg/m^3,
- Young's modulus: 2.1 e+05 MPa,
- Poisson ratio: 0.3,
- velocity of punch: 10 m/s.

The specified dimensions of the die and workpiece are presented in Figure 2.

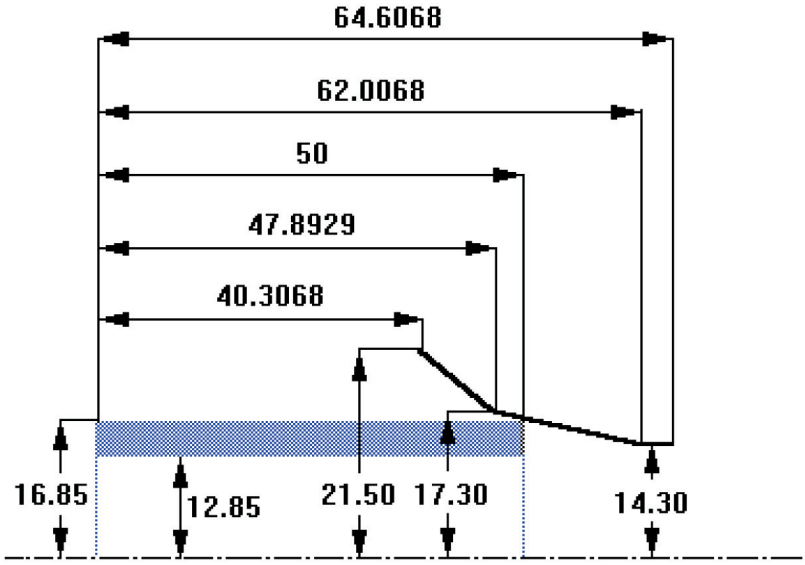

Fig. 2. Geometry of tool and workpiece

4. Discussion of results

The computer simulation of the tube extrusion considered three cases. There were three different friction coefficients that were used in each simulation: their values were as follows (Samper, Felder 1990): $\mu = 0.15$ (for example, uncoated steel); $\mu = 0.2$ (zinc-coated steel in metal forming); $\mu = 0.05$ (lubricated extrusion).

The numerical simulations in Figure 3 (initial state of extrusion), Figure 4 (advanced phase of extrusion), and Figure 5 (end of the process) are presented below.

The technical problem of the tube extrusion is almost always the final diameter of the product. It is possible to obtain these kinds of results from a numerical simulation; these are shown in Figure 6.

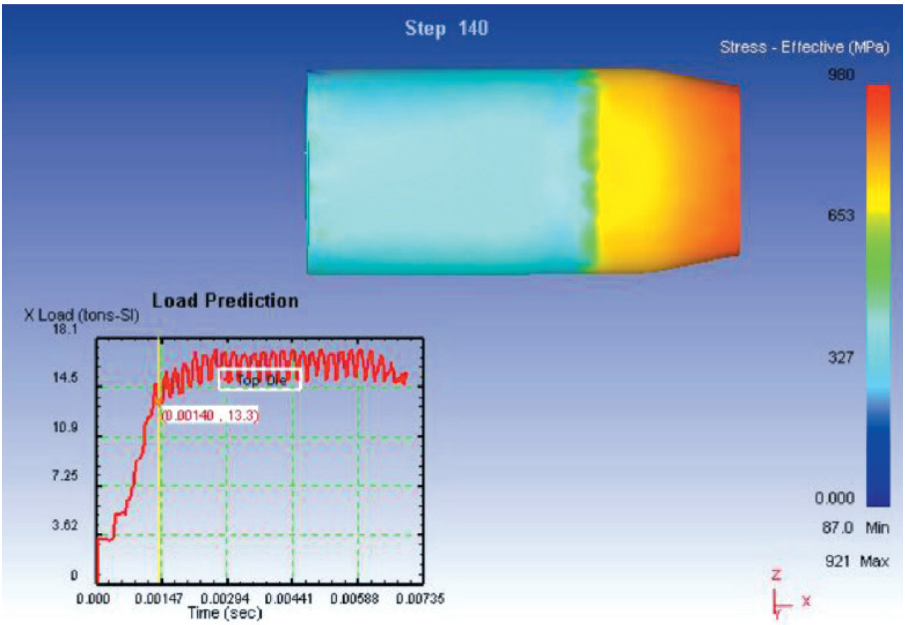

Fig. 3. Effective stress during cold tube extrusion – initial phase of process

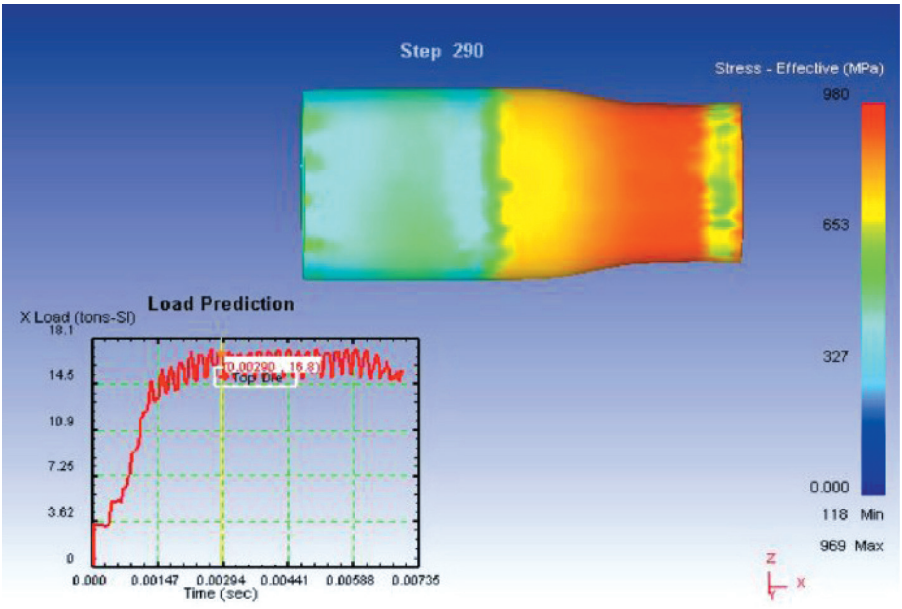

Fig. 4. Effective stress during cold tube extrusion – advanced phase of process

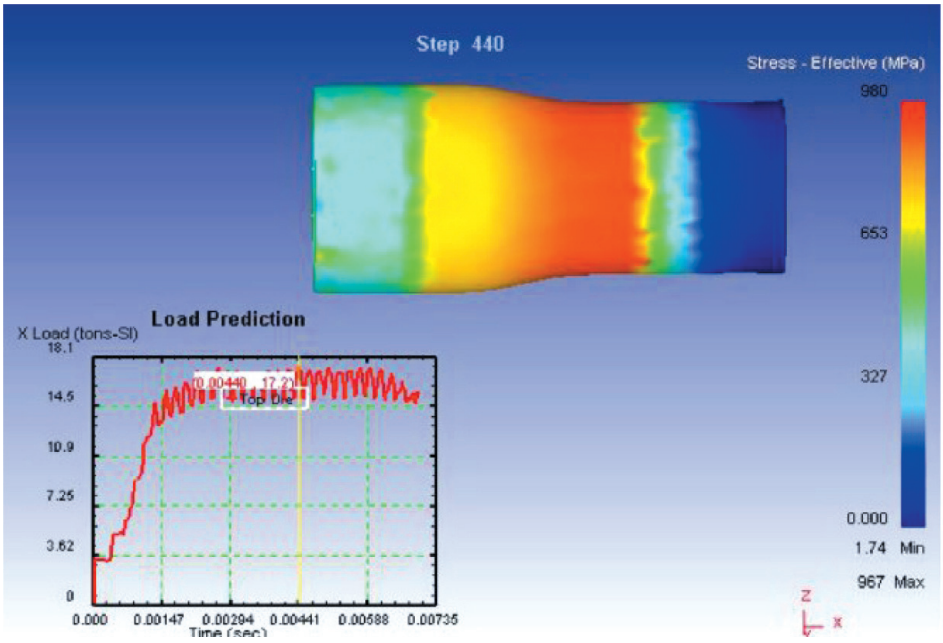

Fig. 5. Effective stress during cold tube extrusion – end of process

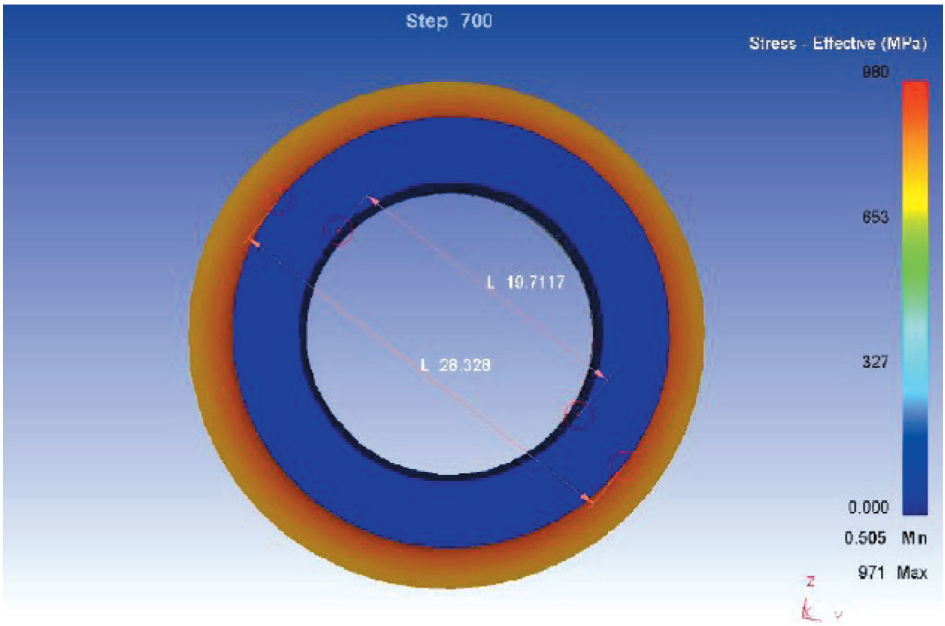

Fig. 6. Final diameters of extruded tube

5. Concluding remarks

It is a very short duration time of cold tube extrusion; therefore, numerical methods are almost the only means of obtaining the solution of pressure distribution on a die's surface. It seems necessary to know the value of the friction coefficients during the extrusion process and their distribution. The friction coefficient ranged from 0.05 to 0.15 in the presented simulation.

On the other hand, it seems to be impossible to obtain the results of contact stresses by using the DFORM 3D system only (with all of its functional constraints). The unknown distribution of stresses that is described above does not allow for die design; only the load and effective stress for choosing the technological parameters of the process are available. Some type of result is disabled because the material of the tool is defined as a rigid body of necessity; thus, only the solution that is described above has been worked out. The test was made using the Deform 3D system. During the test, a friction coefficient of $\mu = 0.12$ was assumed as a recommended parameter for the extrusion of steel tubes. The results of effective stress (Figs. 3–5) also showed the possible load of the punch. The max value of this result (X Load) was near 18 e+3 kg. Thus, this is preliminary approximate information about the kind of press that should be used. Additionally, the computer simulation allowed us to check the possible inner and outer diameters of the extruded tube. This is shown in Figure 6.

So, the computer simulation of the described extrusion process may be very useful for defining the precision load of a die. Using even similar theoretical or experimental methods to obtain this data may be more complex. The pressure load from a computer simulation to calculate the contact stress distribution may be obtained as well. The results of a numerical analysis are, thus, of great importance, as they make it possible to (approximately) estimate the die's load. Even though the actual extrusion process is accomplished within a split second, the setting up of a workplace that is equipped with all of the required measurement sensors to register the die load poses a very complicated problem and often requires significant outlays.

Acknowledgments

This research was founded through a subsidy of the Ministry of Science and Higher Education of Poland for the discipline of mechanical engineering at the Faculty of Mechanical Engineering, Bialystok University of Technology WZ/WM-IIM/4/2020.

REFERENCES

Abou-El-Lail Mohsen M.M., Farag Mahmound M., 1981, *Analysis of direct extrusion by the finite element technique*. In: Metwalli S.M. (Ed.), *Current Advances in Mechanical Design and Production: Proceedings of the 1st International Conference, Cairo University, Egypt, 27–29 December 1979*, Pergamon Press, Oxford, 239–246.

Altan T., Ngaile G., Shen G., 2004, *Cold and Hot Forging. Fundamentals and Applications*, ASM International, Materials Park, OH.

Bhattacharyya S., Mujamdar A.K., Basu S.K., 1982, *Mathematical modelling of metal extrusion process*, Journal of Engineering for Industry, 104(1), 65–70.

Dieter E.G., Kuhn H.A., Semiatin S.L., 2003, *Handbook of Workability and Process Design*, ASM Internationalm Materials Park, OH.

Filice L., Gagliardi F., Micari F., 2008, *A laboratory scale equipment to relieve force and pressure in cold extrusion of lead hollow components*, Key Engineering Materials, 367, 137–144.

Hrycaj P., Cescotto S., Oudin J., 1991, *Elasto-plastic finite element analysis of unilateral contact with generalised Coulomb friction*, Engineering Computation, 8(4), 291–303.

Łukaszewicz A., Skorulski G., Szczebiot R., 2018, *The main aspects of training in the field of computer-aided techniques (CAx) in mechanical engineering*, Proceedings of 17th International Scientific Conference on: Engineering for Rural Development, May 23–25, 2018, 865–870.

Łukaszewicz A., Trochimczuk R., Melnyk M., Kernytskyy A., 2021, *Design of mechatronics systems using CAx environment*. In: Butryło B. (Ed.), *Methods and Tools in CAD – Selected Issues*, Oficyna Wydawnicza Politechniki Białostockiej, Białystok, 7–14.

Mircheski I., Łukaszewicz A., Szczebiot R., 2019, *Injection process design for manufacturing of bicycle plastic bottle holder using CAx tools*, Procedia Manufacturing, 32, 68–73.

Nine H.D., 1982, *The applicability of Coulomb's friction law to drawbeads in sheet metal forming*, Journal of Applied Metalworking, 2(3), 200–210.

Oden J.T., Pires E.A., 1983, *Numerical analysis of certain contact problems in elasticity with non-classical friction laws*, Computers & Structures, 16(1–4), 481–485.

Samper V., Felder E., 1990, *Frictional mechanism in uncoated and zinc-coated steel sheet forming – theoretical and experimental results*, Tribology Series: Mechanics and Coatings, 17, 271–279.

Sidun P., Łukaszewicz A., 2017, *Verification of ram-press pipe bending process using elasto-plastic FEM model*, Acta Mechanica et Automatica, 11(1), 47–52.

Stepanenko A.V., Isaevich L.A., Veremeichik A.A., Medvedeva T.A., 1987, *Theoretical investigation of the process of cold extrusion of rods from unplasticized metal powders. III. Extrusion pressure*, Powder Metallurgy and Metal Ceramics, 26(7), 519–523.

Webster W.D., Davis R.L., 1982, *Development of a friction element for metal forming analysis*, Journal of Engineering for Industry, 104(3), 253–256.

Probabilistic modeling of mechanical cantilever oscillator fluctuation

Petro Kosobutskyy ORCID ID: 0000-0002-3975-4649

Lviv Polytechnic National University
Institute of Computer Science and Information Technologies
Department of Computer-Aided Design Systems, Lviv
email: petro.s.kosobutskyi@lpnu.ua

Andriy Zdobytskyi ORCID ID: 0000-0001-8044-9593

Lviv Polytechnic National University
Institute of Computer Science and Information Technologies
Department of Computer-Aided Design Systems, Lviv
email: andrii.y.zdobytskyi@lpnu.ua

Uliana Marikutsa ORCID ID: 0000-0002-9514-7413

Lviv Polytechnic National University
Institute of Computer Science and Information Technologies
Department of Computer-Aided Design Systems, Lviv
email: uliana.b.marikutsa@lpnu.ua

Mykhaylo Melnyk ORCID ID: 0000-0002-8593-8799

Lviv Polytechnic National University
Institute of Computer Science and Information Technologies
Department of Computer-Aided Design Systems, Lviv
email: mykhaylo.r.melnyk@lpnu.ua

Marek Iwaniec ORCID ID: 0000-0002-1224-4753

AGH University of Science and Technology
Faculty of Electrical Engineering, Automatics, Computer Science and Biomedical Engineering
Department of Biocybernetics and Biomedical Engineering, Krakow
email: iwaniec@agh.edu.pl

ABSTRACT

The dynamics of oscillations of cantilever-type oscillators have been studied in this work. The probabilistic model of a cantilever is explained. Dependencies for the probability density, mean mathematical expectation, and standard deviation were developed. A fluctuation model of a cantilever was constructed, and the dependencies for the probability density for a direct problem were developed. The modeling of the mathematical expectation and phase variance for the inverse problem was performed.

Keywords: oscillator, atomic force microscope, probability density, mathematical expectation, variance

1. Introduction

Mechanical oscillators of the cantilever type in the form of a microconsole with one free end have become widely used due to their high quality factor. Their use has greatly simplified the practical implementation of atomic force microscopy and significantly increased the sensitivity of analyzers in biosensors (Voigtländer 2015); also, the small value of the inertial mass of the cantilever allows us to significantly increase the resonant frequency of sensor fluctuation (Battiston et al. 2001).

Despite the fact that many works have been devoted to studying the dynamics of cantilever oscillations systems, the corresponding task remains relevant in the future (Pietrzakowski 2002; Romaszko et al. 2015). Sensor probes are exposed to random external actions, so the measured parameters require statistical and probabilistic averaging. So far, this problem has barely been solved or has been solved for partial cases (Haran Dr. n.d.; Zibenko, Tarasevich 2016).

2. Substantiation of probabilistic cantilever model

Let us omit the details of the substantiation of the cantilever oscillation dynamics under a force that is applied to the free end (Fig. 1) (Berman, Chumak 2007).

To reveal the main essence of the work, we assume that the unfixed end of a cantilever fluctuates as a system with concentrated parameters – inertia is expressed by the value of oscillator mass m, and elasticity is a parameter of rigidity μ.

We assume that integral probability $dF(t \le \mathrm{T} \le t+dt) = f(t)dt$ is proportional to the width of interval dt: $dF = \kappa \cdot dt$, where constant coefficient κ can be determined from rationing condition $\int_0^{2\pi/\omega_0} f(t)dt = \kappa \int_0^{2\pi/\omega_0} dt = 1$, whence $\kappa = \omega_0/2\pi$. Therefore, the probability density function will be $f(t) = 2\omega_0/\pi$.

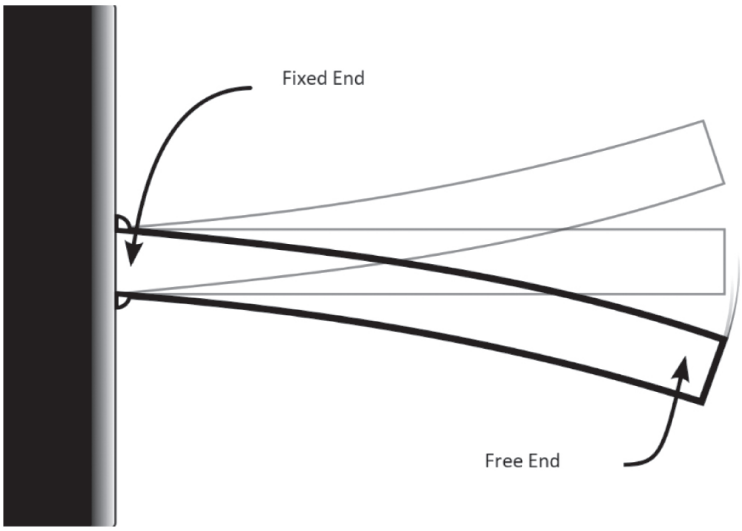

Fig. 1. Cantilever scheme

This means that random variable is evenly distributed. Its probability in interval $[t_1, t_2]$ is $F(t_1 \le \mathrm{T} \le t_2) = \int_{t_1}^{t_2} f(t)dt = F(t_2) - F(t_1) = \omega_0/2\pi \cdot (t_2 - t_1)$. The average $\overline{T}$ for period $2\pi/\omega_0$ is:

$$\overline{T} = \int_{-\infty}^{\infty} t \cdot f_T(t) \cdot dt = \frac{\omega_0}{2\pi} \int_0^{2\pi/\omega_0} tdt = \frac{\omega_0}{4\pi} \left(\frac{2\pi}{\omega_0} \right)^2 = \frac{\pi}{\omega_0}$$

and the mean $\overline{T^2}$ of the square is:

$$\overline{T^2} = \int_{-\infty}^{\infty} t^2 \cdot f_T(t) \cdot dt = \frac{\omega_0}{2\pi} \int_0^{2\pi/\omega_0} t^2 \cdot dt = \frac{\omega_0}{6\pi} \left(\frac{2\pi}{\omega_0} \right)^3 = \frac{1}{3} \left(\frac{2\pi}{\omega_0} \right)^2$$

Then, the variance of the random variable is:

$$D_T = \overline{T^2} - \left(\overline{T}\right)^2 = \frac{1}{3} \left(\frac{2\pi}{\omega_0} \right)^2 - \frac{1}{4} \left(\frac{2\pi}{\omega_0} \right)^2 = \frac{1}{12} \left(\frac{2\pi}{\omega_0} \right)^2 = \frac{1}{3} \left(\frac{\pi}{\omega_0} \right)^2 > 0 \quad (1)$$

and its standard deviation is:

$$\sigma_T = \frac{1}{\sqrt{3}} \frac{\pi}{\omega_0} \quad (2)$$

that is, the condition of non-dispersion is satisfied.

Under initial conditions $y|_{t=0} = 0$, the change in amplitude in a single period is described by function:

$$y = y_0 \cos \omega_0 t \tag{3}$$

Possible values of transformed random variation $Y = y_0 \cos \omega_0 T$ are placed in interval $Y \in [-y_0, y_0]$, beyond which probability density $f_Y(y) = 0$. This interval of Equation (3) has two roots.

To justify the probability density $f_Y(y)$ for values $Y \in [-y_0, y_0]$, let us set the explicit form of Inverse Function (3):

$$t = \frac{1}{\omega_0} \cos^{-1} \frac{y}{y_0}$$

and a derivation of the inverse:

$$\frac{d}{dy} \cos^{-1} y = -\frac{1}{\pi \sqrt{y_0^2 - y^2}} \tag{4}$$

Function $y = g(y) = y_0 \cos \omega_0 t$ is non-monotonic for both the original and converted random variable, and the connection of cumulative probabilities is true:

$$\begin{aligned} F_Y(y) &= \mathrm{P}[Y \le y] = \mathrm{P}[y_0 \cos \omega_0 t \le y] = \\ &= \mathrm{P}\left[\cos^{-1} \frac{y}{y_0} \le 2\pi - \cos^{-1} \frac{y}{y_0} \right] = 1 - \frac{1}{\pi} \cos^{-1} \frac{y}{y_0} \end{aligned} \tag{5}$$

where the derivative of (4) gives probability density $f_Y(y)$:

$$f_Y(y) = \frac{d}{dy} F_Y(y) = \frac{d}{dy} \left(1 - \frac{1}{\pi} \cos^{-1} \frac{y}{y_0} \right) = \frac{1}{\pi \sqrt{y_0^2 - y^2}} \tag{6}$$

The graph of Function (6) goes to infinity at $y \to \pm y_0$ due to the slowdown of function $y = \cos \omega_0 t$ in the vicinity of extreme points $\omega_0 t \to 0, \pi$. Dependence (6) is due to the fact that, under a relatively large sample size (the number of measurements) where value t from interval $2\pi/\omega_0$ is randomly selecting each time, size $\cos \omega_0 t$ more likely to take a value that is closer to ±1 than it is to zero (Consortini 2000).

In absolute value, the amplitude varies in interval $[0, y_0]$. Therefore, the average $\overline{Y}$ (mathematical expectation) is:

$$\overline{Y} = \int_{-\infty}^{\infty} y \cdot f_Y(y) \cdot dy = \frac{1}{\pi} \int_0^{y_0} \frac{y}{\sqrt{y_0^2 - y^2}} dy = \frac{1}{\pi} \int_0^{y_0} \frac{d(y_0{}^2 - y^2)}{\sqrt{y_0{}^2 - y^2}} = -\frac{1}{\pi} \sqrt{y_0^2 - y^2} \Big|_0^{y_0} = \frac{y_0}{\pi}$$

and the mean square (intensity) is:

$$\overline{Y^2} = \int_{-\infty}^{\infty} y^2 \cdot f_Y(y) \cdot dy = \frac{1}{\pi} \int_0^{y_0} \frac{y^2}{\sqrt{y_0^2 - y^2}} dy =$$

$$= \frac{1}{\pi} \int_0^{y_0} \frac{(y_0{}^2 - y^2)}{\sqrt{y_0{}^2 - y^2}} dy - \frac{1}{\pi} \int_0^{y_0} \frac{y_0^2}{\sqrt{y_0^2 - y^2}} dy = -\frac{1}{\pi} \int_0^{y_0} \sqrt{y_0{}^2 - y^2}\, dy + \frac{2y_0{}^2}{\pi} \int_0^{y_0} \frac{dy}{\sqrt{y_0{}^2 - y^2}}$$

We calculate first integral $-1/2 \int_0^{y_0} \sqrt{y_0{}^2 - y^2}\, dy$ in stages:

$$\int_0^{y_0} \sqrt{y_0{}^2 - y^2}\, dy = \begin{vmatrix} u = \sqrt{y_0^2 - y^2} & d\nu = dy \\ du = -\dfrac{y \cdot dy}{\sqrt{y_0^2 - y^2}} & \nu = y \end{vmatrix} = y\sqrt{y_0^2 - y^2} \Big|_0^{y_0} - \int_0^{y_0} \frac{-y^2 dy}{\sqrt{y_0{}^2 - y^2}} =$$

$$- \int_0^{y_0} \frac{(y_0{}^2 - y^2 - y_0{}^2) dy}{\sqrt{y_0{}^2 - y^2}} = -\int_0^{y_0} \sqrt{y_0{}^2 - y^2}\, dy + y_0{}^2 \int_0^{y_0} \frac{dy}{\sqrt{y_0{}^2 - y^2}}$$

Thus, $\int_0^{y_0} \sqrt{y_0{}^2 - y^2}\, dy = y_0{}^2/2 \int_0^{y_0} dy \Big/ \sqrt{y_0{}^2 - y^2}$, and the variance of the amplitude is:

$$D_Y = \overline{Y^2} - \left(\overline{Y}\right)^2 = \frac{y_0{}^2}{\pi} \int_0^{y_0} \frac{dy}{\sqrt{y_0{}^2 - y^2}} - \left(\frac{y_0}{\pi}\right) = \frac{y_0{}^2}{\pi} \arcsin \frac{y}{y_0} \Big|_0^{y_0} - \left(\frac{y_0}{\pi}\right)^2 =$$

$$= \frac{y_0{}^2}{2} - \left(\frac{y_0}{\pi}\right)^2 = \frac{y_0{}^2}{2} \left(1 - \frac{2}{\pi}\right)$$

That is, the condition of non-dispersion is satisfied. The standard deviation of the amplitude is:

$$\sigma_Y = \frac{y_0}{\sqrt{2}}\sqrt{1-\frac{2}{\pi}}$$

3. Fluctuation cantilever model

3.1. Equal distribution of fluctuation phase (direct task)

Let us build a model of average amplitude when the t ωt_0 argument function:

$$x = y_0 \cos(\omega_0 t + \psi) \tag{7}$$

phase ψ gets random changes. Let us assume that phase ψ is distributed evenly with probability density $f_\Psi(\psi) = 1/2\pi$. Then, for Transformation (7), the inverse function and its derivation is $\psi = g^{-1}(x) = \cos^{-1} x$ and $(d/dz)\cos^{-1} x = -1\Big/\left(\pi\sqrt{x_0^2 - x^2}\right)$. Function (7) is ambiguous and has two roots: $\psi_1 = \cos^{-1}(x/y_0) - \omega_0 t$, and $\psi_2 = 2\pi - \psi_1$. Therefore, the density of probabilities $f_X(x)$ is:

$$f_X(x) = \frac{f_\Psi(\psi_1)}{\left|\pi\sqrt{y_0^2 - x^2}\right|} + \frac{f_\Psi(\psi_2)}{\left|\pi\sqrt{y_0^2 - x^2}\right|} = \frac{1}{\pi^2}\frac{1}{\sqrt{y_0^2 - x^2}}$$

The essence of averaging the $\overline{X}$ and $\overline{X^2}$ amplitude of fluctuation with a random phase probability density $f_\psi(\psi)$ is the averaging of trigonometric functions $\overline{\cos\Psi}$ and $\overline{\cos^2\Psi}$; that is, the averages of $\overline{X}$ and $\overline{X^2}$ are:

$$\overline{X} = y_0\overline{\cos\psi} = y_0\int_{-\infty}^{\infty}\cos\psi\, f_\Psi(\psi)d\psi = -\frac{y_0}{2\pi}\sin\psi\Big|_0^{2\pi} = 0$$

$$\overline{X^2} = y_0^2\overline{\cos^2\psi} = y_0^2\int_{-\infty}^{\infty}\cos^2\psi\, f_\Psi(\psi)d\psi = \frac{y_0^2}{4\pi}\int_0^{2\pi}(1+\cos 2\psi)d\psi = \frac{y_0^2}{2}$$

Amplitude variance is calculated by the formula:

$$D_X = \overline{X^2} - \left(\overline{X}\right)^2 = \frac{y_0^2}{2} \Rightarrow \sigma_X = \frac{y_0}{\sqrt{2}}$$

3.2. Rated phase fluctuation distribution

The case when random phase changes are subject to rated distribution with mathematical expectation m_ϕ and variance σ_Φ^2 $\left(\phi \in N(m_\Phi, \sigma_\Phi^2)\right)$ are more interesting from a practical point of view:

$$f_\Phi(\phi) = \frac{1}{\sqrt{2\pi}\sigma_\Phi} \exp\left(-\frac{(\phi - m_\Phi)^2}{2\sigma_\Phi^2}\right) \tag{8}$$

To convert $Z = y_0 \cos\Phi$, the inverse function and its derivation is $\phi = g^{-1}(z) = \cos^{-1} z\,(d/dz)\cos^{-1} z = -1\Big/\left(\pi\sqrt{y_0^2 - z^2}\right)$. Functions $z = \cos\phi$ and $z^2 = \cos^2\phi$ are ambiguous with periods $2\pi/\omega_0$, π/ω_0 and have two roots: $\phi_1 = \cos^{-1} z$ and $\phi_2 = 2\pi - \phi_1$; with $\phi_3 = \cos^{-1}(2z^2 - 1)$ and $\phi_4 = \pi - \phi_3$, we obtain that probability density $f_Z(z)$ is:

$$f_Z(z) = \frac{1}{\sigma_\Phi^2\sqrt{2\pi}} \begin{cases} \left|\frac{d}{dz}\cos^{-1} z\right| \cdot \exp\left(-\frac{1}{2\sigma_\Phi^2}\left[\cos^{-1} z - m_\Phi\right]^2\right) & \text{if} \quad \cos^{-1} z \in [0, y_0], \quad z \in [-\pi, 0) \\ \left|\frac{d}{dz}\cos^{-1} z\right| \cdot \exp\left(-\frac{1}{2\sigma_\Phi^2}\left[\cos^{-1} z - m_\Phi\right]^2\right) & \text{if} \quad \cos^{-1} z \in [0, y_0], \quad z \in [0, \pi] \end{cases} = \tag{9}$$

$$= \frac{1}{\sigma_\Phi^2\sqrt{2\pi}} \frac{1}{\sqrt{1 - z^2}} \cdot \exp\left(-\frac{1}{2\sigma_\Phi^2}\left[\cos^{-1}\phi - m_\Phi\right]^2\right) \quad \text{if} \quad \cos^{-1}\phi \in [0,1], \quad z \in [-\pi, \pi]$$

The average in this case are:

$$\begin{aligned} \overline{Z} &= I_1 + I_2 = \frac{y_0}{2}\exp\left(-\frac{\sigma_\Phi^2}{2}\right)\left[\exp(im_\Phi) + \exp(-im_\Phi)\right] = y_0 \exp\left(-\frac{\sigma_\Phi^2}{2}\right)\cos m_\Phi, \\ \overline{Z^2} &= I_1 + I_2 + I_3 = \frac{y_0^2}{2} + \frac{y_0^2}{2}\exp\left(-2\sigma_\Phi^2\right)\cos 2m_\Phi = \frac{y_0^2}{2}\left(1 + e^{-2\sigma_\Phi^2}\cos 2m_\Phi\right) \end{aligned} \tag{10}$$

and the variance of the amplitude is:

$$D_Z = \overline{Z^2} + \left(\overline{Z}\right)^2 = \frac{y_0^2}{2}\left(1 + e^{2\sigma_\Phi^2}\cos 2m_\Phi\right) + y_0^2 \exp(-\sigma_\Phi^2)\cos^2 m_\Phi$$

3.3. Mathematical model expectation and phase variance by equal amplitude distribution

Suppose that a sample of random amplitude values is obtained by measurements $s = y_0 \sin\theta$ with equal distribution $f_S(s) = 1/y_0$. Phase θ is defined as the inverse of the $S = y_0 \sin\Theta$ transformation of random variable S/y_0:

$$\Theta = \sin^{-1}\frac{S}{y_0} \tag{11}$$

Function $\theta = g(s/y_0) = \sin^{-1}(s/y_0)$ is ambiguous and has two roots in interval $[-y_0, y_0]$; $S_1/y_0 = \sin\Theta$ and $S_2/y_0 = -\sin\Theta$; inverted $s/y_0 = g^{-1}(\theta) = \sin\theta$ and derived from it:

$$\left|\frac{d\left(\frac{s}{y_0}\right)}{d\theta}\right| = \left|\frac{d}{d\theta}[\sin\theta]\right| = |\cos\theta| \tag{12}$$

The connection is true for cumulative probabilities in the function monotonicity of random variable transformation:

$$F_\Theta(\theta) = \mathrm{P}\left[\left(\sin^{-1}\frac{S}{y_0}\right) \le \theta\right] = \mathrm{P}\left[\frac{S_2}{y_0} \le \frac{S}{y_0} \le \frac{S_1}{y_0}\right] = F_S(+\sin\theta) - F_S(-\sin\theta) \tag{13}$$

and we get function by differentiation $f_\Theta(\theta) : f_\Theta(\theta) = (2/y_0)\, y_0 \,|\cos\theta| = 2\,|\cos\theta|$.

Let us set the boundaries of integration. Since the limits of parameter change s are $-y_0 \le s \le y_0$ in Formula (10), then $-1 \le (s/y_0) \le 1$; and according to equation $\theta = \sin^{-1}(s/y_0)$ for phase θ, the limits of integration are $-\pi/2 \le \theta \le \pi/2$ (Fig. 2).

Then, the average $\overline{\Theta}$ is obtained by integrating the parts of the integral:

$$\begin{aligned}\overline{\Theta} &= 2\int_{-\pi/2}^{\pi/2} \theta\cos\theta\, d\theta = \left|\begin{array}{ll} u = \theta & d\nu = \cos\theta d\theta \\ du = d\theta & \nu = \sin\theta \end{array}\right| = \\ &= 2\theta\sin\theta\Big|_{-\pi/2}^{\pi/2} + 2\int_{-\pi/2}^{\pi/2} \sin\theta\, d\theta = 2\pi\end{aligned} \tag{14}$$

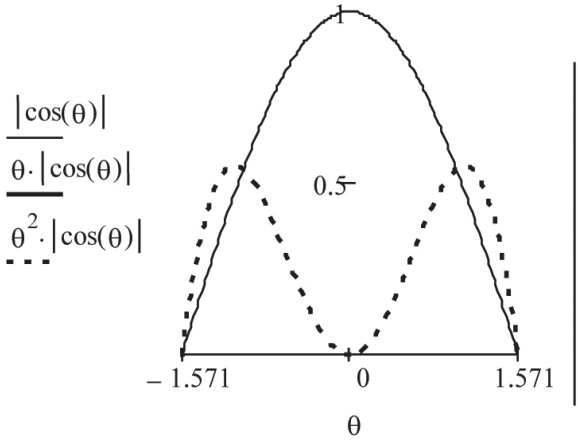

Fig. 2. Graphs of functions $f_\Theta(\theta)$ and subintegral expressions in Formulas (14) and (15)

The mean square of Integration (3) is:

$$\overline{\Theta^2} = 2\int_{-\pi/2}^{\pi/2} \theta^2 \cos\theta\, d\theta = \left| \begin{matrix} u = \theta^2 & d\nu = \sin\theta d\theta \\ du = 2\theta d\theta & \nu = -\cos\theta \end{matrix} \right| =$$

$$= \theta^2 \sin\theta \Big|_{-\pi/2}^{\pi/2} + 2\int_{-\pi/2}^{\pi/2} \theta \sin\theta\, d\theta = \pi^2 + 2\left| \begin{matrix} u = \theta & d\nu = \sin\theta d\theta \\ du = d\theta & \nu = -\cos\theta \end{matrix} \right| = \tag{15}$$

$$= \pi^2 + 2\pi - 2\int_{-\pi/2}^{\pi/2} \cos\theta\, d\theta = \pi^2 + 2\pi - 4$$

3.4. Rated $N(m_Q, \sigma_Q^2)$ distribution of random amplitude values

For law of fluctuations $q = y_0 \sin(\omega_0 t + w)$, the inverse transformation of random variable Q/y_0 has similar relevant patterns to those that are discussed in this paragraph. Then, the distribution function $f_W(w)$ of the probability density of converted random variable Q/y_0 is the following (Consortini 2000; Gradshteyn, Ryzhik 1963):

$$f_\Theta(\theta) = \frac{y_0}{\sqrt{2\pi\sigma_Q^2}} \cos(\theta + \Theta_0) \exp\left(-\frac{[y_0 \cos(\theta + \Theta_0) - m_Q]^2}{2\sigma_Q^2} \right) \tag{16}$$

Then, the average of $\overline{\Theta}$ i $\overline{\Theta^2}$ is:

$$\overline{\Theta} = 2\int_{-\infty}^{+\infty} \theta\cos(\theta+\Theta_0)\,d\theta = 4\int_{0}^{+\infty} \theta\cos(\theta+\Theta_0)\,d\theta$$
$$\overline{\Theta^2} = 2\int_{-\infty}^{+\infty} \theta^2\cos(\theta+\Theta_0)\,d\theta = 4\int_{0}^{+\infty} \theta^2\cos(\theta+\Theta_0)\,d\theta \quad (17)$$

4. Conclusions

The dynamics of the oscillations of cantilever-type oscillators has been studied. The probabilistic model of a cantilever is explained. The dependencies for the probability density, mean mathematical expectation, and standard deviation were developed. The fluctuation model of the cantilever was constructed, and the dependencies for the probability density for the direct problem were developed. The modeling of the mathematical expectation and phase variance for the inverse problem was performed.

REFERENCES

Battiston F.M., Ramseyer J.-P., Lang H.P., Baller M.K., Gerber Ch., Gimzewski J.K., Meyer E., Güntherodt H.-J., 2001, *A chemical sensor based on a microfabricated cantilever array with simultaneous resonance frequency and bending readout*, Sensor and Actuators B: Chemical, 77(1–2), 122–131.

Berman G.P., Chumak A.A., 2007, *Intrinsic dissipation in cantilevers*, AirXiv: 0709.2582v1, https://arxiv.org/abs/0709.2582 [17.09.2007].

Consortini A., 2000, *Should optics students known statistics?* In: Javier Sanchez-Mondragon J. (Ed.), *Sixth International Conference on Education and Training in Optics and Photonics*, Proc. SPIE, 3831, 47–55.

Gradshteyn I.S., Ryzhik I.M., 1963, *Tablitsy integralov, summ, ryadov i proizvedeniy*, Fizmatgiz, Moskva [Градштейн И. С., Рыжик И.М., 1963, *Таблицы интегралов, сумм, рядов и произведений*, Физматгиз, Москва].

Haran Dr. *Second-order Systems: Vibrating Cantilever Beams*, ME 3504 Process Monitoring & Control [online]: https://www.yumpu.com/en/document/view/12369805/second-order-systems-vibrating-cantilever-beams [10.09.2021].

Pietrzakowski M., 2002, *Experiment on a cantilever beam control and theoretical approximation*, Journal of Theoretical and Applied Mechanic, 40(3), 667–686.

Romaszko M., Sapiński, Sioma A., 2015, *Forced vibrations analysis of a cantilever beams using the vision method*, Journal of Theoretical and Applied Mechanic, 53(1), 243–254.

Voigtländer B., 2015, *Scanning Probe Microscopy. Atomic Force Microscopy and Scanning Tunneling Microscopy*, Springer.

Tsybenko S.O., Tarasevych Yu.Ya., 2016, *Ymovirnisni metody v mekhanitsi*, Natsional'nyy Tekhnichnyy Universytet, „Kharkivs'kyy Politekhnichnyy Instytut", Kharkiv [Цибенко С.О.,Тарасевич Ю.Я., 2016, *Ймовірнісні методи в механіці*, Національний Технічний Університет „Харківський Політехнічний Інститут", Харків].

Thermomechanical behavior of two-layer orthotropic cylindrical shell with local convective heat exchange with external environment

Roman Musii ORCID ID: 0000-0002-7169-2206

Lviv Polytechnic National University
Institute of Applied Mathematics and Fundamental Sciences
Department of Mathematics, Lviv
email: roman.s.musii@lpnu.ua

Nataliia Melnyk ORCID ID: 0000-0003-2337-2395

Lviv Polytechnic National University
Institute of Computer Science and Information Technologies
Department of Software, Lviv
email: nataliia.b.melnyk@lpnu.ua

Khrystyna Drohomyretska ORCID ID: 0000-0002-4987-7810

Lviv Polytechnic National University
Institute of Applied Mathematics and Fundamental Sciences
Department of Mathematics, Lviv
email: khrystyna.t.drohomyretska@lpnu.ua

Valentyn Shynder ORCID ID: 0000-0002-9414-5619

Lviv Polytechnic National University
Institute of Civil Engineering and Building Systems
Department of Strength of Materials and Structural Mechanics, Lviv
email: valentyn.k.shynder@lpnu.ua

Lyubomyr Hoshko ORCID ID: 0000-0002-3941-8995

Lviv Polytechnic National University
Institute of Applied Mathematics and Fundamental Sciences
Department of Mathematics, Lviv
email: liubomyr.v.hoshko@lpnu.ua

Marian Banaś ORCID ID: 0000-0003-3014-119X

AGH University of Science and Technology
Faculty of Mechanical Engineering and Robotics
Department of Power Systems and Environmental Protection Facilities, Krakow
email: mbanas@agh.edu.pl

ABSTRACT

A general solution of the heat conductivity and quasi-static thermoelasticity problems for a two-layer orthotropic cylindrical shell was obtained. Expressions for the integral characteristics of the temperature for the shell, which is locally heated by a temperature field or external environment by means of convective heat transfer at the initial moment of time, were recorded. The temperature and stress and strain state of the considered shell of a finite length depending on the physical parameters that corresponded to the thermophysical and mechanical characteristics of the materials of the constituent layers of the shell were studied, as were the geometrical parameters that determined the area of the local heating and heating time.

Keywords: cylindrical orthotropic shell, local thermal heating, temperature, stress and strain state

1. Introduction

As structural elements, two-layer orthotropic cylindrical shells are often used in various fields of modern technology (particularly in aerospace systems). This makes it possible to increase the strength and rigidity of the appropriate structures as well as protect them from low- or high-temperature thermal effects. Therefore, the study and analysis of the temperature and thermoelastic states of the shells under consideration are of great scientific and applied importance for calculating and predicting the thermomechanical behavior of relevant engineering structures.

To study the thermoelastic state of such shells, a model of thermomechanics is used; this consists of interconnected systems of equations of heat conductivity and thermoelasticity. If we neglect the effect of deformation on changes in the temperature field, these systems of equations become independent. This model is used in most cases of the thermal heating of structural elements.

Let us consider a closed circular two-layer cylindrical shell of an antisymmetric regular structure (referred to as cylindrical coordinate system x, θ, z). The shell had a finite length l, a radius R of the middle surface, and a constant thickness of $2h$. The orthotropy axes of each layer were transversely oriented at 0° and 90° angles to the coordinate axes. The shell material was a fiber-reinforced composite; therefore, such a shell is considered to be orthogonally reinforced.

From the model of the unconnected problem of the thermomechanics of shells with different geometric configurations for the analysis of the thermostressed state of the examined cylindrical orthotropic shell, we determined the temperature field of the shell that was caused by thermal heating at the first stage. Using the obtained temperature field, we got a solution for the quasi-static problem of thermoelasticity for this shell at another stage.

2. General solution of heat conductivity problem

Heat conductivity equations with respect to integral characteristics of temperatures T_1 and T_2 in the presence of heat sources take the following form (Hetnarski 2014; Kushnir et al. 2012):

$$\begin{aligned}
&\left(\Delta_{(1)} - \varepsilon_1^t\right)T_1 + \left(\Delta_{(2)} + \frac{\Lambda_{33}^{(1)}}{hR} - \varepsilon_2^t\right)T_2 - C^{(1)}\dot{T}_1 = -F_1^z \\
&\left(\Delta_{(2)} - \varepsilon_2^t\right)T_1 + \left(\Delta_{(3)} - \frac{\Lambda_{33}^{(1)}}{h^2} - \varepsilon_1^t\right)T_2 - C^{(3)}\dot{T}_2 = -F_2^z
\end{aligned} \tag{1}$$

Here, $\Delta_{(k)} = \Lambda_{11}^{(k)}\dfrac{\partial^2}{\partial x^2} + \dfrac{\Lambda_{22}^{(k)}}{R^2}\dfrac{\partial^2}{\partial \theta^2}$ $(k = 1, 2, 3)$;

$\varepsilon_i^t = \left(\alpha_z^+ - (-1)^i \alpha_z^-\right)$ $(j = 1, 2)$;

$F_1^z = \varepsilon_1^t t_1^z + \varepsilon_2^t t_2^z + W_1^t$; $F_2^z = \varepsilon_2^t t_1^z + \varepsilon_1^t t_2^z + W_2^t$;

where:

$\dot{T}_1, \dot{T}_2$ – derivatives of integral characteristics of temperatures T_1 and T_2, respectively, with respect to time variable τ,

$\alpha_z^{\pm}$ – heat transfer coefficients from $z = \pm h$ surfaces,

$\Lambda_{ij}^{(n)}, \Lambda_{33}^{(n)}, C^{(n)}$ – integral characteristics of thermophysical properties of material that is inhomogeneous over thickness of shell,

W_1^t, W_2^t – integral characteristics of heat sources.

For the unambiguity of the solution of the system of Equations (1), we accepted boundary conditions of $x = 0$ and $x = l$ at the edges of the shell:

$$T_1 = T_2 = 0 \tag{2}$$

and initial conditions at the moment of time $\tau = 0$:

$$T_1(x, \theta, 0) = T_1^0(x, \theta),\ T_2(x, \theta, 0) = T_2^0(x, \theta) \tag{3}$$

The solution of the system of Equations (1) under the boundary Conditions (2) and initial Conditions (3) using double finite Fourier transform in coordinates x, θ and integral Laplace transform in time τ took the following form:

$$T_1 = \sum_{n=1}^{\infty}\sum_{m=0}^{\infty}\sum_{\substack{j=1\\k\neq j}}^{2}\frac{\sin\frac{\pi n x}{l}\cos m\theta}{p_j - p_k}\left\{\left(p_j - g_4\right)Q_{1nm}Z_1^{(j)}(\tau) + g_2Q_{2nm}Z_2^{(j)}(\tau) + \right.$$

$$\left. + \left[\left(p_j - g_4\right)T_{1nm}^0 + g_2T_{2nm}^0\right]e^{-p_j\tau_1}\right\}$$

$$T_2 = \sum_{n=1}^{\infty}\sum_{m=0}^{\infty}\sum_{\substack{j=1\\k\neq j}}^{2}\frac{\sin\frac{\pi n x}{l}\cos m\theta}{p_j - p_k}\left\{\left(p_j - g_1\right)Q_{2nm}Z_2^{(j)}(\tau) + g_3Q_{1nm}Z_1^{(j)}(\tau) + \right. \tag{4}$$

$$\left. + \left[\left(p_j - g_1\right)T_{2nm}^0 + g_3T_{1nm}^0\right]e^{-p_j\tau_1}\right\}$$

Here

$$\left\{Q_{inm}, T_{inm}^0\right\} = \frac{\varsigma}{\pi l}\int_0^l\int_{-\pi}^{\pi}\left\{Q_i, T_i^0\right\}(x,\theta)\sin\frac{\pi n}{l}x\cos m\theta\, dx\, d\theta,\ \varsigma = \begin{cases}1, & m = 0\\ 2, & m \neq 0\end{cases},\ (i = 1, 2)$$

$$Z_i^{(j)} = \int_0^{\tau_1}\tilde{F}_i(u)\exp\left(-p_j(\tau_1 - u)\right)du,\ (i, j = 1,2)$$

$$p_j = \frac{g_1 + g_4}{2} + (-1)^j\sqrt{\frac{(g_1 - g_4)^2}{4} + g_2g_3}$$

Substituting the Expressions (4) into linear law $t = T_1 + (z/h)T_2$ of temperature distribution over the entire thickness of the shell under consideration, we obtained a general solution of the heat conductivity problem for it.

3. Temperature field at local heating

In the absence of heat sources, the shell is heated by a temperature field that is set at initial time $\tau = 0$ by expressions $T_1^{(0)}(x,\theta) = \phi(x,\theta)$, $T_2^{(0)} = 0$, or by convective heat exchange with the external environment, temperatures t_c^+, t_c^- of which was set by expres-

sions $t_c^+(x,\theta,\tau)=\phi(x,\theta)S_+(\tau)$, $t_c^-(x,\theta,\tau)=0$ on surfaces. Function $\phi(x, \theta)$, describing the local heating of the shell in a given region, was defined by the following expression:

$$\phi(x,\theta)=T^*\left(1-\frac{(x-x_0)^2}{d^2}\right)\left(1-\frac{\theta^2}{\eta^2}\right)\left[S_-(x-x_0+d)-S_+(x-x_0-d)\right]\times \\ \times\left[S_-(\theta+\eta)-S_+(\theta-\eta)\right] \tag{5}$$

where:

T^* = const,

$2d$ and 2η – width and angle, respectively, of heating area,

$(x_0, 0)$ – coordinates of center of this region,

$S_+(x)=\begin{cases}1, & x>0\\ 0, & x\le 0\end{cases}$; $S_-(x)=\begin{cases}1, & x\ge 0\\ 0, & x<0\end{cases}$ – asymmetric unit functions.

The T^0_{inm}, Q_{inm} Fourier coefficients took the following form:

$$\left\{T^0_{1n0}, Q_{in0}\right\}=\left\{1,\frac{\mathrm{Bi}}{2}\right\}\frac{16}{3}\frac{\eta T^*}{\pi^3 n^2\left(\frac{d}{l}\right)^2}\left(\frac{1}{\pi n}\sin\frac{\pi n d}{l}-\frac{d}{l}\cos\frac{\pi n d}{l}\right)\sin\frac{\pi n x_0}{l},\ T^0_{2n0}=0$$

$$\left\{T^0_{1nm}, Q_{inm}\right\}=\left\{1,\frac{\mathrm{Bi}}{2}\right\}\frac{32T^*}{\pi^3 n^2 m^2\eta^2\left(\frac{d}{l}\right)^2}\left(\frac{1}{\pi n}\sin\frac{\pi n d}{l}-\frac{d}{l}\cos\frac{\pi n d}{l}\right)\times \\ \times\left(\frac{1}{m}\sin m\eta-\eta\cos m\eta\right)\sin\frac{\pi n x_0}{l}$$

$$T^0_{2nm}=0,\ (m\neq 0),\ Z_k^{(j)}(\tau)=\frac{1}{p_j}\left(1-\exp(-p_j\tau_1)\right)S_+(\tau)$$

Then, the integral characteristics of temperatures T_1 and T_2 were given by the following formulas:

$$\{T_1, T_2\}=\sum_{n=1}^{\infty}\sum_{m=0}^{\infty}\{T_{1mn}, T_{2mn}\}\sin\frac{\pi n}{l}x\cos m\theta \tag{6}$$

4. Determination of thermostress state

Having integral characteristics of temperatures T_1 and T_2, we found components of displacement vector u_i and γ_i ($i = 1, 2, 3$) from the system of equations that were written in matrix form [1, 2]:

$$\mathbf{AY} = \mathbf{S}T_{1mn} + \mathbf{G}T_{2mn} \tag{7}$$

Here, matrices $\mathbf{A} = (a_{rk})_{6\times6}$, $\mathbf{Y} = (y_{kmn})_{6\times1}$, $\mathbf{S} = (s_k)_{6\times1}$, $\mathbf{G} = (g_k)_{6\times1}$; $y_{imn}=U_{imn}$, $y_{3+i,\,mn} = \Gamma_{imn}$ are the Fourier coefficients for displacements u_i, γ_i.

We solve the system of Equations (7) under the boundary conditions:

$$u_3 = u_2 = 0;\ \gamma_3 = \gamma_2 = 0;\ N_{11} = M_{11} = 0 \tag{8}$$

where: N_{11}, M_{11} are the forces and moments that were determined by the respective components of the stress tensor.

A solution of the system of Equations (7) was obtained using the double finite integral Fourier transform in coordinates x, θ. We calculated the coefficients of matrices a_{rk}, s_k and g_k, applying the double finite integral Fourier transform in coordinates x, θ to the expressions of the differential operators of the system of equilibrium equations:

$$\sum_{k}^{6} L_{rk} y_k = b_r \quad (r, k = 1, 2, \ldots, 6) \tag{9}$$

Here

$y_i = u_i; y_{3+i} = \gamma_i$ ($i = 1, 2, 3$);

$$L_{11} = A_{11}\partial_{11}^2 + \frac{A_{66}}{R^2}\partial_{22}^2,\ L_{12} = \frac{A_{12} + A_{66}}{R}\partial_{12}^2,\ L_{13} = \frac{A_{12}}{R}\partial_1,$$

$$L_{14} = B_{11}\partial_{11}^2 + \frac{B_{66}}{R^2}\partial_{22}^2,\ L_{15} = \frac{B_{12} + B_{66}}{R}\partial_{12}^2,\ L_{16} = \left(A_{13} + \frac{B_{12}}{R}\right)\partial_1,$$

$$L_{22} = A_{66}\partial_{11}^2 + \frac{1}{R^2}\left(A_{22}\partial_{22}^2 - k'A_{55}\right),\ L_{23} = \frac{A_{22} + k'A_{55}}{R^2}\partial_2,\ L_{24} = \frac{B_{12} + B_{66}}{R}\partial_{12}^2,$$

$$L_{25} = B_{66}\partial_{11}^2 + \frac{B_{22}}{R^2}\partial_{22}^2 + \frac{k'A_{55}}{R},\ L_{26} = \left(\frac{A_{23}}{R} + \frac{B_{22} + k'B_{55}}{R^2}\right)\partial_2,$$

$$L_{33} = -k'A_{44}\partial_{11}^2 - \frac{k'A_{55}}{R^2}\left(k'A_{55}\partial_{22}^2 + A_{22}\right),\ L_{34} = \left(\frac{B_{12}}{R} - k'A_{44}\right)\partial_1,$$

$$L_{35} = \frac{1}{R}\left(\frac{B_{22}}{R} - k'A_{55}\right)\partial_2,\ L_{36} = -k'B_{44}\partial_{11}^2 + \frac{1}{R^2}\left(B_{22} - k'B_{55}\partial_{22}^2\right) + \frac{A_{23}}{R},$$

$$L_{44} = D_{11}\partial_{11}^2 + \frac{D_{66}}{R^2}\partial_{22}^2 - k'A_{44},\ L_{45} = \frac{D_{12} + D_{66}}{R}\partial_{12}^2,\ L_{46} = \left(\frac{D_{12}}{R} + B_{13} - k'B_{44}\right)\partial_1,$$

$$L_{55} = D_{66}\partial_{11}^2 + \frac{D_{22}}{R^2}\partial_{22}^2 - k'A_{55},\ L_{56} = \frac{1}{R}\left(B_{23} - k'B_{55} + \frac{D_{22}}{R}\right)\partial_2,$$

$$L_{66} = A_{33} + \frac{2B_{23}}{R} + \frac{1}{R^2}\left(D_{22} - k'D_{55}\partial_{22}^2\right) - k'D_{44}\partial_{11}^2,$$

$$b_1 = A_{11}^t\partial_1 T_1 + \frac{B_{11}^t}{h}\partial_1 T_2 - q_1,\ b_2 = \frac{A_{22}^t}{R}\partial_2 T_1 + \frac{B_{22}^t}{Rh}\partial_2 T_2 - q_2,$$

$$b_3 = \frac{A_{22}^t}{R}T_1 + \frac{B_{22}^t}{Rh}T_2 + q_3,\ b_4 = B_{11}^t\partial_1 T_1 + \frac{D_{11}^t}{h}\partial_1 T_2 - m_1,$$

$$b_5 = \frac{B_{22}}{R}\partial_2 T_1 + \frac{D_{22}^t}{Rh}\partial_2 T_2 - m_2,$$

$$b_6 = \left(A_{33}^t + \frac{B_{22}^t}{R}\right)T_1 + \frac{1}{h}\left(B_{33}^t + \frac{D_{22}^t}{R}\right)T_2 + m_3,\ \left\{A_{ii},\ B_{ij},\ D_{ij}\right\} = \int_{-h}^{h} c_{ij}\left\{1,\ z,\ z^2\right\}dz,$$

$$\left\{A_{ii}^t,\ B_{ii}^t,\ D_{ii}^t\right\} = \int_{-h}^{h} \beta_{ii}^t\left\{1,\ z,\ z^2\right\}dz,\ \ k' - \text{shear coefficient.}$$

A solution of the system of Equations (9) was obtained in the following form:

$$y_{kmn} = \frac{1}{|A|}\sum_{r=1}^{6}\left(s_r T_{1mn} + g_r T_{2mn}\right)B_{rk},\ (k = 1, 2, ..., 6) \tag{10}$$

where: $|A|$ is determinant of matrix **A**, and B_{rk} is algebraic complement to element a_{rk} of this matrix.

Generalized displacements in terms of the Fourier coefficients are written by the following formulas:

$$\{u_1, \gamma_1\} = \sum_{n=0}^{\infty} \sum_{m=0}^{\infty} \{U_{1mn}, \Gamma_{1mn}\} \cos\frac{\pi n}{l} x \cos m\theta,$$

$$\{u_2, \gamma_2\} = \sum_{n=1}^{\infty} \sum_{m=1}^{\infty} \{U_{2mn}, \Gamma_{2mn}\} \sin\frac{\pi n}{l} x \sin m\theta, \tag{11}$$

$$\{u_3, \gamma_3\} = \sum_{n=1}^{\infty} \sum_{m=0}^{\infty} \{U_{3mn}, \Gamma_{3mn}\} \sin\frac{\pi n}{l} x \cos m\theta$$

According to known generalized displacements in Formula (11) and the integral temperature characteristics in Formula (6), all of the other characteristics of the stress and strain state of the shell were determined using the known formulas (Hetnarski 2014; Kushnir et al. 2012), of expressions of the deformation component of an arbitrary point of shell e_{ij} in terms of generalized displacements u_i, γ_i (taking into account the physical equations for stresses σ_{ij} and strains ε_{ij} ($i, j = 1, 2, 3$) and internal forces N_{ij} and moments M_{ij}).

5. Analysis of numerical results

Numerical studies were performed for a two-layer cylindrical shell of an antisymmetric regular structure. The shell layers were made of an orthogonally reinforced graphite-epoxy composite with the following physical and mechanical properties (Reddy 2004): E_L = 150 GPa; E_T = 110 GPa; G_{LT} = 35 GPa; G_{TT} = 41 GPa; $\nu_{LT} = \nu_{TT}$ = 0,33; $\alpha_L = 7{,}6 \cdot 10^{-6}$ 1/K; $\alpha_T = 14{,}0 \cdot 10^{-6}$ 1/K; λ_L = 105 W/(m·K); λ_T = 75 W/(m·K) (indices L and T indicate the parallel and perpendicular directions, respectively, to the reinforcing fibers).

The values of the other parameters were selected as follows: h/R = 0,05, l/R = 5; $\eta = \pi/4$; $d/l = (R/l)\sin\eta$; $x_0 = l/2$; $k' = 5/6$; Bi = 1.

For the given parameters, the values of dimensionless average temperature $T_1' = T_1 / T^*$, temperature gradient $T_2' = T_2 / T^*$, and temperature field $t' = t/T^*$ were numerically studied for different values of dimensionless time $\tau' = \lambda_{22}\tau/(c_e h^2)$ and dimensionless heat transfer coefficient (Biot criterion) $\mathrm{Bi} = \alpha_z h/\lambda_{22}$.

In Figure 1, the change in values T_1' and T_2' along generatrix $\theta = 0$ ($0.5 \le x' \le 1$) are shown, and in Figure 2 – the change of the same quantities along guide line $x' = 0.5$ ($0 \le \theta \le \pi$) at different time points τ' are shown. The dependence of average

temperature T_1' on time τ' for various values of the heat transfer coefficient is illustrated in Figure 3.

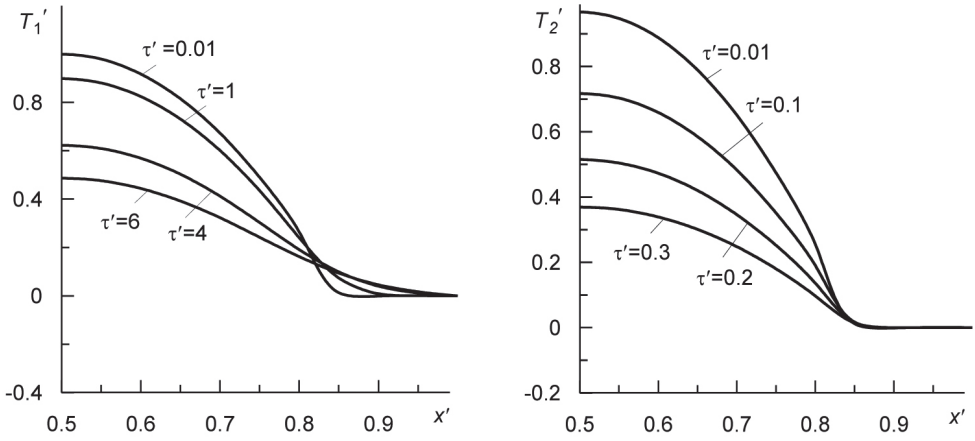

Fig. 1. Changes in T_1' and T_2' along generatrix $\theta = 0$ $(0.5 \le x' \le 1)$ at different times τ'

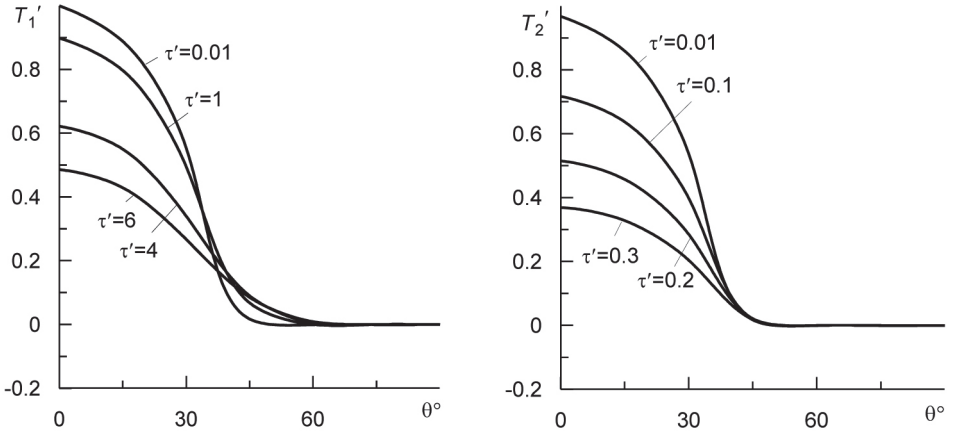

Fig. 2. Changes in T_1' and T_2' along guide line $x' = 0.5$ $(0 \le \theta \le \pi)$ at different times τ'

In Figure 4, the graphs of the dependence of temperature field t' on transverse coordinate $z' = z/h$ for the Bi = 0.1, 0.2, 0.3 values are shown. The solid lines correspond to the solution of the system of equations (which were written under the linear law of temperature distribution over the thickness of the shell), and the dashed lines correspond to the cubic law. The results that are shown in Figures 1–3 were obtained under the conditions of shell heating by a temperature field that was specified at the initial moment of time, and the results that are presented in Figure 4 were achieved when the shell was heated by the environment by convective heat transfer.

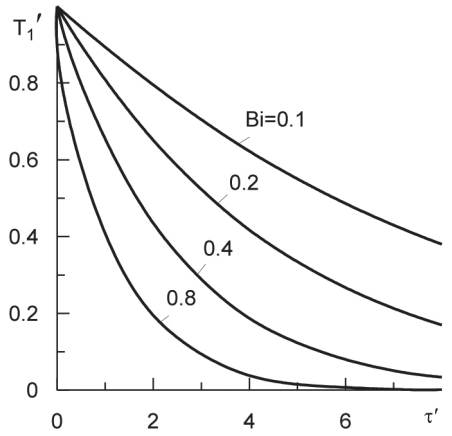

Fig. 3. Dependence of average temperature T_1' on time τ' for various values of heat transfer coefficient Bi

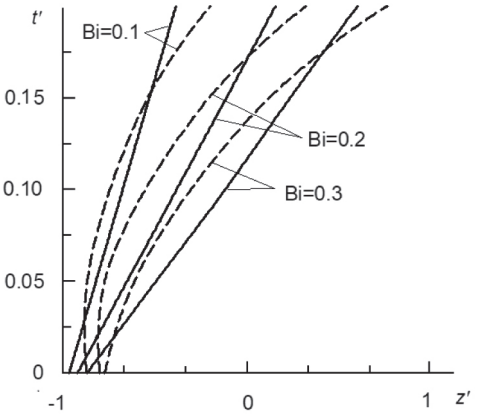

Fig. 4. Dependences of temperature t' on transverse coordinate $z' = z/h$ for values of heat transfer coefficient Bi

From an analysis of the numerical results and Figures 1–4, it follows that the maximum values of the average temperature and temperature gradient were reached in the center of the heating region ($x' = 0.5$, $\theta = 0$). As we moved away from the center of this region, these monotonically decreased to zero. Since there was heat exchange with the environment, the temperature characteristics decreased over time. This decrease was more intense for the temperature gradient; this was also the case with increases in the heat transfer coefficient. The temperature gradient was only significant at the initial moments of time; then, it rapidly decreased. For the composite under consideration, the layered structure of the material did not significantly affect the temperature distribution in the shell.

To analyze the thermomechanical behavior of the examined shell, the infinite stresses $\sigma'_i = \sigma_{ii} / E_L \alpha_L T^*$, $\sigma'_{23} = \sigma_{23} / E_L \alpha_L T^*$ ($i = 1, 2$) for four values (0.01, 0.1, 0.4, 1) of infinite time $\tau' = \lambda_T \tau / c_\varepsilon h^2$ were numerically analyzed. The changes in the axial σ'_1 and azimuthal σ'_2 stresses along guide line $x' = 0.5$ from the middle of the heated area to the middle of the unheated area ($0 \le \theta \le \pi$) at different times τ' are illustrated in Figure 5. Normal stresses were calculated on the outer $z' = z/h = 1$ surface. It was obtained that, at the initial time in the heating region, the stresses were compressive, and the maximum values were reached at point (0.5; 0). With increasing time, the stresses and displacements in the heating region and beyond were equalized.

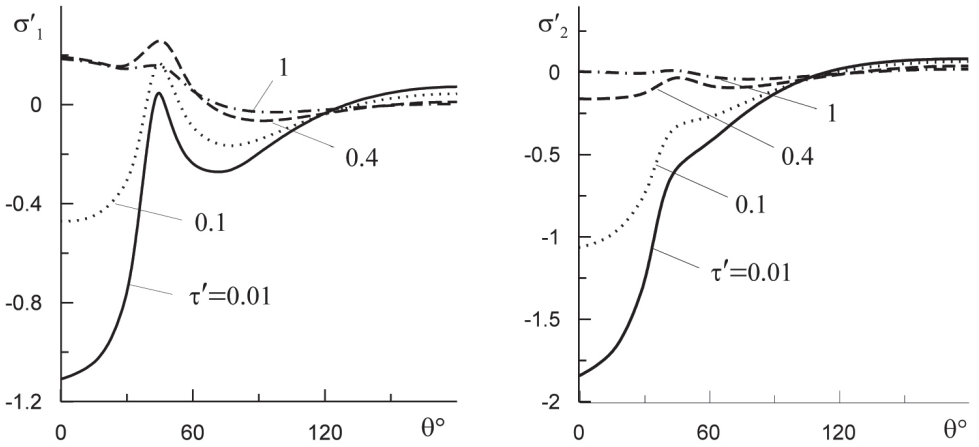

Fig. 5. Dependence of axial σ'_1 and azimuthal σ'_2 stresses along guide line $x' = 0.5$ from middle of heated area to middle of unheated area ($0 \le \theta \le \pi$) at different times τ'

6. Conclusions

On the basis of a two-dimensional mathematical model of heat conductivity for layered orthotropic cylindrical shells using the integral Fourier transforms in spatial variables and the Laplace transform in time, a general solution of the heat conductivity problem was obtained. Expressions of the integral characteristics of temperature for a two-layer shell (which at the initial moment of time was locally heated by a temperature field or the environment by convective heat exchange) were obtained.

Using the equations of the six-modal linear shear theory of the first order, the stress and strain state of the considered two-layer orthotropic circular closed cylindrical shell of finite length was investigated.

The dependencies of the integral characteristics of the temperature and the components of the stress tensor on the physical parameters that corresponded to the thermophysical and mechanical characteristics of the materials of the component layers of a shell as well as on the geometrical parameters that defined the area of local heating and time of heating were the theoretical bases for forecasting the thermomechanical behavior of two-layer orthotropic cylindrical shells under the appropriate conditions of local heating.

REFERENCES

Hetnarski R.B. (Ed.), 2014, *Encyclopedia of Thermal Stresses*, Springer.

Kushnir R.M., Nykolyshyn M.M., Zhydyk U.V., Flyachok V.M., 2012, *On the theory of inhomogeneous anisotropic shells with initial stresses*, Journal of Mathematical Science, 186, 61–72.

Reddy J.N., 2004, *Mechanics of Laminated Composite Plates and Shells. Theory and Analysis*, CRC Press, New York.

Topology optimization parameters of blades of wind turbines

Krzysztof Pytel ORCID ID: 0000-0002-1924-8351

AGH University of Science and Technology
Faculty of Mechanical Engineering and Robotics
Department of Power Systems and Environmental Protection Facilities, Krakow
email: kpytel@agh.edu.pl

Andriy Zdobytskyi ORCID ID: 0000-0001-8044-9593

Lviv Polytechnic National University
Institute of Computer Science and Information Technologies
Department of Computer-Aided Design Systems, Lviv
email: andrii.y.zdobytskyi@lpnu.ua

Mykhaylo Lobur ORCID ID: 0000-0001-7516-1093

Lviv Polytechnic National University
Institute of Computer Science and Information Technologies
Department of Computer-Aided Design Systems, Lviv
email: mykhaylo.v.lobur@lpnu.ua

Roman Panchak ORCID ID: 0000-0002-6422-7656

Lviv Polytechnic National University
Institute of Computer Science and Information Technologies
Department of Computer-Aided Design Systems, Lviv
email: roman.t.panchak@lpnu.ua

Anna Hnatiuk ORCID ID: 0000-0002-0623-5041

Lviv Polytechnic National University
Institute of Computer Science and Information Technologies
Department of Computer-Aided Design Systems, Lviv
email: anna.hnatiuk.knm.2019@lpnu.ua

ABSTRACT

This work provides peculiarities of the production of various elements of complex geometric shapes by the newest technologies of additive production. It considers the possibility of modernizing and improving the design of wind turbine blades by the classical method of topological optimization while taking the wind load vector into account and preserving their functional properties. Using the topological optimization algorithm of the Inventor Nastran software environment, the design of a wind turbine blade was automatically generated in accordance with the geometric constraints on the shape and minimization in terms of its weight and maximum rigidity. It also shows the peculiarities of generating a wind turbine blade design with changes in the parameters of topological optimization ([COMPVF], [TOPTMANCONSTR], [TOPGEN], and [TOPTMANCORD]) and the maximum and minimum airflow forces.

Keywords: topological optimization, blade, wind turbine, stiffness, material minimization, wind load

1. Introduction and research objective

The development of alternative energy sources (namely, wind energy) is undoubtedly an important area for implementing energy systems. Modern wind turbines are bulky structures that can only work properly in a narrow area of wind load; under the influence of variable wind loads, however, the blades of wind turbines become deformed, which leads to a decrease in their efficiency (Ma et al. 2016). Therefore, the main criteria for designing wind turbine blades are optimization by the weight and maximum rigidity of a structure while taking the spectrum of the natural frequencies of oscillations, geometric, and production constraints into account (along with their contact interaction).

The gradual development of composite materials has opened up new ways of using them in fundamentally new industries and aspects. Due to the expansion of such functional properties as their increased strength, corrosion resistance, and lightweight construction, composite materials are gradually gaining popularity in the wind energy industry. However, ensuring the proper functionality of materials is virtually impossible without the use of modern technologies of engineering calculation and design. The rapid development of new technologies and models of additive production (namely, the introduction of new design techniques) contributes to the production of various elements of complex geometric shapes. As a result, the requirements for the quality of manufacture of both individual parts/components and units as a whole increase.

Generative design, generated design, topological optimization, structural optimization, and bionic design are the most common ways of developing, optimizing, and creating lightweight structures.

In the environments of computer aided design and engineering analysis, the following optimization methods are have been implemented at:

- topological – which provides the optimal distribution of the material in a calculation area based on the boundary conditions, objective function, and constraints;
- topographic – which determines the optimal direction of stiffening ribs of stamped sheet metal parts based on the boundary conditions, target function, and constraints;
- thickness optimization – determines the optimal thickness of sheet metal parts in a structure based on the boundary conditions, target function, and constraints;
- optimization of mesh structures – the optimal area of the intersection of the elements of mesh structures based on the boundary conditions, target function, and constraints (Altair Inspire 2021; Bendsøe, Kikuchi 1988).

Generating structures by using methods of topological optimization and generative design significantly expands their functionality (Meng et al. 2020). Due to the creation of lightweight matrix structures of blades, their proper geometric parameters are provided, taking fatigue and impact resistance into account as well as durability in accordance with the action of wind load.

2. Methodology of research

Topological design optimization provides the optimization of the structure of a design object at the initial stage within a given three-dimensional spatial location with a set of rules that are set by the user. Accordingly, the maximum performance of the system is ensured by the mathematical modeling and optimization for external forces, boundary conditions, and existing constraints.

However, the topology optimization of the part is the first step in the design process; this is usually too difficult to implement, as it is also necessary to take the issue of the manufacturability of a structure into account. Nonetheless, the use of topology optimization at the initial stage of design provides the appropriate functionality and necessary characteristics of the structural elements to perform their functions. As a result, the basis of the final design is programmatically implemented.

Conventional topology optimization uses the finite element method for evaluating the effectiveness of a design according to certain criteria.

The classical method of topological optimization is based on the method of density distribution (Ma et al. 2016); within this, the material distribution parameter is set by using controlled parameters through the interpolation function. Interpolation functions for solid and non-solid materials are built into the functionality of Autodesk

Nastran In-CAD software, so the density of isotropic material is taken into account for optimization (ranging from 0 to 1). Other methods consider local material orientation (for non-isotropic materials) and even other characteristics (Bendsøe 1989; Bendsøe, Sigmund 2003).

Each element is filled with material for those areas in which it is needed or its absence for those areas where it can be removed (representation of voids). The distribution of the material density within design domain ρ is discrete; therefore, each element is assigned a binary value (Fig. 1) (Razvan 2014).

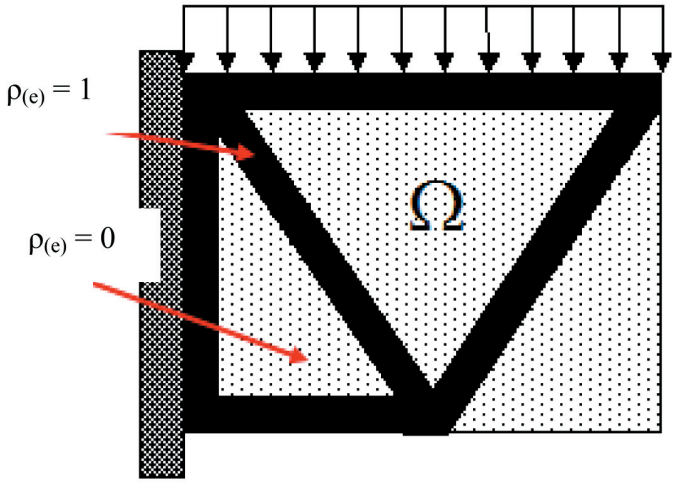

Fig. 1. Optimized structure of material distribution according to set conditions: $\rho_{(e)} = 1$ – material required (black); $\rho_{(e)} = 0$ – material removed (white)

Since the relative density of a material can change continuously, the material's Young's modulus can also be constantly changing on each element. For each element "e", there are correlations between the coefficient of relative density of the material ρ_e and Young's modulus for elasticity of the isotropic model of the material E_0 (as calculated by the power function) (Fig. 2):

$$E(\rho_e) = \rho_e^p E_0 \tag{1}$$

The loss-correction parameter reduces the proportion of the elements with intermediate densities (gray elements) to total stiffness and controls the optimization solution for those elements that are represented by total black ($\rho_e = 1$) or removed – white ($\rho_e = \rho_{min}$). The loss adjustment parameter is usually $p = 3$.

In the process of performing each iteration, optimization algorithms analyze the sensitivity to estimate the types of material density on the target indicators in order to maximize the stiffness.

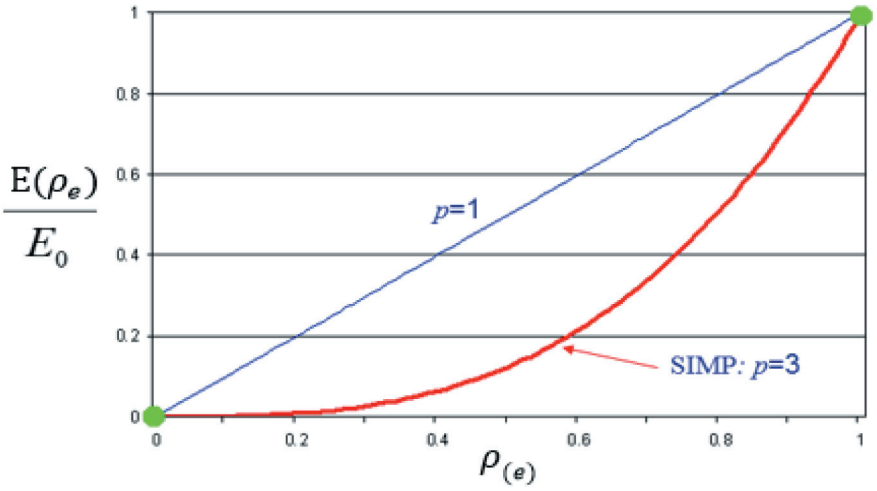

Fig. 2. Optimized structure of material distribution according to set conditions

The optimization algorithm is based on finding the local minimum, starting with different initial volume particles and different grids – the densities of which will lead to different construction designs. Topology optimization is determined based on isogeometric analysis with a global stress limitation. The iterations of the optimization continue until the convergence of different target functions and the achievement of iterations of their matching criteria:

$$\sigma_{\text{global}} = \sigma_{\max} \left\{ \frac{1}{N} \sum_{e=1}^{N} \left(\frac{\sqrt{\rho_e}\,\sigma_{\text{vM}}^{e}}{\sigma_{\max}} \right)^{p} \right\}^{\frac{1}{p}} \leq \sigma_{\max} \tag{2}$$

where:

$\sigma_{\max}$ – allowable stress [MPa],
σ_{vM} – von Mises stress [MPa],
N – number of topology optimization elements,
$p \sim 10$ – approximation exponent.

3. Main results and their discussions

To verify the adequacy of the described assumptions about increasing the strength of wind turbine blades by topological optimization methods, we will use computer-aided CAD modeling and CAE engineering analysis with the appropriate modules of topological optimization and design (Rozvany et al. 1992; Zdobytskyi et al. 2021).

A wind turbine blade is made of polymeric material with high mechanical strength and impact resistance, abrasion resistance, and multiple deformations during the stretching and bending; it retains its high impact resistance and strength characteristics in an operating temperature range of –40° to +60°C. Therefore, we will use the classic method of topological optimization solid isotropic material penalization (SIMP) (for isotropic materials). In the Autodesk Inventor Nastran environment, we will create constraints to remove unwanted material and generate a more optimal wind turbine blade design (Fig. 3), making its structure hollow (Pedersen, Allinger 2006).

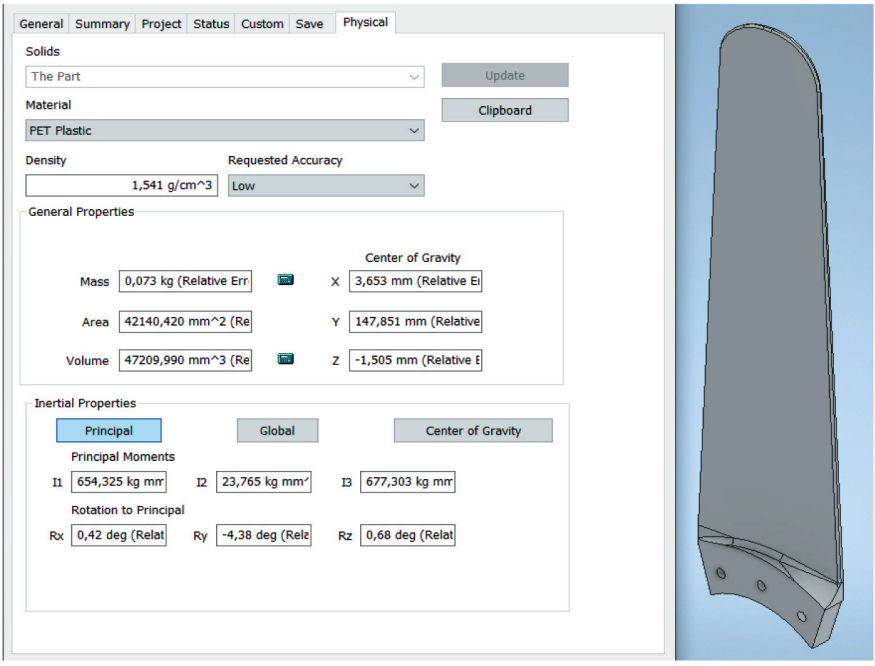

Fig. 3. Automatically generated wind turbine blade structure

At the initial stage of the design, we will create a three-dimensional model of a wind turbine blade and investigate it for tensions and deformations that arise under the action of a wind load of 380 Pa (Fig. 4).

Since the classical method of topological optimization is based on the finite element method, the density of the material varies from 0 to 1 at each given optimization point. For the automatic generation of topology optimization (TOPGEN) that is in accordance with a linear static analysis of the stress-strain state of the structure, we set design constraints on volume particle minimization (COMPVF) and additive layer fabrication (TOPTMANCONSTR). We also indicate the planes of symmetry of the constraints and the direction of the extrusion of the material (TOPTMANCORD) in Figure 5.

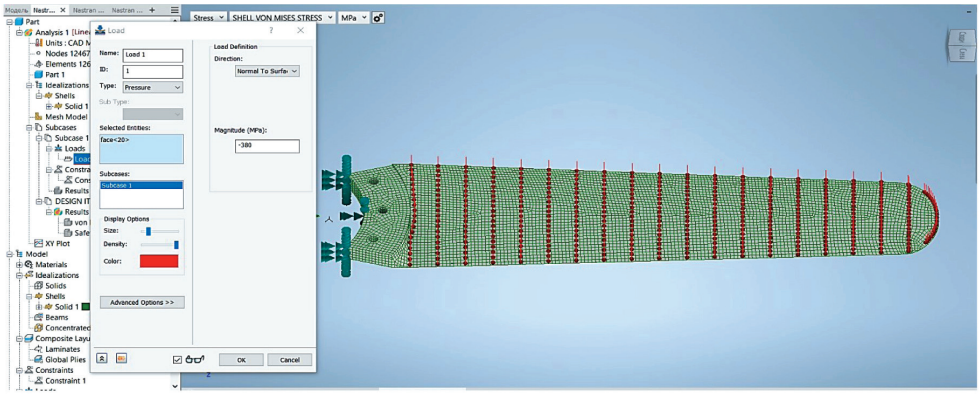

Fig. 4. Automatically generated wind turbine blade structure

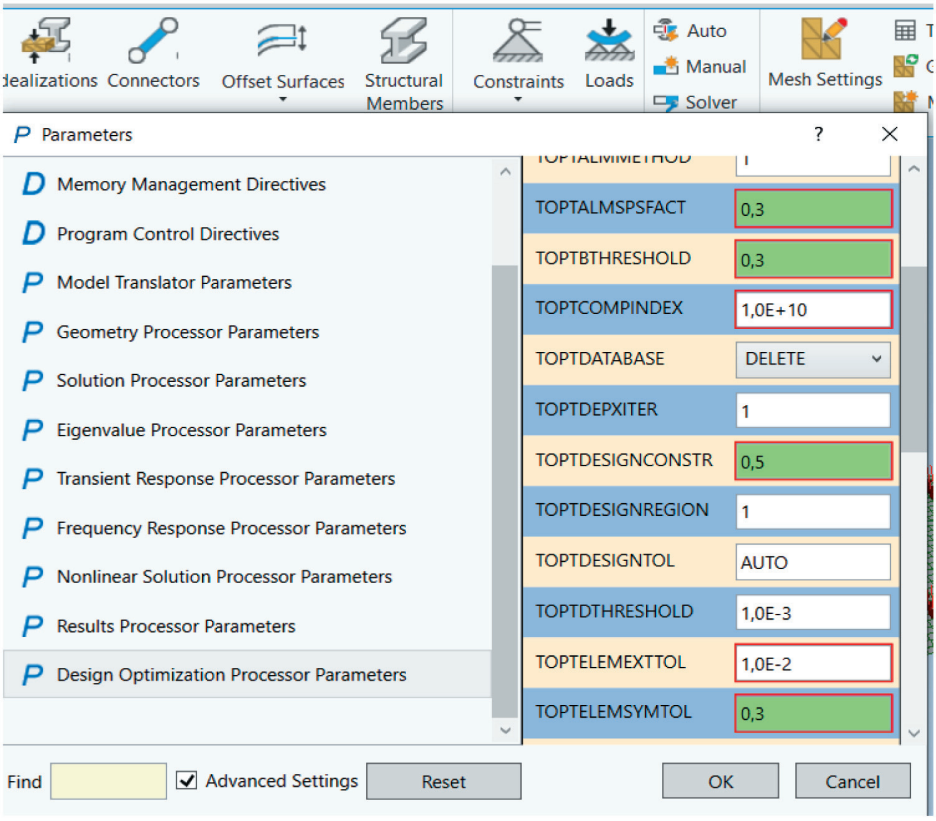

Fig. 5. Topology optimization processor parameters

The material constraints were determined by the volume fraction, where the maximum material that is allowed in the final design is described as the fraction of the

material that is available at the beginning of the optimization. The values of the topology optimization design constraint based on the TOPTGEN parameters were 0.3, 0.5, and 0.7, respectively (Fig. 6).

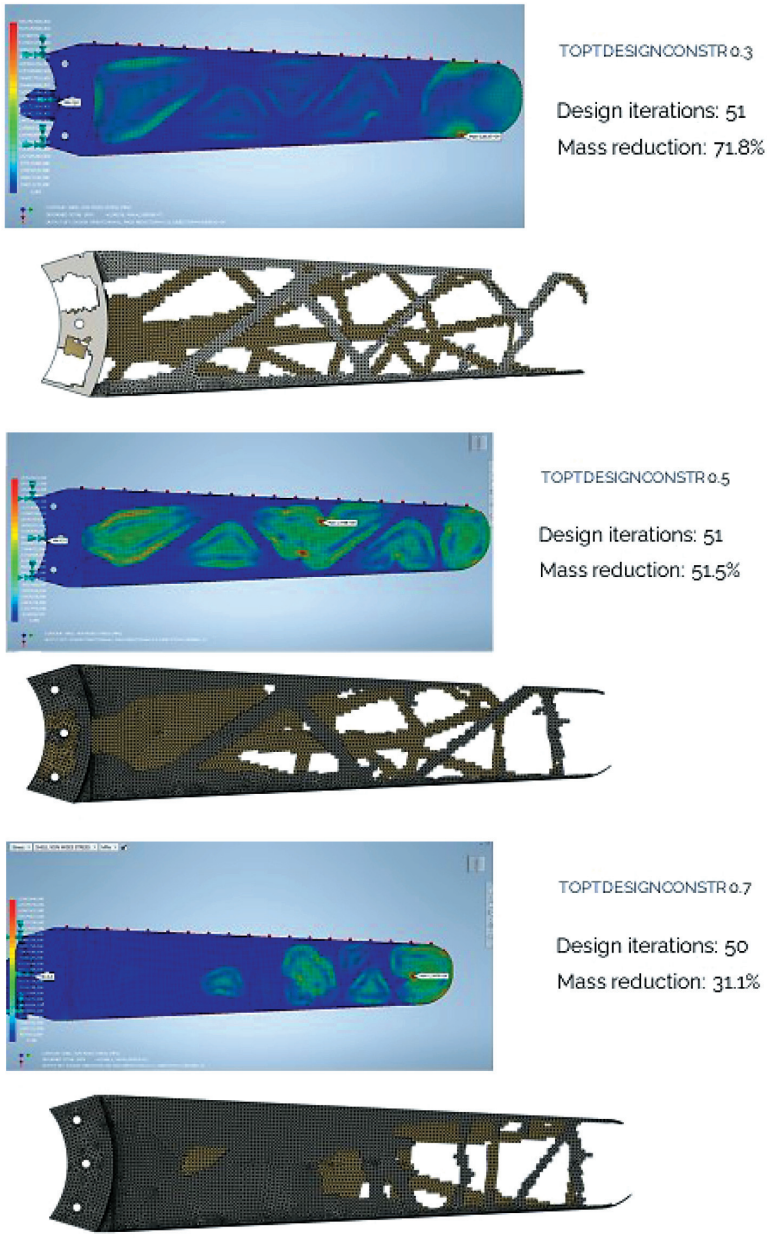

Fig. 6. Automatically generated structure of wind turbine blades by limiting density of grid and volume fractions of 0.3, 0.5, and 0.7

4. Conclusion

The topological optimization of a structure optimizes the structure of a design object at the initial stage within a given three-dimensional spatial location with a set of rules that are set by the user. Accordingly, the software implements the maximum performance of the system through the mathematical modeling and optimization for external forces, boundary conditions, and existing constraints.

The implementation of the topological optimization algorithm by Autodesk Inventor Nastran enables solutions to multi-purpose design problems that are intuitively difficult to predict. The structure of a wind turbine blade is automatically generated and provides the maximum possible rigidity and minimization of the material in accordance with the action of the wind load vector. By changing the TOPTDESIGNCONSTR parameter to within a range of 0 to 1, the method gives us a wide range of improved forms of the model for its further reproduction while employing additive production.

REFERENCES

Altair Inspire. Available: https://infcs.ru/catalog/promyshlennyy-dizayn/altair-inspire/ [18.10.2021].

Bendsøe M.P., 1989, *Optimal shape design as a material distribution problem*, Structural Optimization, 1, 193–202.

Bendsøe M.P., Kikuchi N., 1988, *Generating optimal topologies in structural design using a homogenization method*, Computer Methods in Applied Mechanics and Engineering, 71(2), 197–224.

Bendsøe M.P., Sigmund O., 2003, *Topology Optimization: Theory, Methods, and Applications*, Springer-Verlag, Berlin – Heidelberg – New York.

Ma Y., Xu S., Liu H., Wang X., 2016, *Optimization of reinforcing ribs of a hollow fan blade using metamodel-based optimization algorithm conference*, Proceedings of ASME Turbo Expo 2016: Turbine Technical Conference and Exposition June 2016. DOI: https://doi.org/10.1115/GT2016-57226.

Meng L., Zhang W., Quan D., Shi G., Tang L., Hou Y., Breitkopf P., Zhu J., Gao T., 2020, *From topology optimization design to additive manufacturing: today's success and tomorrow's roadmap*, Archives of Computational Methods in Engineering, 27, 805–830. DOI: https://doi.org/10.1007/s11831-019-09331-1.

Pedersen C.B.W., Allinger P., 2006, *Industrial implementation and applications of topology optimization and future needs*. In: Bendsøe M.P., Olhoff N., Sigmund O. (Eds.), *IUTAM Symposium on Topological Design Optimization of Structures, Machines, and Materials: Status and Perspectives*, Springer, 147–156.

Razvan C., 2014, *Overview of structural topology optimization methods for plane and solid structures*, Annals of the Oradea University, Fascicle of Management and Technological Engineering, 3(3). DOI: https://doi.org/10.15660/AUOFMTE.2014-3.3043.

Rozvany G.I.N, Zhou M., Birker T., 1992, *Generalized shape optimization without homogenization*, Structural Optimization, 4(3–4), 250–252.

Zdobytskyi A., Lobur M., Panchak R., Sika R., Kalinowski K., 2021, *Increasing the strength of materials by topological optimization methods*, 16th International Conference on the Experience of Designing and Application of CAD Systems (CADSM), 6–9. DOI: https://doi.org/10.1109/CADSM52681.2021.9385222.

Ways to increase efficiency of lidar scan system of three-dimensional objects

Andriy Zdobytskyi ORCID ID: 0000-0001-8044-9593

Lviv Polytechnic National University
Institute of Computer Science and Information Technologies
Department of Computer-Aided Design Systems, Lviv
email: andrii.y.zdobytskyi@lpnu.ua

Uliana Marikutsa ORCID ID: 0000-0002-9514-7413

Lviv Polytechnic National University
Institute of Computer Science and Information Technologies
Department of Computer-Aided Design Systems, Lviv
email: uliana.b.marikutsa@lpnu.ua

Mykola Khranovskyi ORCID ID: 0000-0002-1633-6639

Lviv Polytechnic National University
Institute of Computer Science and Information Technologies
Department of Computer-Aided Design Systems, Lviv
email: mykola.khranovskyi.mknit.2021@lpnu.ua

Vladyslav Yusiuk ORCID ID: 0000-0002-5608-3920

Lviv Polytechnic National University
Institute of Computer Science and Information Technologies
Department of Computer-Aided Design Systems, Lviv
email: vladyslav.yusiuk.mknit.2021@lpnu.ua

ABSTRACT

This article discusses the main methods of scanning three-dimensional objects and the features of using lidars as devices for this purpose; it is a comparative analysis of different types of optical, acoustic, and laser devices. Areas of the use of these technologies have been considered. The principle of laser scanning operations is also described in detail, as is the operations of radiating and reading devices. Information is recorded by the system about an object as well as additional parameters. The classification of the returned signal and additional attributes that the sensor takes into account are considered. Based on this information, a mobile system has been developed that optimizes the use of lidars and allows one to use similar systems that work with mobile applications.

Keywords: laser, cloud of points, API, lidar, radar, scanning, 3D modeling

1. Introduction

Modern 3D scanners are high-tech devices – the primary purpose of which is to create three-dimensional models of various physical objects. 3D scanners allow one to measure linear dimensions with high accuracy, determine any object's geometric shape, and then create a three-dimensional digital model. Then, one can perform any manipulations and calculations in computer programs with this 3D model.

In industry, one of the main areas of the application of 3D scanners is reverse engineering. When designing almost any industrial product (from a car to a toothbrush), one must usually create a lot of iterations until an optimal shape is achieved. In industry, various types of 3D scanners are also used to control the quality and other parameters of finished products. In science, 3D scanners are used in archeology and paleontology, for example, to reproduce the forms of various ancient objects and the appearance of fossils. 3D scanners help to create accurate models of any works of art: sculptures, statuettes, jewelry, and other products as well as paintings in their original frames. In medicine, 3D scanners are used to obtain the parameters of the body of a particular patient in the design of orthopedic shoes, corsets, prostheses, and various individual medical devices. 3D-scanning – technologies are widely used in the cinematography, animation, and gaming industries. The 3D scanning of premises and buildings is an important stage of interior design. The resulting three-dimensional models are the bases for the construction of utilities, the design of buildings and premises, the selection and placement of furniture and equipment, VR technology (National Ocean Service 2021).

2. Review and analysis of research

Different types of radar are used to perform such work: optical, acoustic, and laser. High-precision projects require the use of the last, which in turn are expensive and complex

systems. Many optical 3D scanners allow one to obtain data not only on the location of points but also on their colors, which differs favorably from laser 3D scanners. However, optical scanners on a tripod are difficult to use for studying large objects, such as vehicles and large parts in mechanical engineering. Another disadvantage of "optics" is that it does not cope well with copies of black and shiny objects and requires the use of special sprays or other equipment.

2.1. Principle of operation of laser radars

Laser systems make it possible to obtain a high-precision digital copy; they are not vulnerable to the parameters and coverage of an object. The measurements are performed by calculating the return times of laser beams and their wavelengths; this creates accurate, high quality, and three-dimensional maps of any environment they scan. The formed map of an area helps in its characterization and research, which significantly distinguishes this technology against the background of more classic scanning methods.

Laser radar has a long-wavelength optical range ($\lambda \leq 1.5$ μm) and a laser as a source of radiation. Its principle of operation: laser radiation is directed to an object, reflected from the object, and returned to the receiver. Then, the distance to the object is determined in the device. With lidar with a movable mirror in which a 360° viewing angle can be obtained, one can obtain a cloud of environmental points to create a 3D map or digitize architectural objects. Special software creates a three-dimensional image that reproduces the shape around the lidar system with a precise location in space. (Fig. 1).

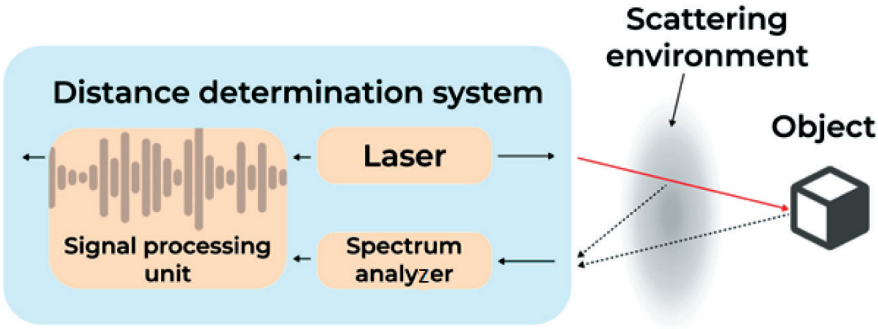

Fig. 1. Lidar scheme

2.2. Principle of operation of optical 3D-scanners

The principle of operation of optical 3D-scanners is simple – the scanning process is to illuminate objects created by a projector with structured light and capture reflected light from certain angles. The scanning object is illuminated with a light strip or pattern – a reference monochrome pattern. By processing the reflected signal and calculating the

locations of the points on its surface based on the difference between the projected and reflected image, the computer obtains the necessary information for building a 3D model (Heritage, Large 2009).

Many optical 3D scanners allow one to obtain data not only on the locations of points but also on their colors, which differs favorably from laser 3D scanners.

Color information is very important; sometimes color changes can diagnose deviations in the properties of a part. It is also necessary for the further reproduction of the appearance of the object, which is critical if not about technical details but about historical objects or works of art.

3. Three factors that distinguish lidars from each other

3.1. Beam control technology

Most leading lidars use one of four methods for directing laser beams in different directions:

1) A rotating lidar in which a certain number of lasers are placed vertically. The design rotates at a speed of several revolutions per second. The advantages of this approach are 360° coverage; however, such designs are expensive and unreliable.
2) A mechanical scanning lidar uses a mirror to redirect a single laser beam in different directions. Some companies use an approach called a "microelectromechanical system" (MEMS) to control the mirror (Zdobytskyi et al. 2020).
3) An active phased array antenna uses a number of emitters that are capable of changing the direction of the laser beam, thus adjusting the relative phase of the signal between adjacent transmitters.
4) A flash-based lidar highlights an entire area at once; existing technologies use one wide-angle laser. The technology has difficulties with long distances, as only a small part of the laser light reaches any point.

3.2. Distance measurement

A lidar measures the time it takes for light to reach and reflect off an object. There are three easy ways to do this:

1) Travel time: the lidar sends a short pulse and measures how long it takes to fix the return of the pulse.
2) Lidar of continuous radiation with frequency modulation: this sends a continuous beam of light, the frequency of which constantly changes over time. The beam is divided in two; one of these is sent to the outside world, and then merges with the other

upon its return. Since the frequency of the beam source changes continuously, the difference in the path of the two rays is expressed through the difference of their frequencies. The result is a picture of interference, the frequency of which is a function of time on the road (and, consequently, from a distance). This path may seem unreasonably complicated, but it has a couple of advantages. This lidar is resistant to interference from other lidars or from the Sun. This lidar can also use a Doppler offset to measure the speeds of objects, not just the distances to them.

3) Lidar of continuous radiation with amplitude modulation: this can be considered as a compromise between the two previous options. A lidar, like a simple sensor that measures time on the road, sends a signal and then measures the time it took it to reflect and return; however, when simple systems send a single pulse, lidar sends a complex circuit (a pseudo-random flow of digital zeros and ones). Proponents of the approach say that this option is more resistant to interference.

3.3. Laser wavelength

This choice is important for two reasons; one of these is eye safety. The fluid inside an eye is transparent to light with wavelengths of 850 nm and 905 nm, which allows light to reach the retina. If a laser is too powerful, it can cause irreparable damage; on the other hand, the eye is opaque to radiation with a wavelength of 1550 nm, which allows such lidars to work at higher power without damaging the retina. Increasing the power allows one to increase the range.

So, why not use lasers with a wavelength of 1550 nm in lidars? Detectors that operate at 850 nm and 905 nm can be created on the basis of inexpensive and common silicon technologies. To create a lidar with a wavelength of 1550 nm, one must use exotic and expensive materials such as gallium, indium, or arsenide.

Even though 1550 nm lasers can operate at higher power without posing a threat to the eye, such power levels can lead to other problems. And, of course, higher-power lasers consume more energy (Neoge, Mehendale 2020).

3.4. Lidar classification of points

Each lidar point can be assigned a classification that determines the type of object that reflects a laser pulse. Lidar points can be divided into several categories, including bare ground or ground, a canopy top, and water. Different classes are defined by using numeric integer codes in LAS files.

When the classification is based on lidar data, points may fall into more than one classification category. Classification flags are used to provide additional descriptions or

classifications of lidar points. With LAS Version 1.0, a lidar point cannot support two assigned classification attributes at the same time. For example, it may be necessary to extract a result that is returned from water from the final dataset, but it should still remain and be managed as a collected lidar point in the LAS file. Using LAS Version 1.0, this point will not be established as water and will be excluded from the analysis.

Later versions (LAS 1.1 and later) have used class flags to solve this problem. Classification flags have been added to the LAS standard to flagpoles with additional information to traditional classification. Synthetic flags, key point flags, hidden flags, and overlaps can be set for each lidar point. These flags can be set along with their classification codes. For example, a water record may have a classification code for water as well as a prohibited flag. This point will remain in the dataset but be hidden from any additional analysis of the LAS files.

Laser pulses that are emitted by a system of lidars are reflected from objects on both the surface of the Earth and above its surface: vegetation, buildings, bridges, etc. One radiated laser pulse can be returned to a lidar sensor as one or more returns. Any radiated laser pulse that encounters several reflective surfaces as it moves toward the ground is broken into as many reflective surfaces, as there are reflective surfaces (McManamon 2020).

The first laser pulse that returns is the most significant return and will be associated with the highest object in a landscape, such as the top of a tree or the top of a building. The first return can also represent land; in such a case, only one return will be detected by the lidar system. Multiple rotations can detect the height of several objects within the laser imprint of the output laser pulse. Intermediate returns are typically used for vegetation structures, and the last returns are used for bare-land relief models. The last return will not always be from a land return; for example, consider a case where a pulse hits a thick branch on the way to the ground and does not actually reach the ground. In this case, the last departure is not from the ground but from the branch that reflected the entire laser pulse (Tab. 1).

Table 1
Data classification

Classification value	Meaning
0	Never classified
1	Not intended
2	Earth
3	Low vegetation
4	Average vegetation
5	High vegetation
6	Building

Table 1 cont.

7	Low point
8	Reserved
9	Reserved
10	Water
11	Railway
12	Road surface
13	Reserved
14	Reserved
15	Wire – shield (shield)
16	Wire – conductor (phase)
17	Transmission tower
18	Wire connector (insulator)
19–63	Deck of bridge
64–255	High noise level

Additional information is stored with each position value's x, y, and z points. For each registered laser pulse, the following lidar point attributes are stored: intensity (Fig. 2), number of revolutions, number of revolutions, point classification values, points at the edge of a flight line, RGB values (red, green, and blue), GPS time, scan angle, and scan direction. The following table describes the attributes that can be assigned to each lidar point (Tab. 2).

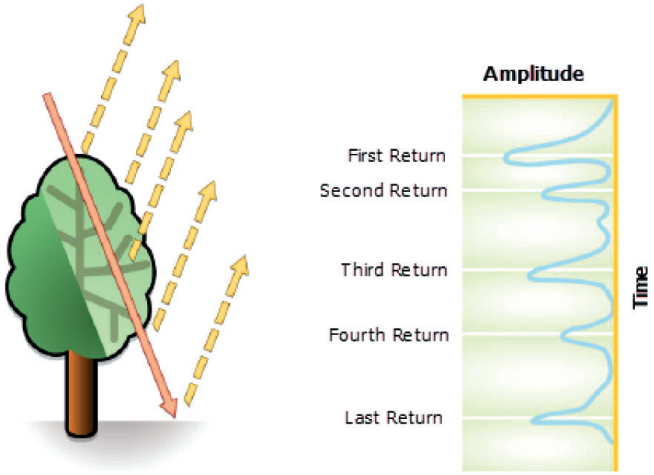

Fig. 2. Returning signal

Table 2
Lidar attributes

Attribute lidar	Description
Intensity	The reverse force of the laser pulse that generated the lidar point
Return number	An emitted laser pulse can have up to five revolutions depending on the characteristics from which it is reflected and the capabilities of the laser scanner that is used to collect the data. The first return will be marked as return number one, the second as return number two, and so on
Number of returns	The number of returns is the total number of returns for a given pulse. For example, a laser data point can return two (return number) in a total of five returns
Point classification	Each lidar point that can be further processed may have a classi-fication that determines the type of object that reflected the laser pulse. Lidar points can be divided into several categories, including bare ground or ground, canopy tops, and water. Different classes are defined using numeric integer codes in LAS files
GPS time	The GPS timestamp at which the laser point was emitted from an aircraft. The time is specified in GPS seconds of the week
Scanning angle	The scan angle is a value in degrees from –90° to +90°. At 0°, the laser pulse is directly below the aircraft at the highest point. At –90°, the laser pulse is on the left side of the aircraft, while at +90°, it is on the right side of the aircraft in the direction of flight. Most lidar systems currently have values that are below ±30°
Scanning direction	The scanning direction is the direction in which the laser scanning mirror moved during the output laser pulse. A value of 1 is the positive direction of the scan, and a value of 0 is the negative direction of the scan. A positive value indicates that the scanner moved from left to right on the track direction, and a negative value indicates the opposite

4. Lidar and API system

With the development of technology in the modern world, the lidar as the system has begun to be used in various fields, which allows it to comprehensively solve many issues that are related to scanning objects. To qualitatively improve the use of the lidar of the systems, the priority is to ensure their availability in a wide range of industries.

Although the basic idea is simple, the details complicate things very quickly. Lidars face the challenge of making decisions based on the following three basic principles: the method of multi-directional laser direction, measuring the duration of a signal in the forward and reverse directions, and the spectrum of light that was used.

Due to the use of a significant number of lasers, we obtain an array of significant data points.

Since one of the key points of the above technologies involves the analysis and processing of large amounts of data, the study considers one of the options for optimizing this process; namely, the remote processing of data that contains information about coordinates GPS positions, etc. This approach will simplify a mobile system and increase its usability in the case of interacting through a mobile application.

A lidar system consists of components that are responsible for determining distance, positioning, and orientation as well as a database, emitter, and receiver. The distance-determination system consists of a laser and a spectrum analyzer. The laser creates and sends a light flux through the emitter, which in turn is returned to the receiver. The laser also sends a signal to the database to create a timestamp; this is used to compare with the information that is provided by the receiver. The receiver transmits the reflected signal to the spectrum analyzer; together with the wavelength, time of receiving the signal, and its angle, information from this unit is transferred to a database (where it is grouped and compared). The database also contains information from the GPS system about location, position, and acceleration when moving the system.

All of this data is stored in a database; based on this, a detailed cloud of surface points of any complexity is created. It is advantageous to use cloud services to create a cloud of data; they simplify the system and, in combination with the use of a mobile application, significantly increase the convenience.

Cloud storage is a model of storing data on a computer in which digital data is stored in logical pools; this physical storage covers several servers (usually in several places). The physical environment usually belongs to the hosting companies that manage it. These cloud storage providers are responsible for maintaining and accessing available information as well as for the physical environment. Users can purchase the ability to store data from cloud storage service providers.

Cloud storage services can be accessed through a web service interface (API) or applications that use an API; thus, the system receives many benefits. It is more profitable to use cloud capacity than to keep one's own. Cloud storage gives users instant access to a wide range of resources and applications that are hosted on another organization's infrastructure through a web service interface. Cloud storage makes it possible to have a backup of data, as companies that provide similar services have two or three different backup servers that are located in different places around the world. In this way, the data is reliably protected from loss.

The use of API significantly increases the convenience of the system. A user can access the results through a mobile application for instant viewing anywhere and anytime. One can also work on an object in detail via a personal computer using the power of the server; all one needs is access to the Internet (Fig. 3).

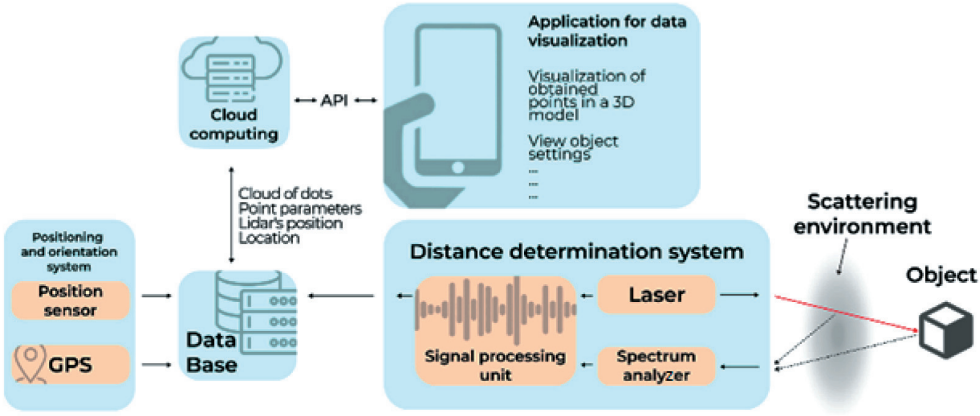

Fig. 3. Block diagram of technical implementation of lidars using cloud technologies

5. Conclusions

The implementation of such a system has a number of significant advantages over cloud storage. Moreover, it provides users with instant access to a wide range of resources and applications that are hosted in another organization's infrastructure via the interface of the web service. The use of an API significantly increases the usability of the system, as the user is provided with the necessary access to the results via a mobile application for instant viewing at any convenient time.

REFERENCES

Heritage G.L., Large A.R.G. (Eds.), 2009, *Laser Scanning for the Environmental Sciences*, John Wiley & Sons.

McManamon P.F., 2020, *LiDAR Technologies and Systems*, Society of Photo-Optical Instrumentation Engineers, Washington.

National Ocean Service, 2021, *What is lidar?* [electronic resource]: https://oceanservice.noaa.gov/facts/lidar.html [18.10.2021].

Neoge S., Mehendale N., 2020, *Review on LiDAR technology* [electronic resource]: https://papers.ssrn.com/sol3/papers.cfm?abstract_id=3604309 [10.09.2021].

Zdobytskyi A., Lobur M., Dutka V., Prodanyuk M., Senkovych O., 2020, *Determination of dispersion medium parameters by intelligent microelectromechanical system*, 16th International Conference on the Perspective Technologies and Methods in MEMS Design (MEMSTECH). Proceedings, 49–52. DOI: https://doi.org/10.1109/MEMSTECH49584.2020.9109482.

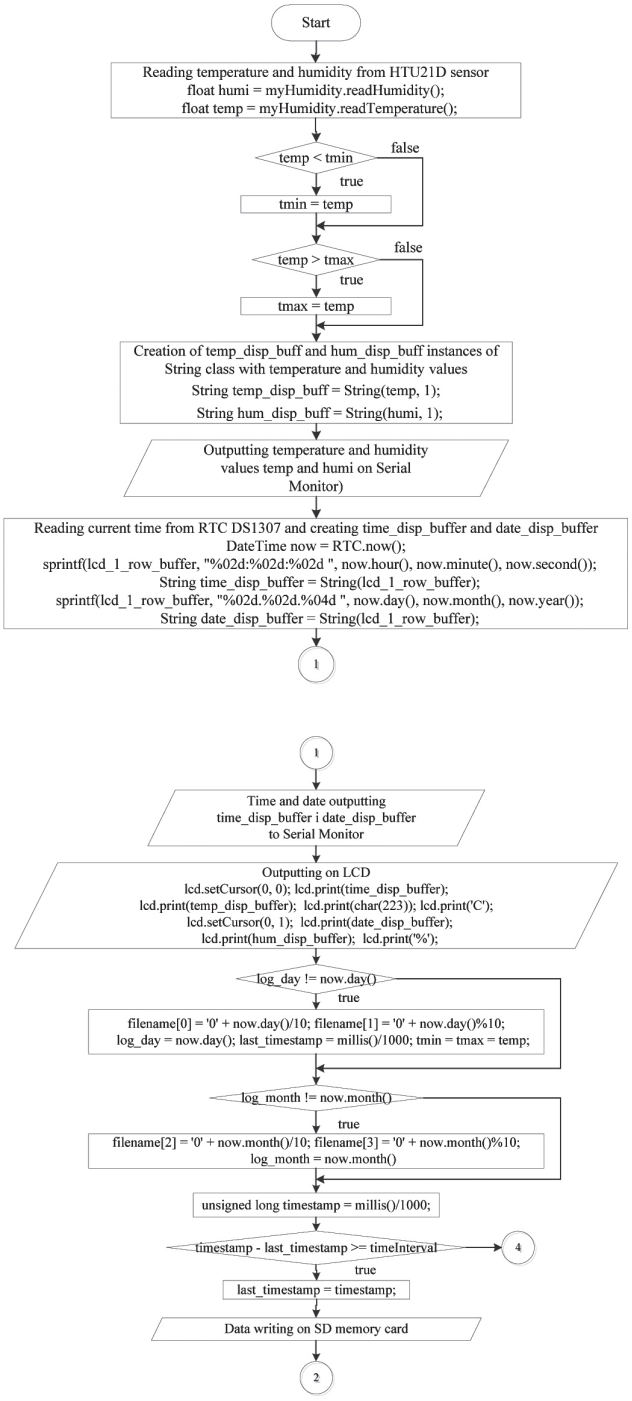

Fig. 3. Operation algorithm of microcontroller-based temperature and humidity data logger

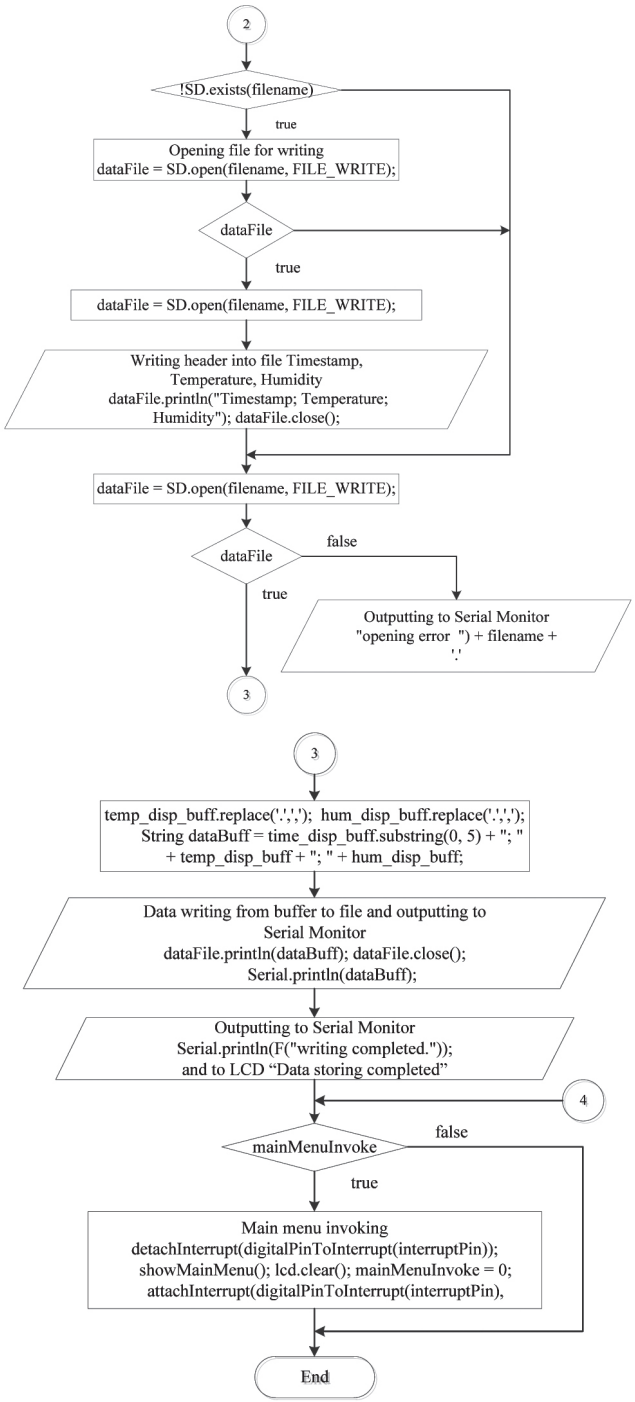

Fig. 4. Operation algorithm of microcontroller-based temperature and humidity data logger

back to article

e-ISBN 978-83-67427-25-8
ISBN 978-83-67427-24-1